		100		STAFF SUMN	1AF	Y SHEET			
	ТО	ACTION	SIGNATURE (Surname	e) GRADE AND DATE		TO	ACTION	SIGNATURE	(Surname), GRADE AND DATE
1	USAFA/ DFAN	sig	Chadare	146012/1/14	6				
2	USAFA/ DFER	approve	SOLT I AD 25		7				
3	USAFA/ DFAN	action	(Author / Originat	or)	8	¥			
4					9				
5					10				
SU	RNAME OF ACT	ION OFFICER A	ND GRADE	SYMBOL	_	PHONE		TYPIST'S INITIALS	SUSPENSE DATE
Aı	ndrew J. Loft	house, Lt Co	I, USAF	Hq USAFA/DFAN	1	333-9526		ajl	20141201
	IBJECT				- · ·		7. 1		DATE
Cl	earance for N	Material for P	ublic Release	U	SA.	FA-DF-PA-	705		20141201
	IMMARY						No. of Whose have	10000000000 1	112
1.	PURPOSE.	To provide s	ecurity and policy	review on the docu	mei	its at Tab 1 p	orior to releas	e to the pu	blic.
2.	BACKGRO	OUND.							
	uthors: Mehondrew J. Loft		Krzysztof Fyszka,	Keith Bergeron, Ju	rge	n Seidel, Ada	am Jirasek, Rı	issell M. C	ummings and
Ti M	itles: Vortica	al Flow Predi arachute Can	ctions of the AVT- opies; Computation	183 Diamond Wing nal Fluid Dynamics	g; C for	rid Quality a the Aerodyn	and Resolutio namic Design	n Effects o and Mode	on the Aerodynamic ling
C	ircle one: A	Abstract	Tech Report	Journal Article	S	peech (I	Paper Pre	esentation	Poster
		Thesis/Disse	rtation Book	Other:	-				
C	heck all that	apply (For C	ommunications Pur	rposes):					
		[] CRADA (C	Cooperative Research	ch and Developmen	ıt A	greement) ex	cists		
		[] Photo/ Vide	eo Opportunities	[] STEM-outread	h R	elated []	New Invention	on/ Discove	ery/ Patent
	escription: Puring 5-9 Jan		oing work research	accomplished by H	PC	RC personne	el to be presen	ated at the	AIAA SciTech Conference
R	elease Inform	nation: AIA	A Science and Tec	hnology Forum and	i Ex	position 201	15, Kissimme	e, FL, 5-9	Jan 2015
P n	revious Clea ot yet been c	rance inform leared for pu	ation: Some materi blic release.	al has been derived	fro	m several pr	eviously clea	red AIAA	papers. Other material has
R	Recommende	d Distribution	n Statement: Distrib	oution A, Approved	l fo	r Public relea	ase, distributi	on unlimit	ed.
3	. DISCUSSI	ON. N/A							
4 ti	RECOMMI	ENDATION. being unclas	Sign coord block a sified, not jeopardi	above indicating do zing DoD interests	cun , an	nent is suitab d accurately	ole for public portraying of	release. Su ficial party	nitability is based soley on
A	ANDREW J.	LOFTHOUSE	E, A Col, JSAP	nter 1.3		IAA Papers	to be presente	ed	

Entra and the works

Computational Fluid Dynamics for the Aerodynamic Design and Modeling of a Ram-Air Parachute with Bleed-Air Actuators

K. Bergeron*

US Army Natick Soldier, Research, Development, and Engineering Center, Natick, MA 01760

Jürgen Seidel[‡], Mehdi Ghoreyshi[†], Adam Jirasek[§], Andrew J. Lofthouse¹, Russell M. Cummings High Performance Computing Research Center, U.S. Air Force Academy USAF Academy, Colorado 80840

The activation of spoilers on the upper surface of a wing is a relatively new method of achieving longitudinal and lateral control of ram-air canopies, often referred to as parafoils. No numerical studies, however, have fully investigated the 3-D aerodynamic performance of these bleed-air actuators. Simulation results are presented for a finite span, ram-air canopy geometry and several configurations amenable for comparison with wind tunnel experiments and flight test data. Assessments are also made between the resulting flowfields and previously reported 2-D computational fluid dynamics (CFD) results. Evaluations include cases with an asymmetrical trailing edge deflection to simulate a turn and the inclusion of two different bleed-air vents. Lift, drag and roll coefficients correlate well with wind tunnel and flight test results.

Nomenclature

AR	aspect ratio, b/S	L/D Re	lift to drag ratio Reynolds Number, Vc/v
b	span	,	Time
C	airfoil/wing chord	1	non-dimensional time, $t*V/c$
C_L	lift coefficient, $L/q_{\infty}S$	<i>t</i> *	non-dimensional time, i vic
	drag coefficient, $D/q_{\infty}S$	S	Area
C_D		V	Velocity
C_l	rolling moment, $L/q_{\infty}Sb$	· · · · · · · · · · · · · · · · · · ·	friction velocity at wall
C_m	pitching moment, $M/q_{\infty}Sc$	u^*	
	yawing moment, $N/q_{\infty}Sb$	y^{τ}	y-plus, u^*y/v
C_n	yawing moment, 11/4%55	a	angle of attack
C_y D	side coefficient, $Y/q_{\infty}S$		Density
D	drag force	ρ	
L	lift force	ν	air viscosity

I. Introduction

An autonomously guided cargo deliver consists of a ram-air canopy, suspension lines connecting the canopy to an airborne guidance unit which in turn is connected to a payload. The original ram-air inflated wing was proposed by Domina Jalbert in 19611 with the trailing edge being deflected down for lateral and longitudinal flight control. An asymmetric deflection provides turning authority, skid steering, such that a right turn is produced by the right side deflection. A symmetric deflection, on the other hand, changes the descent rate and glide angle. For both the asymmetric and symmetric tail deflection the resulting dynamics has led to the term "brakes" being the common vernacular to identify this control mechanism. Ware and Hassel² conducted wind tunnel tests of various ram air canopies and note symmetric deflection

Senior Research Aerospace Engineer, AIAA Senior Member

[†] Senior Aerospace Engineer, AIAA Senior Member

[‡]Research Associate, AIAA Senior Member § Research Fellow, AIAA Senior Member

Director, AIAA Senior Member

Professor of Aeronautics, AIAA Associate Fellow

of the trailing edge to an angle of about 45°, as measured from the chord line, resulted in a relatively small change in the trim angle of attack and the lift-drag (L/D) ratio remained effectively unchanged. However, increasing the deflection of the trailing edge to larger angles, approaching 90°, caused a large change in trim angle of attack and the L/D could be reduced to approximately 0.5. Matos et al. reported an L/D variation from 3.1 to 2.1 during wind tunnel testing of a Clark-Y ram-air canopy, as a function of trailing edge deflection (TD). They also documented a variation in angle of attack, α , between 8.8°, for the unrestrained case, and 6°, "when maximum flap was applied."

Ram-air canopies have been widely used by sport parachutists since the mid-70s, and many variations in design are documented in Poynter⁴. Depending on the wing planform and angle-of-incidence the forces and moments associated with TD deflection can vary widely. A small number of parachutists have pursued canopy designs and guidance strategies which optimize the use of TD between 45° and 90° to perform precision landings, and Bergeron et al summarize some of the more common techniques and designs⁵. The use of bleed-air (BA) "spoilers" to increase control authority for personnel airdrop was pioneered and tested for personnel airdrop applications in the mid-1970's by H. Bergeron.⁶ J. Hayhurst and J. Eiff also investigated the use of spoilers for personnel use in the mid-1980's⁷. These personnel systems used a combination of coupled control lines (TD and spoilers) where the bleed-air vents opened and closed to spoil the flow across the upper surface of the ram-air parachute. However, the incremental increase in longitudinal control authority that was offered with the addition of the BA vents to the standard TD did not have significant enough performance improvements to be adopted by personnel parachutists.

Instead, canopy design efforts have concentrated on reducing deployment forces, increasing the L/D performance, and reducing pack volume of sport ram-air canopies. As a result of the L/D focus, the majority of personnel canopies have tapered or elliptical planforms with aspect ratios (AR) greater than 2.5 and wing loadings greater than 1. These designs have in turn led sport parachutists, following the lead of paragliding pilots⁸, to experiment with and include the use of leading edge deflection and weight shift as additional control inputs. The utility of these inputs has been rather limited as the effectiveness of these methods is relatively constrained in the first case by the additional force needed to initiate the leading edge deflection and in the second case by the dependence on the underlying airfoil shape. Designs have also included inlet optimization, see for example Germain⁹, to reduce profile drag and enhance internal pressurization. With respect to shape, weight shift is a relatively ineffective mechanism for lateral control of personnel or cargo canopies with AR = 2 or less. While such low aspect ratio canopies have a reduced L/D range, their slow flight capabilities are particularly useful for combining precision accuracy with payload "survivability."

The use of ram-air canopies to autonomously deliver payloads began in earnest in the 1990s by NASA¹⁰ and demonstrated with their X-38 program¹¹. More recently, the Joint Precision AirDrop System (JPADS) family of systems included "self-guided" cargo parachute systems across a payload weight range of 10 lbs to 42Klbs¹². Both the X-38 and JPADS programs used traditional TD as the flight control mechanism. Ward et al.¹³ present multibody simulation results demonstrating weight shift control as an effective means of providing longitudinal and lateral control of parafoils. Longitudinal control via angle of incidence changes, which is equivalent to weight shift control has been demonstrated on small scale systems¹⁴, and larger scale systems have also shown the method can be used to enhance landing accuracy.

Higgins¹⁵ documents the potential use of a bleed air vent system for autonomously control airdrop systems and Gavrilovski et al¹⁶ used a virtual spoiler method on a non-airdrop ram-air gliding system for both lateral and longitudinal control. This work was based on wind tunnel testing and preliminary computational fluid dynamics (CFD) work documented in Bergeron et al.¹⁷, and flight tests of the method¹⁸ showed a linear glide slope change with respect to spoiler deflection and also a linear dependence between the number of cells activated and the percent of glide slope change.

Several researchers have presented CFD results for ram-air parachute configurations both 2-D and 3-D, and Fogell¹⁹ includes a good overview of these contributions. However, no high-fidelity CFD study has fully investigated the 3-D aerodynamic performance of any of the various flight control methods discussed above. The present work continues the investigation of ram-air flow fields as part of a

comprehensive Verification and Validation (V&V) initiated by Natick Soldier, Research, Development, and Engineering Center (NSRDEC)^{20, 21}. In addition, this study extends 2-D bleed-air vent simulations to 3-D. Results are presented using the finite volume method solvers *Kestrel*^{22, 23} and *Cobalt*²⁴, which have been extensively validated for unsteady CFD for fixed wing aircraft. *Kestrel* is a fixed wing multiphysics computational engineering product of the High Performance Computing and Modernization Program's (HPCMP) Computational Research and Engineering for Acquisition Tools and Environments-Air Vehicle (CREATETM-AV) program. The results also support parallel work in Ghoreyshi et al²⁵ which specifically, addresses meshing considerations for these types of coupled cavity-airfoil geometries. The paper first reviews the grid generation, flow solver, and computational parameters. Test cases are then described, and results are presented. Finally, conclusions and recommendations are given.

II. Computational Setup

As previously mentioned, this computational effort was conducted in parallel to the results reported in Ghoreyshi et al²⁵. Details of the grid convergence study for various geometries as well as validation results are included in that presentation.

A. Geometry

The baseline geometries used for the validation simulations are shown in Figure 1. These geometries are derived from the cut pattern used in the manufacturing process of a ram-air canopy being drop tested and which is designed to enable precision landings with a nearly vertical final descent profile. The solid models represent a half span of the actual wing, such that the model aspect ratio, AR, is 1. They were created in a modular manner to enable the construction of multiple wind tunnel configurations that would be used for validation and testing. Four attachment holes for the wind tunnel mounting can be seen in the root of each wing. To provide a well-posed airfoil shape for the rounded closed inlet case, a cubic spline was used. The rounded leading edge may be removed, as emphasized by the red circles in Figure 1, to produce a closed, or open, flat nose with an angle the same as the open inlet ram-air canopy. Though the rounded and flat nose leading edge geometries do not represent a ram-air parachute, they are critical models for conducting simulation validation, and they serve as a reference for understanding the flow characteristics of the ram-air canopy's hybrid cavity-airfoil design. An additional configuration of interest included the 50% asymmetric deflection of the trailing edge of the airfoil, highlighted by the green circles in Figure 1. Finally, Figure 1d. illustrates the combination of the leading and trailing edge modifications.

Future rigid geometries and solid models will include additional features that more accurately capture steady flight configurations of the ram-air canopy. These characteristics include the inflated deformation of the ram-air canopy cells as well as the arc anhedral. Open inlet geometries, and meshes, with a straight and 50% deflected trailing edge were computationally modeled and simulations completed, but no solid models were constructed for these specific configurations. The open inlet simulation data will, however, be compared against future wind tunnel experiments.

Eslambolchi and Johari²⁶ conducted rigid canopy simulations of a different baseline airfoil, with inflation and arc anhedral included, to assess the fidelity of the lifting-line theory in predicting the forces on the canopy during steady glide. The authors found the forces on the canopy during steady glide using finite wing theory to be only accurate to approximately 30% for the expected operational range of angle of attack for their canopy. These differences were attributed to a variety of factors which accentuate the difficulties of high-fidelity ram-air modeling and simulation as well as obtaining accurate aerodynamic force and moment measurements from parachute drop tests.

Using the current geometries, two additional configurations including two different versions of the bleed-air vents were simulated. The placement of the vents was restricted to the middle of the ram-air airfoil, and followed the designs for which previous 2-D CFD simulations had been completed.²⁰ Vent

width was approximately 14% of the half span. This size was chosen to model the equivalent vent size on an airdrop canopy. Finally, an open inlet geometry with an asymmetric TD of 50% was simulated, and represent, to the authors' knowledge, the first such simulations. These results will be presented and compared against 2-D CFD flowfields, and as mentioned earlier, they will also be compared against wind tunnel experiments in a future effort.

B. Computational Grid

Both structured and hybrid grids for a half wing with a symmetry plane were tested, and will be identified in the presentation of results. The "structured" meshes (structured everywhere except the wing tip surface and the volume mesh from the tip to the far-field boundary) had between 15M and 39M cells, and were created using *Pointwise*. The hybrid meshes used a refined boundary layer grid along the airfoil surfaces to capture the boundary layer while a tetrahedral grid was used for the far field. The unstructured meshes ranged from 5.5M to 5.9M cells, and they were created using CREATETM-AV *Capstone*. Sample projections of the various meshes used in these simulations are illustrated in Figure 2.

Except for the BA grids, the grids have a $y^+ < 1$ which ensures the first computational cell above the wall is located within the viscous sub-layer. Figure 3 illustrates the wall y^+ for the open inlet-no TD configuration. For the BA vent grids, the y^+ around the vent flaps is approximately 2. The growth rate in the viscous layer is < 1.25 for all grids. For the symmetry wall the grid spacing was 0.1. Additionally, the farfield was located at +/-10c.

C. Flow Regime and Simulation Parameters

CFD results were computed using both the commercially available code *Cobalt* and the DoD-developed solver within the *Kestrel* software suite. Both codes are based on finite-volume methods and in addition to performing traditional Reynolds Averaged Navier-Stokes (RANS) calculations, also have the capability to perform Delayed-Detached Eddy Simulations (DDES). Cobalt simulations were run on the Cray XE6 at Engineering Research Development Center (ERDC) DoD Supercomputing Resource Centers (DSRC) while *Kestrel* was used on the SGI ICE X System located at the AFRL DSRC.

The numerical method used by *Cobalt* is based on Godunov's first-order accurate, cell-centered, finite volume, exact Riemann solution method applicable to arbitrary cell topologies²⁷. The spatial operator uses the exact Riemann Solver of Gottlieb and Groth, least squares gradient calculations using QR factorization to provide second order accuracy in space, and TVD flux limiters to limit extremes at cell faces²⁸. A point implicit method using analytic first-order inviscid and viscous Jacobians is used for advancement of the discretized system. For time-accurate computations, a second order accurate Newton sub-iteration scheme is employed. Parallel performance is achieved using the ParMETIS domain decomposition library for optimal load balancing with a minimal surface interface between zones²⁹. The code uses Message Passing Interface (MPI) for communication between processors, with parallel efficiencies above 95% on as many as 1024 processors and scales linearly up to 4000 processors.

The flow solver component of *Kestrel* solves the unsteady, three-dimensional, compressible Navier-Stokes equations on hybrid unstructured grids. Its foundation is also based on Godunov's first-order accurate, exact Riemann solver. Second-order spatial accuracy is obtained through a least squares reconstruction. The code uses an implicit Newton sub-iteration method to improve time accuracy as well. *Kestrel* receives an eXtensible Markup Language (XML) input file generated by *Kestrel* User Interface and stores the solution convergence and volume results in a common data structure for later use by the Output Manager component. Some available turbulence models are the Spalart-Allmaras (SA) model, SA for Rotation/Curvature (SARC), and DDES with SARC. For these simulations the inviscid flux calculations were computed with the Harten, Lax, van Leer, and Einfeldt (HLLE) Riemann solver, and the Barth/Jespersen flux differencing scheme was used.

Table 1 documents the parameters and conditions used for the unsteady, 2^{nd} order in time, simulations which resulted in a Reynolds number, $Re = 1.4 \times 10^6$ with a non-dimensional time step $\Delta t^* = 0.007$. Given

these values, Figure 4 shows typical convergence histories for the lift, drag, pitch, roll, and yaw coefficients. These specific plots are for the FB (flat leading edge, 50% TD) geometry. Convergence occurs between 1000 and 1500 iterations.

Table 1. General Job File Inputs and "Test" Matrix

Value or Condition
Ideal Gas
SARC-DDES
3
5000
0.25
0, 4, 8, 12, 16, 20
81,850
290
0.000025
84

IV. Simulation Results and Discussion

In this section, computational results are presented for the rigid configurations. The first data serve as preliminary validation of computational techniques and processes. Though simulations were conducted for $0^{\circ} < \alpha < 20^{\circ}$, analyses of the flowfields will not be discussed for all conditions. The set of presented results will illustrate flowfield evolution for open and closed inlet geometries at $\alpha = 8^{\circ}$ as this value is representative of the nominal angle of incidence, and thus angle of attack, used for ram-air systems used for personnel and cargo airdrop. Finally, data will be discussed for various open inlet designs including the straight trailing edge, deflected trailing edge, and front- and rear-flap bleed-air vents.

A. Validation with Wind Tunnel Experiments, RS Geometry

In an earlier validation effort Ghoreyshi et al.²¹ compared CFD results against data from experiments performed at Kyushu Institute of Technology of Japan³⁰ with inconclusive results. The Japanese experiment measured a setup with a flexible wing surface supported by fixed ribs at a Mach number of 0.04 and Reynolds number of 2 × 10⁵. However, the simulations assumed a rigid structure throughout, and it is believed this structural difference is the main contributor to the discrepancies among the measured forces and moments. NSRDEC and the USAFA subsequently designed a new set of experiments using the geometries described above, and a comprehensive report of the experimental results will be reported later.

The C_L and C_D from the *Kestrel* simulations and the airfoil wind tunnel experimental values are depicted in Figure 5 and show good agreements. It should also be noted that a grid convergence study, which included using *Cobalt* was conducted as part of these analyses. As a result a grid size of approximately 6M cells was used in *Kestrel* for the remaining computations. Figure 6, illustrates the attached flow about a finite RS geometry, and shows the simulation capturing the strong wing tip vortex. With these validation results, the remainder of the presentation will address the aerodynamic characteristics of the different geometries at $\alpha = 8^{\circ}$.

B. Closed Geometries: RS, FS, RB, and FB

In Figure 7 a plot of the isosurface of normalized Q = 0.1, i.e., the second invariant of the gradient tensor³¹, colored by pressure is used to track vortical structures in the flow. The predominant effect due to geometry changes is seen in corresponding changes in the topology of the wing tip vortex. Three

vortex structures are identified in Figures 7a. and 7b.— tip nose, tip upper surface, and tip lower surface vortices. These structures may also be identified by the reader in Figures 7c. and 7d.

The tip nose vortex of the RS geometry evolves from the separation of the flow along a relatively large portion of the leading edge at the wing tip. The locally unsteady flow organizes into a structure at .1c and follows the pressure gradient to the top of the wing near .25c. At that position the tip nose vortex passes over the tip upper surface vortex which has been created near .25c. Additionally, a similar lower surface tip vortex has been created at approximately .125c, and slowly grows spatially while also following the pressure gradient towards the upper surface until it crosses the tip at .75c. For the FS wing, the pointed nose at the wing tip causes a concentrated vortex to form but with a weaker amount of energy as compared to the RS tip nose vortex. As such, the majority of the FS tip nose vortex joins with the upper surface tip vortex. The remaining wing tip separated flow, below the pointed nose, bursts into several small vortical structures until the majority of the enstrophy organizes itself with the lower surface vortex and follows the favorable pressure gradient around the wing tip to .75c as did the RS case. A small vortical structure is seen to join the upper surface vortex at .5c. The resulting lift is reduced and drag increased for the FS relative to the RS configuration, and the L/D is reduced by approximately 4%.

Figures 7c. and 7d. illustrate the effect of the asymmetric trailing edge deflection on the closed geometries. In particular, the magnitudes of the lift, drag, pitch, roll, and yaw coefficients increase, but where the RS and FS L/D are approximately 7.1 and 6.8 respectively, the L/D for RB, 5.6, and for BF, 5.5, are significantly reduced. Indeed, the TD leads to significant changes in all aerodynamic characteristics with a 60% increase in C_D (L/D decreases by 20%) and a 100% increase in C_n . These characteristics align with the use of the trailing edge deflection for longitudinal and lateral control of the ram-air canopies—glide slope changes result from symmetric TD and a turn is initiated by an asymmetric trailing edge deflection on the either side of the canopy. The drag and yaw prevail over lift and roll increases. Airdrop tests of different ram-air geometries have shown control inputs with lower amounts of TD which result in initially opposite lateral and longitudinal responses, but these conditions were not investigated in this work. Table 2 documents the changes in the force and moment coefficients for the FS, RB, and FB configurations relative to RS.

Table 2. Percent Change Forces and Moments, Closed Geometries (Relative to RS.)

Coefficient	FS (RS)	RB (RS)	FB (RS)
C_L	-0.8%	27.8%	26.2%
C_D	3.4%	63.5%	65.0%
L/D	-4.1%	-21.8%	-23.5%
C_{y}	4.8%	40.6%	45.6%
C_m	0.9%	14.3%	14.7%
C_{l}	-0.6%	39.0%	37.1%
C_n	8.4%	95.4%	101.9%

A flow description similar to the non-deflected trailing edge cases follows for the TD cases, though in Figure 7d. at .5c additional bursting along the outward face of the wing tip has now joined with the upper surface vortex. The more favorable pressure gradient for the deflected trailing edge cases also leads to a widening in the vortical structures at the trailing edge. Additionally, the increased curvature at the trailing edge induces separation.

C. Open Inlet Geometries: Open, 50% TD, and Bleed-air Vents

At α near 8°, except for the rear-flap bleed-air vent configuration, the 2-D simulations of ram-air geometries ¹⁹ exhibited a strong separation bubble, reference Figures 8 and 9. In the case of the rear-flap bleed-air vent, the flow along the upper surface of the geometry was significantly accelerated resulting in

an attached flow and an order of magnitude increase in the ram-air airfoil's L/D. However, the results presented below support the need to complete 3-D simulations in order to obtain valid data for these otherwise geometrically simple cavity-airfoil flows.

1. 0% and 50% TD

The percent change relative to the corresponding closed geometry for the 0% and 50% TD configurations are documented in Table 3. Overall aerodynamic performance is diminished. In both cases the L/D is reduced by the same percentage, as compared to the closed rounded geometries. The major differences in coefficients are in the side force and yaw. For the 0% TD case, the percent relative change for both C_y and C_n is twice as large as the 50% TD relative change, and indicates the dominant contribution of the TD as opposed to the change from the closed to open inlet. In Figure 10, the upper surface flow is attached except for the small separation region near the root of the wing. The flowfield has a three-dimensional structure similar to the closed inlet geometries RS and FS, but with a reduced L/D = 6.2 and an increase of over 25% in C_n .

Table 3. Percent Change Forces and Moments, Open Geometries (Relative to equivalent closed geometries.)

Coefficient	0% TD (RS)	50% TD (RB)
C_L	-6.3%	-8.0%
C_D	8.4%	6.4%
L/D	-13.6%	-13.5%
C_v	10.7%	5.4%
C_m	-6.0%	-9.3%
C_{l}	-6.6%	-7.9%
C_n	26.2%	12.1%

Figure 11 shows a much stronger separated flow at the wing root.

2. 0% TD, Front Flap and Rear Flap Bleed-air Vents

In Figures 10-13, the ram-air airfoil surfaces have been illustrated with a transparency effect such that Q structures may be seen in the interior of the cells. While the magnitudes of the vortical structures are significantly less than those seen on the outer surface, there is a nonzero variation throughout. Actual ram-air canopies typically include crossports between adjacent cells, positioned at several chordwise locations, to allow pressure equalization across the span of the ram-air airfoil. The crossport features are important to include for accurately modeling future fluid structure interactions (FSI), but they are not modeled in these results.

Table 4. Percent Change Forces and Moments, Bleed-Air Vents (Relative to the 0%TD geometry.)

Coefficient	Front Flap (0%TD)	Rear Flap (0%TD)
C_L	-14.1%	-0.6%
C_D	49.8%	0.6%
L/D	-42.6%	-1.1%
C_{v}	-9.5%	-1.9%
C_m	-21.9%	-0.8%
C_{l}	-12.3%	-0.4%
C,	59.9%	1.0%

Qualitatively, the 3-D BA vent flows mirror the behavior of the 2-D simulations in Figure 9. However for the front flap BA, even though the intersection of a streamwise plane centered at the mid-span point of the vent with the flow would show a field similar to the 2-D field of Figure 9a., the 3-D structure (ref Figure 12) has complex transverse recirculation components. The strength of the front flap BA jet causes a separation bubble which affects 75% of the ram-air airfoil span. Alternatively, the flow field for the rear vent BA shows a relatively mild perturbation as compared with the laminar flow of the no-vent ram-air geometry. The 3-D effect is much less than that predicted by 2-D simulations, and the result also follows more closely with field data.

Table 4 quantitatively shows the relative effects of the BA vents as compared to the no-vent, ram-air geometry. For the front-flap BA vent, the decrease in lift and large increases, with respect to the 0% TD baseline, in drag and yaw reflects the effectiveness of the "spoiler." The 3-D rear flap BA vent forces and moments, though, indicate a significantly different overall behavior as compared to 2-D.

3. 0% TD, 50% TD, and Front Flap Bleed-air Vent

The data in Table 5 identifies the different aerodynamic contributions to longitudinal and turning response changes depending on the type of actuation used. No attempt has been made to identify conditions for equivalent turning response or longitudinal rate changes between the two control methods. While turning response comparisons require a more detailed analysis, for the defined geometries, the data indicates the front flap BA vent is a more effective mechanism for longitudinal control than TD.

Table 5. Percent Change Forces and Moments (Relative to the 0%TD geometry.)

Coefficient	50% TD (0% TD)	Front Flap BA (0%TD		
C_L	25.5%	-14.1%		
C_D	60.4%	49.8%		
L/D	-21.7%	-42.6%		
C_{y}	33.8%	-9.5%		
C_m	10.2%	-21.9%		
C_{I}	37.1%	-12.3%		
C_n	73.6%	59.9%		

The positioning of the BA vent was somewhat arbitrary, though the current design lends itself to modular application across the surfaces of the ram-air geometry. Therefore, a geometric superposition of vents on the surfaces of the canopy may be easily accommodated. Trailing edge deflection modifications are less systematically employed. Additionally, changes in the baseline airfoil geometry will have significant influence on responses of each control method.

V. Conclusion

Computational results for 3-D ram-air geometries including trailing edge deflection and bleed-air vents have produced a rich data set which may be used for control law design. The validation of the numerical models against wind tunnel data suggests meshes on the order of 6M cells are sufficient for engineering analysis for these conditions. The results confirm the application of symmetric trailing edge deflection for longitudinal control using a downward deflection on the order of 45° . However, a single BA vent produced twice the change in L/D as was produced by the TD. Skid steering was also verified as the dominant turning response for ram-air canopies, while BA vents were shown to be effective control methods in this regard. Future work will continue the validation of the computational methods with wind tunnel experiments and airdrop tests. New efforts will also address BA vent location and TD/BA vent coupling.

Acknowledgements

The authors would like to first acknowledge the support of the Natick Soldier Research Development and Engineering Center Airdrop Technology Team and the DoD HPCMP. In particular, the HPCMP's CREATETM-AV team has provided substantial resources and help, including valuable meshing inputs from many members participating in the program's FY14 Strategic TARgeting (STAR) Projects. Finally, Mehdi Ghorevshi and Jürgen Seidel extend their appreciation for the researchers and technicians at the Aeronautics Research Center and the High Performance Computing Research Center at the USAF Academy (USAFA) who have time and again provided critical assistance and insights.

This material is based in part on research sponsored by the USAFA under agreement number FA7000-10-2-0026 and contract number FA7000-10-2-0009. The U.S. Government is authorized to reproduce and distribute reprints for Governmental purposes notwithstanding any copyright notation thereon. The views and conclusions contained herein are those of the authors and should not be interpreted as necessarily representing the official policies or endorsements, either expressed or implied, of the NSRDEC, USAFA, or the U.S. Government.

References

¹ Jalbert, D. C., "Multi-Cell Wing Type Aerial Device," U.S. Patent No. 3,285,246.

² Ware, G.M., and Hassell, J. L., "Wind-Tunnel Investigation of Ram-Air-Inflated All-Flexible Wings of Aspect Ratios 1.0 to 3.0," Technical Report, NASA, 1969, TM SX-1923.

³ Matos, C., Mahalingham, R., Ottinger, G., Klapper, J., Funk, R., and Komerath, N, "Wind Tunnel Measurements of Parafoil Geometry and Aerodynamics," AIAA 98-0606.

⁴ Poynter, D., The Parachute Manual: A Technical Treatise on Aerodynamic Decelerators, Volume 1 and 2, Para Publishing, Santa Barbara, CA, 1991.

⁵ Bergeron, K., Feizi, A. and Tayan, S., "AccuGlide 100: Precision Airdrop Guidance and Control via Glide Slope Control," AIAA 2011-2530.

⁶ Bergeron, H., Private communication.

⁷ Eiff, J. and Hayhurst, J., "Classic Accuracy Manual," Eiff Aerodynamics.

⁸ Whittall, N., Paragliding: The Complete Guide, Lyons Press, New York, 1995.

⁹ Germain, B., "The Parachute and its Pilot," American Printing, 2004.

¹⁰ Murray, J., Sim, A., Neufeld, D., Rennich, P., Norris, S., and Hughes, W., "Further Development and Flight Test of an Autonomous Precision Landing System Using a Parafoil," NASA TM-4599, July 1994.

¹¹ Iacomini, C. S., and Cerimele, C. J. "Longitudinal Aerodynamics From a Large Scale Parafoil Test Program," AIAA Paper 1999-1732, 1999.

¹² Benney, R., Henry, M., Lafond, K., Meloni, A., and Patel, S., "DoD New JPADS Programs & NATO Activities," AIAA Paper 2009-2952, 2009.

¹³Ward, M., Culpepper, S., and Costello, M., "Parafoil Control Using Payload Weight Shift," Journal of Aircraft, Vol. 51, No. 1, January-February 2014.

¹⁴ Slegers, N., Beyer, E., and Costello, M., "Use of Variable Incidence Angle for Glide Slope Control of Autonomous Parafoils," Journal of Guidance Control and Dynamics, Vol. 31, No. 3, 2008, pp 585-596.

15 Higgins, M. W., "Control System for Ram Air Gliding Parachute," U.S. Patent 4,175,722.

16 Authority with Upper-Surf

¹⁶ Gavrilovski, A., Ward, M., and Costello, M., "Parafoil Control Authority with Upper-Surface Canopy Spoilers," Journal of Aircraft, Vol. 49, 2012, pp. 1391-1397.

⁷ Bergeron, K., Ward, M., and Costello, M., "Aerodynamic Effects of Parafoil Upper Surface Bleed Air Actuation," AIAA Paper 2012-4737, August 2012.

¹⁸ Bergeron, K., Ward, M., Costello, M., and Tavan, S., "AG100 and Bleed-Air Actuator Airdrop Testing," AIAA Paper 2013-1378, 2013.

¹⁹ Fogell. N., "Fluid-structure interaction simulations of the inflated shape of ram-air parachutes, PhD thesis, Imperial College London, 2014.

²⁰ Bergeron, K., Seidel, J., Ghoreyshi, M., Jirasek, A., Lofthouse, A., and Cummings, R., "Numerical Study of Ram Air Airfoils and Upper Surface Bleed-Air Control," 32nd AIAA Applied Aerodynamics

Conference, AIAA 2014-2832, Jun 2014.

²¹ Ghoreyshi, M., Seidel, J., Bergeron, K., Jirasek, A., Lofthouse, A., and Cummings, R., "Prediction of Aerodynamic Characteristics of Ram-Air Parachutes," 32nd AIAA Applied Aerodynamics Conference, AIAA 2014-2831, Jun 2014.

²² Morton, S. A., McDaniel, D. R., Sears, D. R., Tillman, B., and Tuckey, T. R., "Kestrel: A Fixed Wing Virtual Aircraft Product of the CREATE Program," AIAA Paper 2009-0338, January 2009.

Roth, G. L., Morton, S. A., and Brooks, G. P., "Integrating CREATE-AV Products DaVinci and

Kestrel: Experiences and Lessons Learned," AIAA Paper 2012-1063, January 2012.

²⁴ Grismer, M. J., Strang, W. Z., Tomaro, R. F., and Witzemman, F. C., "Cobalt: A Parallel, Implicit, Unstructured Euler/Navier-Stokes Solver." Advanced Engineering Software, Vol. 29, No. 3-6, 1998, pp. 365-373.

²⁵ Ghoreyshi, M., Seidel, J., Bergeron, K., Jirasek, A., Lofthouse, A., and Cummings, R., "Grid Ouality and Resolution Effects on the Aerodynamic Modeling of Parachute Canopies," AIAA SCITECH Conference, Kissimmee, FL, Jan 2015.

²⁶ Eslambolchi, A. and Johari, H., "Simulation of Flowfield Around a Ram-Air Personnel Parachute

Canopy," Journal of Aircraft, Vol. 50, 2013, pp. 1628-1636.

²⁷ Godunov, S. K., "A Finite Difference Method for the Computation of Discontinuous Solutions of the Equations of Fluid Dynamics", Mat. Sb., 47:357-393, 1959.

²⁸ Gottlieb, J. J. and Groth, C. P. T. (1988). "Assessment of Riemann solvers for unsteady one-

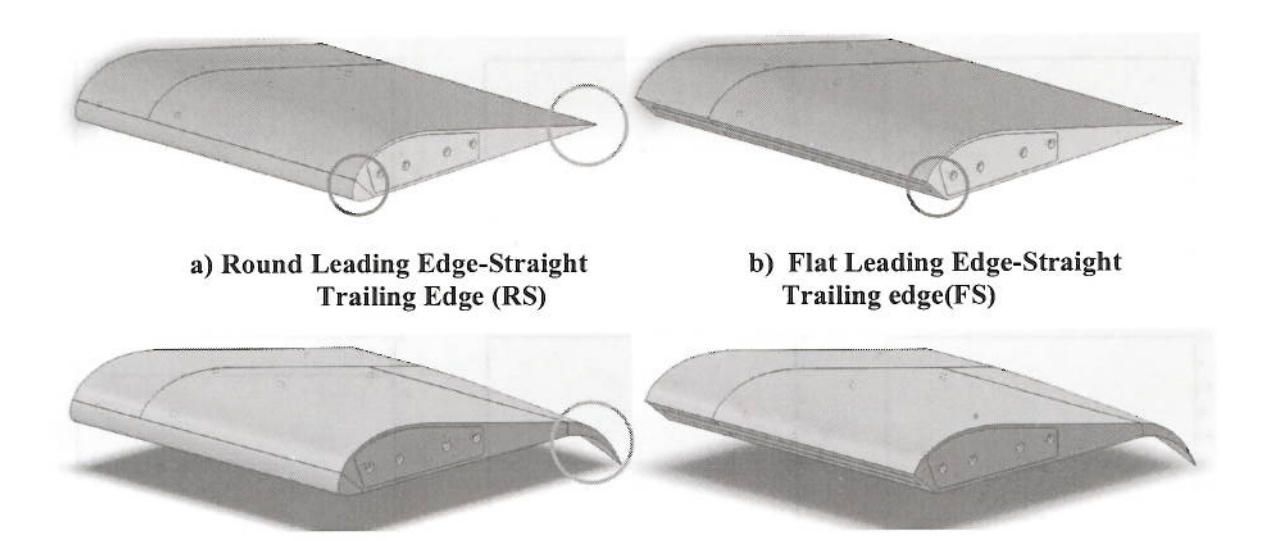
dimensional inviscid flows for perfect gases." J. Comp. Phys., 78(2):437-458.

²⁹ Karypis, G., Schloegel, K, Kumar, V. (1997). ParMETIS: Parallel Graph Partitioning and Sparse Matrix Ordering Library Version 1.0.

³⁰Hiraki, K. and Hidaka, Y., "Aerodynamic Characteristics of Complusively-Inflated Paraglider for

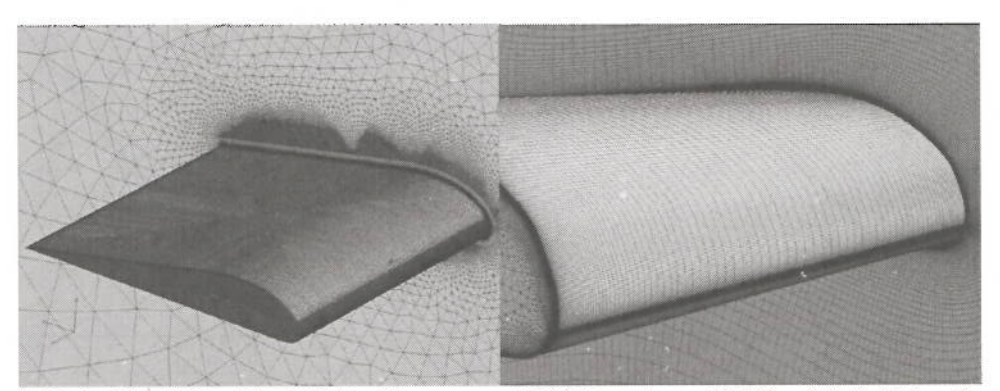
Mars Exploration," AIAA Paper 2013-1305, March 2013.

³¹ Haller, G., "An objective definition of a vortex," J. Fluid Mech. (2005), vol. 525, pp. 1–26.



- c) Round Leading Edge-Asymmetric Trailing Edge Deflection (RB)
- d) Flat Leading Edge-Asymmetric Trailing Edge Deflection (FB)

Figure 1: Solid, Closed Inlet Ram-air Canopy Geometries



- a) Hybrid-RS with 5.9M cells
- b) "Structured" FB with 5.4M cells

Figure 2: Example Meshes

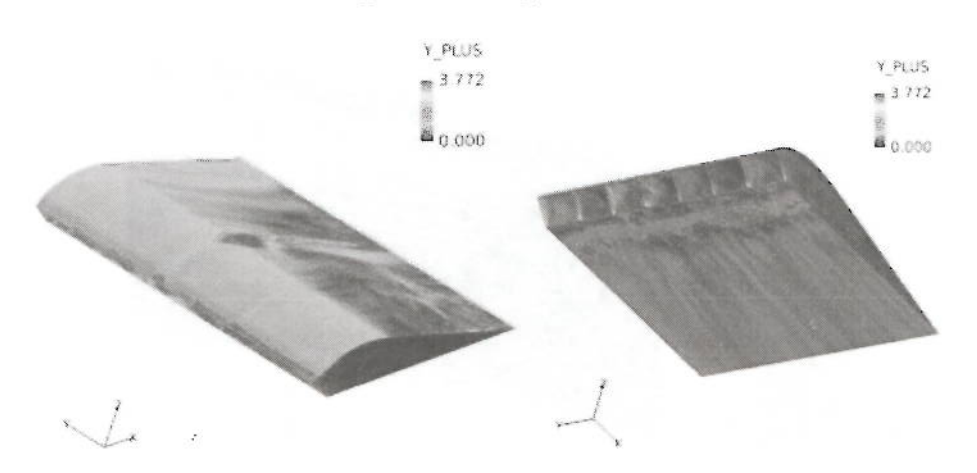


Figure 3: Mesh Quality Example—Open Inlet No TD (OS)

11 of 14

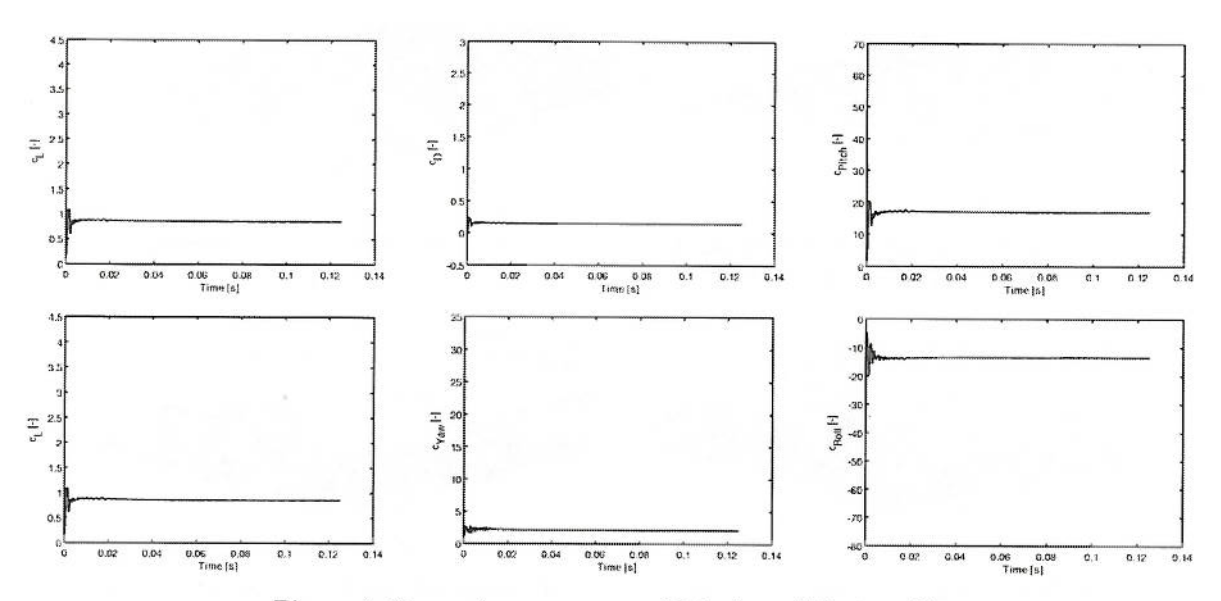


Figure 4: Example convergence histories—FB at $\alpha = 8^{\circ}$.

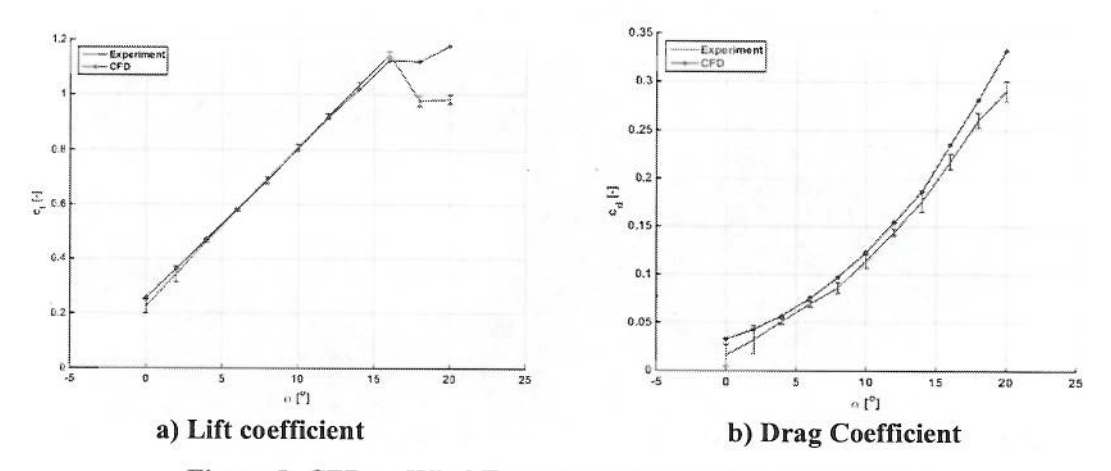


Figure 5: CFD-to-Wind Tunnel comparison for the RS model

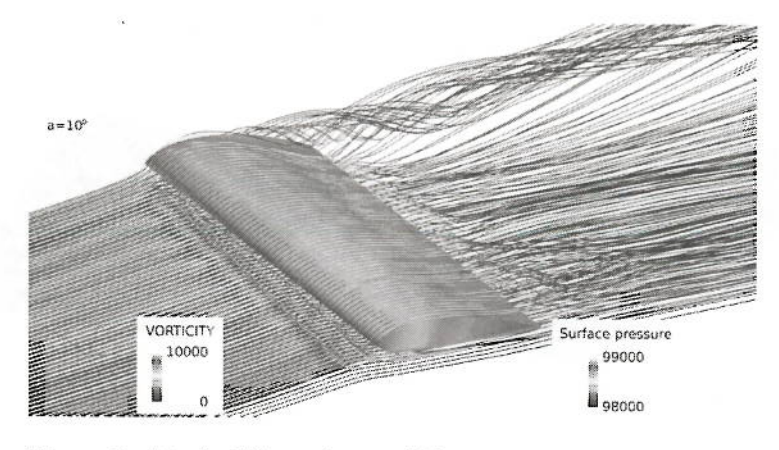


Figure 6: Attached flow about a finite ram-air closed inlet wing 12 of 14

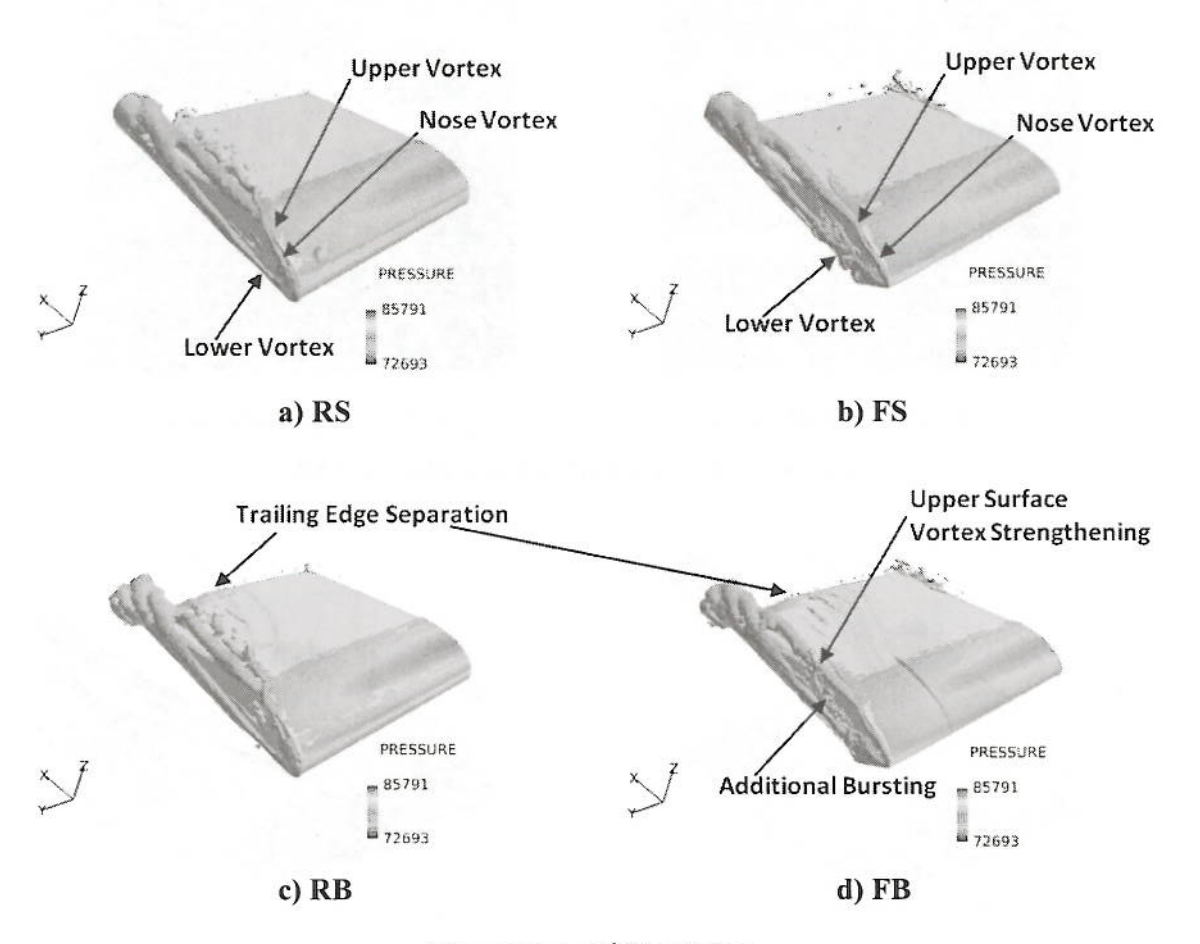


Figure 7: $\alpha = 8^{\circ}$ Simulation

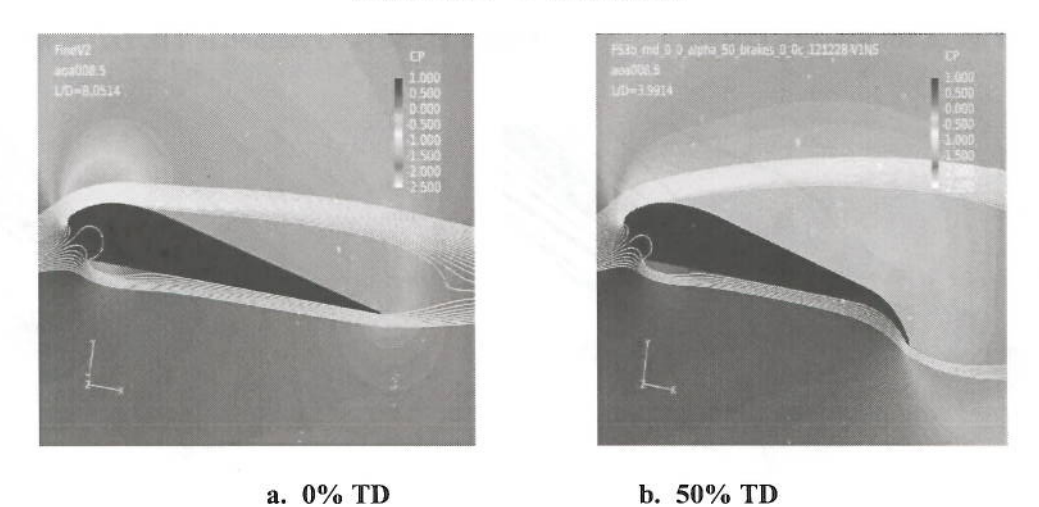
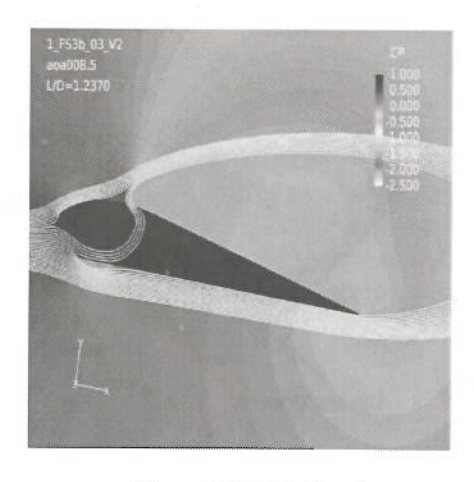
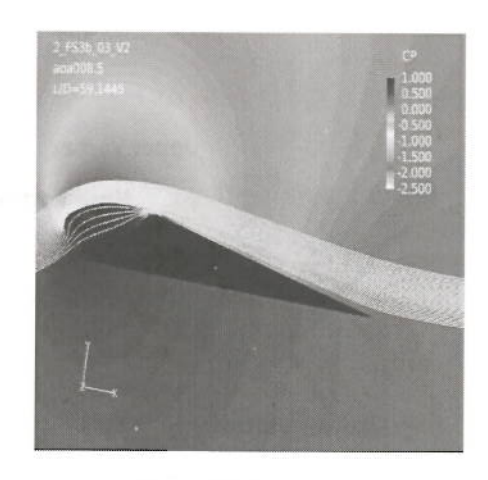


Figure 8¹⁹: 2-D CFD Ram-air Simulations, $\alpha = 8.5$



a. Front-flap Deflection



b. Rear-flap Deflection

Figure 9¹⁹: 2-D CFD Bleed-air Simulations, $\alpha = 8.5$

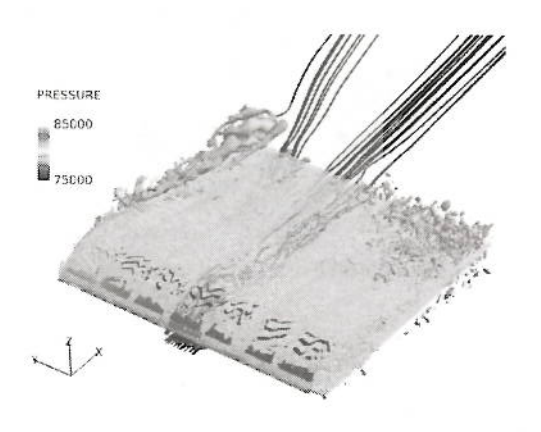


Figure 10: 0% TD, L/D = 6.2

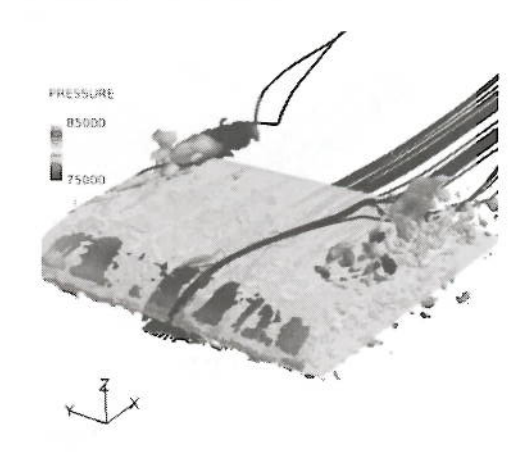


Figure 11: 50% Asymmetric TD, L/D = 4.8

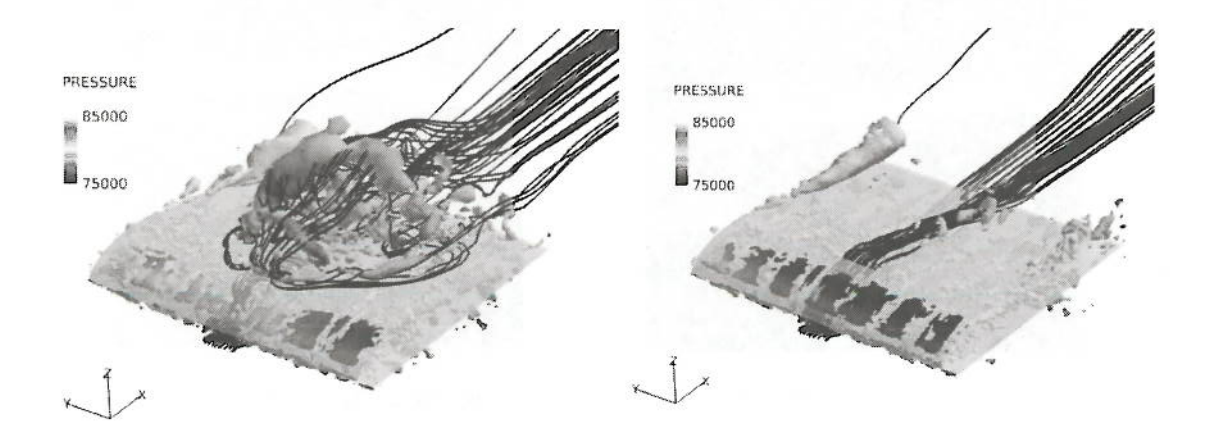


Figure 12: BA Front-flap Deflection, L/D = 3.5

Figure 13: BA Rear-flap Deflection, L/D = 6.1

Grid Quality and Resolution Effects on the Aerodynamic Modeling of Parachute Canopies

Mehdi Ghoreyshi¹, Keith Bergeron², Jürgen Seidel^{1‡} Andrew J. Lofthouse¹, Russell M. Cummings¹

¹ High Performance Computing Research Center, U.S. Air Force Academy USAF Academy, Colorado 80840

² US Army Natick Research, Development, and Engineering Center Natick, MA 01760

This paper provides an overview on the grid quality and resolution effects on the aerodynamic modeling of parachute canopies. The CFD simulations were performed using the Cobalt flow solver on two dimensional canopy sections with open and closed inlets. Previous simulation results of these geometries showed that the grid independence is achieved for the closed and open airfoils with grids containing around half a million and two million cells, respectively. Previous grids were either hybrid with prismatic layers near the walls or multi-block structures using algebraic grid generators. The results presented in this work show that the grid independence of both geometries can be achieved with even much coarser grids. These grids, however, were generated with good smoothness, wall orthogonality, and skewness. Cobalt solver reports an overall and a local quality value for each grid cell. The results show that this quality value is mainly related to the grid smoothness but does not depend on the mesh skewness or the wall orthogonality. Although a smooth grid improves the Cobalt quality value and therefore the solution convergence, but it does not always lead to an accurate solution. For example, the unstructured meshes with anisotropic cells near the wall have very good grid quality in Cobalt, but they have the worst accuracy between the considered meshes because of the mesh poor skewness at the walls. The results also showed that in comparison to the closed inlets, the open geometry solutions are less sensitive to the initial grid spacing and number of constant spacing layers at outside walls. Also, the open inlet solutions do not change with inside mesh resolution and type.

Nomenclature

 C_L lift coefficient, $L/q_{\infty}S$ C_D drag coefficient, $D/q_{\infty}Sc$ c mean aerodynamic chord, m

Distribution A. Approved for Public Release. Distribution unlimited.

^{*}Senior Aerospace Engineer, AIAA Senior Member

[†]Senior Research Aerospace Engineer, AIAA Senior Member

Senior Aerospace Engineer, AIAA Senior Member

[§]Director, AIAA Senior Member

[¶]Professor of Aeronautics, AIAA Associate Fellow

D	drag force, N
GQ	grid quality
GR	growth rate in the viscous layer
L	lift force, N
l	farfield length away from the airfoil, m
M	Mach number, V/a
$N_s \ q_{\infty} \ {q_k}^i$	the number of layers of constant spacing normal to all viscous walls
q_{∞}	dynamic pressure, Pa, $\rho V^2/2$
$q_k{}^i$	k th grid quality metric at i th cell
Re	Reynolds number, $\rho V c/\mu$
t	time, s
V	freestream velocity, m/s
x, y, z	grid coordinates

Greek

Δ_{s1}	the initial spacing at all viscous walls
α	angle of attack, rad
ρ	density, kg/m ³
μ	air viscosity

I. Introduction

The accuracy and expediency of computational fluid dynamic (CFD) solutions depend not only on the underlying numerical methods, but also on the grid generation process, in which the computational domain is discretized into distinct sub-domains. These sub-domains are called cells or grid blocks. The numerical error rises if the physical geometry is not exactly represented by the grid. Also, truncation error and machine round-off error are always present in the numerical solutions of partial or ordinary differential equations. These errors depend on the grid size such that for a finer mesh, the truncation errors decreases, but the rounding errors will increase. Finally, inaccurate interpolation of the discrete solutions between grid blocks will increase the numerical error.

The uniform grids have many advantages over non-uniform grids including a better accuracy and faster convergence.³ However, to resolve boundary layer and wake regions in viscous flows, a uniform grid approach would require a very large number of mesh points, which increases the computational cost. Practical turnaround times for obtaining a CFD solution and availability of computer facilities would limit the uniform grid applicability for three-dimensional (3D) problems. The total number of mesh points, and therefore computational cost, can be reduced by using a non-uniform grid approach, in which the grid points are clustered near the regions of interest and are coarsely distributed elsewhere. However, these non-uniform cells can sometimes lead to grids of locally poor quality that will increase the computational solution error.⁴ The performance of the numerical methods can be significantly reduced even if just a few low-quality cells present.⁵

The grid generation efforts can be traced back to 1960s. Since then many grid generation methods have been proposed such as conformal mapping, algebraic construction, partial differential equation solutions (elliptic, hyperbolic, and parabolic equations), Delaunay, advancing-front, and many others. These methods have been used to generate structured and/or unstructured meshes over simple to complex geometries. Each method leads to a different grid quality to the same geometry. Besides, while some mesh generation methods could be fast and even automated, others are a time consuming manual process.

The conformal mapping is the simplest method of structured grid generation, in which the computational domain is mapped onto a rectangular region. Although, the method is simple and efficient and creates very high quality cells, but it is practical only for two-dimensional simple problems. To create a smooth structured grid, elliptic grid generators can be used, which involve the numerical solution of inhomogeneous elliptic partial differential equations.⁶ Grid smoothness can help reducing the truncation error and improving the accuracy. A disadvantage of the elliptic grid generation is the limited control over the interior grid points. Algebraic methods have also been used to create structured meshes. These methods use algebraic transfor-

mation and an interpolation scheme to distribute grid points from a discrete set of data.⁷ In comparison to elliptic grid generators, algebraic methods require much less computational effort and has better control over grid point locations, but the grid may not be as smooth as an elliptic grid. To improve the interior mesh over complex geometries, the multi-block strategy has been proposed, in which the computational domain is divided into several smaller sub-domains (block) and then separate meshes are generated for each block.⁸ Each block can initially be meshed by an algebraic method and then an elliptic solver be used to smooth the meshes.

Although, structured meshes offer higher accuracy, simplicity, and easy data access compared to an unstructured mesh, but unstructured meshes (using tetrahedra cells) are more popular for complicated geometries. Delaunay and advancing-front methods are the most famous tetrahedral mesh generators. The advancing front creates the cells one by one, starting from the domain boundary and by marching a front toward the interior. The front refers to the cells that meet unmeshed domains; the front will eventually vanish when the mesh is completed. Advancing-front approach will have the best quality cells at the boundaries and the worst cells where the front collides itself. Therefore, this mesh generator is very helpful for modeling inviscid or laminar flows over solid walls. The advancing-front method can even be used to create quadrilateral cells, however, the interior cells could have low quality or the mesh cannot be completed for a complex geometry. Typical Delaunay mesh generators start from a boundary discretization. New points and triangular cells are then added to satisfy a particular connectivity. The method maximizes the minimum angle of all triangles to avoid sharp and distorted cells wherever possible. Delaunay mesh generators, unlike advancing-front method, has the worst cells at the domain boundary and the best cells interior. Therefore, the Delaunay and the advancing front approaches are often combined to use the advantages of both methods.

Unstructured meshes are not much effective when localized regions of high gradients appear in the flow, such as boundary layers. Hybrid grid generators and anisotropic tetrahedral extrusion are commonly used to treat boundary layers in unstructured meshes. The first step of a hybrid approach is the triangulation of the computational domain and then placing prismatic cells near boundary surfaces. The prismatic cells are typically created using an advancing layer scheme. In such a mesh, the outside boundary nearly has isotropic tetrahedral cells. A disadvantage is that prismatic cells may have poor quality near sharp edges. An anisotropic tetrahedral extrusion creates triangular cells in a layer-by-layer fashion with extrusion direction normal to the surface. The method begins with an isotropic tetrahedral mesh (generated by Delaunay and/or advancing-front methods), and tetrahedra on surfaces are then subdivided into anisotropic cells for user-specified number of layers. However, this approach might create extremely stretched tetrahedra cells near the walls which impact the accuracy of computations.

At United States Air Force Academy (USAFA), the hybrid mesh approach has been successfully used for a number of years for CFD simulation of many fighter aircraft. ^{15, 16, 17, 18} These grid have structured cells near solid surfaces and unstructured cells elsewhere. In more details, an inviscid tetrahedral mesh is generated using the ICEM-CFD code. This mesh will then be used as a background mesh by the mesh generator of TRITET^{19,20} which builds prism layers using a frontal technique. TRITET rebuilds the inviscid mesh while respecting the size of the original inviscid mesh from ICEM-CFD. More recently, the authors of this work used this hybrid grid approach for prediction of aerodynamic characteristics of a ram-air parachute. ^{21, 22} The grid sensitivity study showed that solutions are very sensitive to the grid quality and size for the airfoils/wings with an open inlet. For example the airfoil solutions became grid independent for the hybrid grids that have more than 1.7 million cells. That brings to mind a question whether another grid generator could produce similar predictions to the hybrid fine grids, but at a much lower computational cost.

The objectives of the work are twofold: one concerns the grid resolution and to find coarse grids that can have comparable results to the fine meshes. Second, is to understand the relationship between mesh quality and the solution accuracy and convergence. Results are presented for two-dimensional airfoils with open and closed inlet. The airfoil sections is from an actual parachute canopy. The results of two-dimensional airfoils, considered in this work, can be easily generalized to three-dimensional wings. For example, a high quality 3D mesh can be created from spanwise extrusion of a high quality 2D mesh. This work is organized as follows. First the Cobalt flow solver is described. Several grid quality metrics are also reviewed. Next, the test case is presented. Finally, the simulation results will be discussed.

II. CFD Solver

Cobalt solves the unsteady, three-dimensional, compressible Navier-Stokes equations in an inertial reference frame. Arbitrary cell types in two or three dimensions may be used; a single grid therefore can be composed of different cell types.²³ In Cobalt, the Navier-Stokes equations are discretized on arbitrary grid topologies using a cell-centered finite volume method. Second-order accuracy in space is achieved using the exact Riemann solver of Gottlieb and Groth,²⁴ and least squares gradient calculations using QR factorization. To accelerate the solution of the discretized system, a point-implicit method using analytic first-order inviscid and viscous Jacobians is used. A Newtonian sub-iteration method is used to improve the time accuracy of the point-implicit method. Tomaro et al.²⁵ converted the code from explicit to implicit, enabling Courant-Friedrichs-Lewy (CFL) numbers as high as 10⁶. In Cobalt, the computational grid can be divided into group of cells, or zones, for parallel processing, where high performance and scalability can be achieved even on ten thousands of processors.²⁶ Some available turbulence models in Cobalt are the Spalart-Allmaras (SA) model,²⁷ Spalart-Allmaras with Rotation Correction (SARC),²⁸ and Delayed Detached-eddy simulation (DDES) with SARC.²⁹

Cobalt checks the grid quality and reports a score; this score is directly related to a particular part of the second-order accurate spatial operator inside Cobalt.³⁰ The reported score is averaged from all the cells and ranges from zero to hundred, such that the lower the grid score, the more numerical dissipation is added to the solution (worse stability). Note that Cobalt's grid score involves the mesh geometry information only, and not the flow solution obtained on that mesh. This means that the grid quality is a fixed number regardless of the angle of attack and Mach number. Cobalt's User Guide³⁰ details that the high aspect ratio of cells (typically placed in the boundary layer) can cause the quality to suffer. Also regions of high surface curvature can adversely impact grid quality. The grid quality will improve if a sufficient number of surface cells are used to accurately capture any geometric curvature.

III. Grid Quality

The relationship between the mesh quality and solution accuracy will be investigated in this work. A priori grid quality metrics could provide some guidance of the grid before running it in CFD.³¹ The mesh quality mainly deals with the geometric information of the grid. Before examining the grid quality, one should check the grid for negative volume (or volumes below a threshold) and folded cells. These type of cells make a cell-centered flow solver impossible to iterate.³² Typically, a high quality mesh is obtained by creating well-shaped cells (orthogonal structured cells or isotropic tetrahedra cells) with moderate smoothness. Therefore, most grid quality metrics indicate how much a grid cell deviates from its ideal shape.

A great, but more advanced, way to improve the grid quality metrics is to add information about the numerical solution obtained on the mesh.⁴ One simple example is Y^+ values at the walls. According to the gridding guidelines from the 2nd AIAA CFD high lift prediction workshop,³³ approximate initial spacing normal to all viscous walls should have Y^+ values of approximately 1.0, 2/3, 4/9, and 8/27 for a coarse, medium, fine, and extra fine grid, respectively. In more advanced grid generation methods, the solution errors are used to refine the mesh in regions where the error is large.

Mesh resolution and quality should be checked prior to running the grid in CFD. The mesh resolution should be high enough to capture the flow physics. Mavriplis et al,³⁴ for example, have recommended a chordwise grid spacing of 0.1% of local chord (for a medium grid) at the wing leading and trailing edges. In the spanwise direction at the wing root and tip, a grid spacing of 0.1% of semispan was recommended. The number of recommended cells at the wing trailing edge base are 8, 12, 16, 24 for a coarse, medium, fine, and extra fine grid, respectively. The grid resolution can be evaluated by sensitivity studies. The results become mesh independent if they show less than 3% difference from a 30% finer mesh.³⁵

The grid quality is often measured for each cell from given information about the cell's aspect ratio and skewness. It is also desirable to have near-wall faces parallel to the wall. Besides, the rate at which the grid spacing changes from one cell to another (grid smoothness) is important. Optimal grids have equilateral cells (equilateral triangles and squares) with a smooth change of dimensions through the domain.³⁵ In more details, cell skewness should be kept minimum. High aspect ratios would slow down the convergence. Finally, a spacing growth rate below 20% does not affect the solutions,³⁵ but higher values affect the solution accuracy and convergence. The reader should note that these criteria might change from one solver to another. This is discussed later in this section.

There are some available grid quality metrics. Alter, ³⁶ for example, has described a grid quality metric for structured three-dimensional grids. This metrics is defined by,

$$GQ = \frac{\bar{\theta}_{\min}\bar{\Theta}}{\bar{\epsilon}_{\max}} \tag{1}$$

where GQ denote the grid quality ranging from 0 to one; $\bar{\theta}_{\min}$, $\bar{\Theta}$, and $\bar{\epsilon}_{\max}$ show deviations from orthogonality, straightness, and stretching, respectively. Best grid quality comes with GQ = 1. The minimum of the average skewness, $\bar{\theta}_{\min}$, is determined in three directions by

$$\theta \mid_{\xi = \text{constant}} = \frac{2}{\pi} \cos^{-1} \left(\frac{\vec{r}_{\eta} \cdot \vec{r}_{\zeta}}{|\vec{r}_{\eta}| |\vec{r}_{\zeta}|} \right)$$
 (2)

$$\theta \mid_{\eta = \text{constant}} = \frac{2}{\pi} \cos^{-1} \left(\frac{\vec{r}_{\xi} \cdot \vec{r}_{\zeta}}{|\vec{r}_{\xi}| |\vec{r}_{\zeta}|} \right)$$
 (3)

$$\theta \mid_{\zeta = \text{constant}} = \frac{2}{\pi} \cos^{-1} \left(\frac{\vec{r}_{\xi} \cdot \vec{r}_{\eta}}{|\vec{r}_{\xi}| |\vec{r}_{\eta}|} \right) \tag{4}$$

where its value is zero and minimum for a collapsed cell and is one and maximum for an orthogonal edge segment. The straightness, $\bar{\Theta}$, measures the extra distance traversed between the wall and the outer boundary and is computed normal to the boundary as

$$\bar{\Theta} = \frac{S \mid_{(\zeta_{\min} \to \zeta_{\max})}}{\sum_{\zeta=1}^{\zeta_{\max}} \mid \vec{r} \mid_{\zeta}}$$
(5)

where the grid line straightness ranges from zero to one, where zero is for a grid line that begins and ends at the same point. Finally, the maximum average planar stretching, $\bar{\epsilon}_{\max}$, measures the spacing of one point to the next in all three directions and is given by

$$\epsilon_{\xi} = \frac{\max(|\vec{r}_{\xi}|^{+}, \vec{r}_{\xi}|^{-})}{\min(|\vec{r}_{\xi}|^{+}, \vec{r}_{\xi}|^{-})}$$
(6)

$$\epsilon_{\eta} = \frac{\max(|\vec{r}_{\eta}|^{+}, \vec{r}_{\eta}|^{-})}{\min(|\vec{r}_{\eta}|^{+}, \vec{r}_{\eta}|^{-})}$$
(7)

$$\epsilon_{\zeta} = \frac{\max(|\vec{r}_{\zeta}|^{+}, \vec{r}_{\zeta}|^{-})}{\min(|\vec{r}_{\zeta}|^{+}, \vec{r}_{\zeta}|^{-})}$$
(8)

where each term ranges from one as minimum to infinity. The minimum refers to a uniform spacing. An abrupt change in the spacing increases the stretching value. Alter's examples of orthogonality, stretching, and straightness are shown in Figure 1. For quadrilateral (two-dimensional) meshes, Dannenhoffer³¹ defined below quality metrics:

$$skew = \frac{\min(d_1, d_2)}{\max(d_1, d_2)}$$

$$(9)$$

taper =
$$\min\left(\frac{s_1}{s_3}, \frac{s_3}{s_1}, \frac{s_2}{s_4}, \frac{s_4}{s_2}\right)$$
 (10)

aspect ratio =
$$\frac{\min(s_1 + s_3, s_2 + s_4)}{\max(s_1 + s_3, s_2 + s_4)}$$
(11)

stretch =
$$\sqrt{\frac{\min(A_1, A_2, A_3, A_4)}{\max(A_1, A_2, A_3, A_4)}}$$
 (12)

where s_1 , s_2 , s_3 , and s_4 are the lengths of the adjacent sides around the cell; d_1 and d_2 are the lengths of two diagonals, and A_1 , A_2 , A_3 and A_4 are the areas of four cells that surround a node. All these metrics are computed at each cell and then are added to find the overall grid quality.

A grid quality metrics based on the deviation from an ideal cell shape will probably invalidate most of anisotropic cells near the walls for viscous flows. On the other hand, these anisotropic cells are allowed and acceptable in many flow solvers. In addition, for all cell-centered flow solvers, the quadrilateral faces should be planar, however, non-planar faces are not an issue in most node-based solvers. McDaniel³² in his PhD dissertation, therefore, proposed that an independent mesh quality should be provided from the viewpoint of each flow solver (cell-centered, node-based and others). He then introduced grid quality metrics for the kCFD code³⁷ which solves the unsteady, three-dimensional, compressible RANS equations on hybrid unstructured grids. Note that both Cobalt and kCFD code originated from the Air Vehicles Unstructured Solver (AVUS, formally known as Cobalt60²⁴), which is a parallel, implicit, unstructured flow solver developed by the Air Force Research Laboratory. Both solvers have since been highly modified. McDaniel then defined some grid quality metrics which are applicable to the most cell-centered numerical algorithms and all cell types and take into account the fact that large-area faces have a larger flux contribution to the solution value in the cell. All metrics, also, lie in the range from zero to one, while one represents the maximum quality. Some of these quality metrics are briefly reviewed in this paper.

Assume that there are no folded and negative volume cells. A planarness metric is defined for the j^{th} face of the i^{th} cell as

$$q^{i}_{\text{planar},j} = \begin{cases} 1 & \text{face nodes } \leq 3\\ \left[1 - \frac{\cos^{-1}(\hat{n}_{j,1}.\hat{n}_{j,2})}{\pi}\right] & \text{face nodes } = 4 \end{cases}$$
 (13)

where $\hat{n}_{j,1}$ and $\hat{n}_{j,2}$ are the unit-normal vectors to each face. The cell planarness metric is then calculated as:

$$q^{i}_{\text{planar}} = \frac{1}{\sum_{j} A_{j}^{i}} \sum_{j=1}^{\text{No. faces}} A_{j}^{i} q^{i}_{\text{planar},j}$$

$$\tag{14}$$

 $A_j{}^i$ denotes jth face area of the ith cell. Figure 2 (a) gives the planarness metric values for some example cells. The skew-smoothness metric for the jth face in the ith cell is also defined as

$$q^{i}_{\text{skew-smooth},j} = \left[\frac{\min\left(|\bar{\nu}_{\text{left},j}|,|\bar{\nu}_{\text{right},j}|\right)}{\max\left(|\bar{\nu}_{\text{left},j}|,|\bar{\nu}_{\text{right},j}|\right)} \right] \left[\frac{1}{2} \left(1 - \left[\hat{\nu}_{\text{left},j}.\hat{\nu}_{\text{right},j} \right] \right) \right]$$
(15)

 $\bar{\nu}_{{
m left},j}$ and $\bar{\nu}_{{
m right},j}$ are the vectors from the adjoining left and right cell centroids, respectively, to the centroid of the jth face of the cell. $\hat{\nu}_{{
m left},j}$ and $\hat{\nu}_{{
m right},j}$ are the corresponding unit vectors. The first and second terms of equation 15 correspond to the degree of smoothness and skewness across a particular face, respectively. The cell skew-smoothness metric can be calculated using eq. 14. If the cell is folded then $q^i_{{
m skew-smooth},j}=0$. The skew-smoothness metric values for some example cells are given in Figure 2 (b).

A flow alignment (wall orthogonality or straightness) metric was also defined to measure the degree to which cell faces are parallel to the solid walls. The flow alignment metric for the jth face in the ith cell is

$$\tilde{q}_{\text{align},j}^{i} = \frac{\cos^{-1}\left(\operatorname{abs}\left(\hat{n}_{\text{wall}}.\hat{n}_{\text{face},j}^{i}\right)\right)}{\pi/2}$$
(16)

$$q^{i}_{\text{align},j} = 2 \left[\max \left(\tilde{q}^{i}_{\text{align},j}, 1 - \tilde{q}^{i}_{\text{align},j} \right) - 0.5 \right]$$

$$(17)$$

 \hat{n}_{wall} is the unit normal of the closest solid wall boundary face and $\hat{n}_{\text{face},j}^i$ is is the unit normal of the jth face. Some flow alignment metric examples are shown in Figure 2 (c). Other quality metrics include isotropy and spacing metrics which measure the deviation from an "equilateral" cell shape and uniformity in the mesh, respectively. The global grid quality is then estimated by

$$GQ = \sum_{k=1}^{\text{No of metrics}} P_k \left[\sum_{i=1}^{\text{No of cells}} w \left(\bar{s}_k, \hat{d}_{\text{wall},i} \right) q_k^{i} \right]$$
(18)

where P_k is the global weight for the kth quality metric; $q_k{}^i$ is the kth quality metric value for the ith cell; $w\left(\bar{s}_k, \hat{d}_{\text{wall},i}\right)$ is a weighting function for each quality metric which depends on through parameter \bar{s}_k and $\hat{d}_{\text{wall},i}$, the minimum distance of the ith cell centroid from the solid wall boundary, normalized by the characteristic length for the mesh.

IV. Test Cases

The U.S. DoD program to develop precision guided airdrop systems is known as the Joint Precision Airdrop System (JPADS) which is coordinated by the U.S. Army Natick Soldier Center (NSC). The JAPDS uses round and ram-air parachutes (parafoils) for deceleration and control of the payload. Different type of airfoil sections have been used for parafoils: initial ram-air canopies used the Clark-Y section which has good lift-to-drag (L/D) characteristics for medium Reynolds number, Re, flows. Over the years this airfoil shape has been modified for parachute applications to improve lift-to-drag ratio; recent canopy designs are based on the airfoil sections used in glider design (for example NASA LS1-0417 airfoil). In this work, low-speed airfoil section of an actual parafoil is investigated. The airfoil, considered here, is a non-symmetric airfoil that has a flat bottom surface. The flow around this airfoil has been studied by Ghoreyshi et al. 21,22 for opening and closing the inlet; the open and closed-inlet geometries are shown in Figure 3.

Ghoreyshi et al.²¹ performed the mesh-independent study of both airfoils. These results are shown in Figures 4 and 5. Closed airfoil grids are fully structured or hybrid; structured grids were generated using the multi-block techniques inside the commercial code of Pointwise V17.01.R3. Hybrid meshes were generated using ICEM-CFD code and the mesh generator of TRITET. All the meshes labeled in Figure 5 are hybrid type.

Figure 4 shows that solutions of structured medium (around 663,000 cells) and fine meshes (around 3 million cells) match everywhere. The solutions of the hybrid medium mesh (around 744,000 cells) are in close agreement with the medium and fine structured meshes as well. The coarse structured mesh (around 172,000 cells), however, only matches the solutions up to an angle of 6°; at higher angles, it predicts smaller lift and larger drag coefficients. The closed airfoil is further investigated in this work. This geometry is used to determine if predictions of a low-resolution, but high-quality mesh can still match with the medium

and fine grid data. The second goal is to relate the solution accuracy and convergence with grid parameters and quality metrics. All meshes of this work were generated using the Pointwise code and predictions were compared with solutions of the fine structured grid (containing 3M cells). Cobalt reports an averaged grid quality of 99.74 in a range of zero to 100 for this fine grid.

Figure 5 shows that CFD solutions of the open-inlet airfoil largely depend on the grid resolution. Coarse and medium meshes (containing around 452,000 and 528,000 cells) were generated from a low-density inviscid grid and CFD data using these grids do not match with fine meshes data (containing around 943,000, 1.7 million, and 2.45 million cells). Figure 5 shows that solutions do not change with grid density for the grids that have more than 1.7 million cells (see fine1 and fine2 plots in the figure). The open-inlet airfoil is also used in this work. The coarse meshes, with different grid generation methods, will be tested in Cobalt and the results will be compared to fine1 mesh data in Ref. 21. This grid has a Cobalt quality of 99.83. The meshing study will be performed on both outside and inside domains. The effects of meshing on the solution accuracy and convergence will be investigated.

V. Results and Discussion

For the sake of convenience, the closed and open inlet grids are labeled "CG" and "OG", respectively. All CFD simulations were performed using the Spalart-Allmaras (SA) turbulence model and were run on the Cray XE6 machine at the Engineering Research Development Center (ERDC). The free-stream velocity in all simulations was fixed at Mach 0.1 and the Reynolds number is 1.4×10^6 at standard sea level conditions. The simulation were performed for an angle-of-attack sweep from zero to ten degrees with one degree increment. In all simulations, second-order accuracy in time, 3 Newton sub-iterations, and 20,000 iterations with a time step of 1e-4 seconds were used. The last 10,000 iteration values were averaged to obtain overall lift and drag coefficients.

All grids were run in Cobalt and errors in the force coefficients from the predictions of fine meshes are estimated. In more details, the error norm of lift coefficient (C_L) , drag coefficient (C_D) , and lift to drag ratio (L/D) is defined as:

$$err = \frac{\sqrt{\frac{1}{N_i} \sum_{j=1}^{N_i} (y_j^{\text{NewGrid}} - y_j^{\text{FineGrid}})^2}}{|y^{\text{FineGrid}}(max) - y^{\text{FineGrid}}(min)|} \times 100$$
(19)

where $y = [C_L, C_D, L/D]$; N_i is number of angles of attack which is 11 in this work. The error norm is also found for the maximum lift coefficient $(C_{L_{max}})$ as

$$err = \frac{C_{L_{\max}}^{\text{NewGrid}} - C_{L_{\max}}^{\text{FineGrid}}}{C_{L_{\max}}^{\text{FineGrid}}} \times 100$$
 (20)

First, results are presented and discussed for the closed-inlet grids. A medium size grid (named CG1) was generated with details given in Table 1. The grid was generated layer by layer using an elliptic extrusion method starting from the walls. The method stops when the new grid layer reaches a total height of 200m. The outer edges of the cells, at the final layer, define the freestream boundary. The coarse grid used in Ref. 21 was also modified to have exactly the same number of grid points and spacings on the walls as the CG1 mesh has. This new grid (named CG2), however, was generated using a multi-block method with an algebraic grid generator applied to each block. Grid details are also given in Table 1. Table 1 confirms that CG1 and CG2 grids have nearly equal number of cells. The grid overview near trailing edge is shown in Figure 6.

Table 2 compares Y^+ , Cobalt grid quality, and the error norms of CG1 and CG2 grids. While both grids have approximately the same resolution, Y^+ , and grid quality, but the errors from CG1 are one order of magnitude less than CG2 grid. In more details, Figure 7 compares the lift and drag coefficients of CG1 and CG2 grids with the fine grid data of Figure 4. The comparisons show that CG1 grid perfectly matches with the fine grid predictions, however, CG2 predictions do not match everywhere. A question that arises is why

these grids, both structured, with the same Y^+ , grid quality, and resolution lead to different answers to the exact same problem.

Prior to answer this question, let's first examine the convergence solution of CG1 and CG2 grids. Figure 8 shows the convergence histories of the density residual $(D\rho/Dt)$ for CG1 and CG2 grids as well as the fine mesh containing 3M cells. From this figure, it can be seen that both CG1 and CG2 grids reached converged values with approximately 3.0 order of magnitude reduction in the density residual. Figure 8 also indicates that both grids exhibit very similar convergence behavior. Since CG1 and CG2 have the same quality and resolution, a preliminary conclusion is that solution convergence in Cobalt is related to the grid quality and the resolution; this will be further examined later for more grids. The fine mesh quality in Cobalt is 99.74 slightly higher than CG1 and CG2; also it is a very high spatial resolution grid. As expected, Figure 8 shows that the fine mesh has better convergence than other grids.

Now, in attempting to answer the aforementioned question, the reader is referred again to the mesh overviews shown in Figure 6. Detailed visualization of the cells around the trailing edge reveals that CG1 has better wall orthogonality (straightness), smoothness, and skewness compared to CG2. Many cells in CG2 are highly skewed; besides most mesh lines are not orthogonal to the walls. However, Cobalt's overall grid quality is very similar for both grids. The grid quality plots of CG1 and CG2 (around the trailing edge) can also be seen in Figures 9 (a) and (b). Note that white color cells in the figures indicate high grid quality (above 99). Figure 9 (b) shows that most CG2 cells in Cobalt have high quality while they were expected to have low quality because of the poor flow alignment and skewness.

Grid smoothness and skewness values from Pointwise are also shown in Figure 9. This figure shows that CG1 cells are well-shaped with good smoothness. Comparing Pointwise plots with Cobalt grid quality pictures reveals that Cobalt grid quality is related to the grid smoothness, but not the skewness or the wall orthogonality. Figure 10 shows the same correspondence for the cells near the leading edge. CG2 cells at the leading edge have slightly better smoothness than CG1, but it has highly skewed cells. Figure 10 shows that Cobalt's quality (at the leading edge) is better for CG2 compared to CG1 cells. This again confirms that Cobalt grid quality does not change with the skewness or wall orthogonality. This means that a high grid quality in Cobalt corresponds to good smoothness which would improve the convergence but it does not necessarily provide a better accuracy.

Four new grids (CG10 - CG13) were generated around the closed-inlet airfoil by the normal extrusion of the wall using an elliptic mesh generator. The edge lengths of these grids are about half-size of the edges in CG1 and CG2 grids. All grids are structured and contain around 120,000 cells. The near-wall grid spacing (Δ_{s1}) is 4e-5m for these grids which makes overall Y^+ near one. The difference between these four grid is only due to the farfield length(l); it varies from 25 to 100 chord lengths. Grid details and errors (with the fine mesh) are given in Tables 1 and 2.

Figure 11 (a) shows that CG10-CG13 grids have very similar convergence behavior; again, because these grids have the same resolution and quality. Figure 11 (a) shows that the farfield length had no considerable effect on the convergence rate in Cobalt. Figure 11 (b) also shows the error trends with farfield length for grids CG10 - CG13. Increasing the farfield length above 50 chord length does not change much the C_L , C_D and $C_{L\text{max}}$ errors; Figure 11 (b) shows that L/D predictions can be improved by making the farfield boundary bigger but its impact becomes smaller above 50c. For all subsequent grids, a farfield length of 50 chord will therefore be used.

CG20-CG21 grids were generated by similar mesh generation methods, however, the near-wall grid spacing (Δ_{s1}) varies in these grids. The convergence data of these grids (CG20 - CG21) are shown in Figure 12 (a) which shows the convergence improves as Y^+ decreases from one to around 0.2 (CG11 in this figure has $Y^+=1$). The solution accuracy is also improved with decreasing Y^+ as shown in 12 (b). Figure 13 also compares the lift and drag coefficient predictions of CG21 grid ($Y^+=0.2663$ and containing 134,000 cells) with predictions from CG1 ($Y^+=0.2663$ and containing 341,000 cells). The results show that CFD data of the coarse grid match very well with the medium grid data. Note that CG1 data also match with CFD data of the fine grid. These results show that a grid size of around 134,000 cells and $Y^+=0.26$ with well-shaped cells will match the fine data of Ref. 21.

Three unstructured meshes (CG30-32) were also considered; these meshes were generated by the Delaunay tetrahedralization and have anisotropic cells near the wall with a growth rate of 1.1. These grids are very similar, except that they have different initial spacing near the wall. Gird details and errors are given in Tables 1 and 2. These grids have around 115,000 cells and have grid quality above 99. Figure 14 compares CG21 (structured) with the CG32 (unstructured). The anisotropic cells near the wall can be seen in this

figure. Note that anisotropic tetrahedral layers are not constant everywhere; the local extrusion at each point would stop if the cell size become close to the size of outside isotropic cells.

Figure 15 compares cobalt quality plot of CG32 with the Pointwise skewness quality picture of CG32. Figure 15(b) shows that the cells near the wall are extremely skewed, but Cobalt considers these cells high-quality ones because of the grid good smoothness. The convergence history of CG1, CG21, and CG32 are plotted in Figure 16. Despite having a poor skewness near the wall, CG32 has very similar convergence behavior to CG21 which is a structured grid. This again confirms that Cobalt convergence does not change much with the skewness quality. CG1 has better convergence than the other grids because it is a high-resolution compared with CG21 and CG32.

Although CG32 and CG21 have similar quality and convergence, but Table 2 shows that CG32 has much larger errors in the lift and drag coefficients than CG21. In more details, Figure 17 compares the lift and drag values for grids of CG1, CG21, and CG32. Figure 17 shows that CG32 match well with CG21 and CG1 data at small angles of attack; however, for angles above 6° , CG32 lift overestimates CG21/CG1 data and CG32 drag underestimates them. Finally, for the structured grids of CG11, CG20, and CG21, Table 2 shows that the accuracy is improved by decreasing Y^+ from one to 0.26; this, however, does not apply to the unstructured grids. Decreasing the initial spacing makes the cells near the wall more skewed assuming the wall spacing is unchanged. Poor skewness would impact the solution accuracy.

Final closed girds considered are hybrid type with prismatic layers near the wall and isotropic cells elsewhere. Three hybrid grids of CG40, CG41, and CG42 were generated. The prismatic layers were generated by the wall normal extrusion using an elliptic solver. The outer domain is then meshed by the Delaunay tetrahedralization. These grids are much coarser than the structured grids of CG10 to CG21. Gird details and errors are gain given in Tables 1 and 2. The main difference between these grids is the number of prism layers. Figure 18 shows the mesh overview of CG2 with 75 prism layers. The effects of the number prism layers on the errors can be seen in Figure 19 which shows the accuracy is significantly improved by increasing the layers from 25 to 50; however, the accuracy does not change much by increasing layers from 50 to 75. Figure 20 also compares the lift and drag coefficients of the hybrid CG42 mesh with predictions of CG1 and CG21 grids. The results show that predictions from a hybrid grid with 75 prism layer still match quite well with expected data.

Next, results are presented for the open-inlet geometry. The computational domain of this geometry consists of two parts corresponding to the outside and inside of the airfoil. These domains are meshed separately in this work. First grids considered are structured; outside mesh was generated by the wall normal extrusion and the inside mesh is an algebraic mesh nearly uniform in spacing even at the inside walls. These meshes are named OG1- OG5. All these grids have the same inside mesh containing around 278,000 cells inside. OG1- OG3 have the initial spacing of 4e-5m at the outside walls but they have different number of layers of constant spacing. OG4 and OG5 have 5 layers of constant spacing at the outside walls but the initial spacing of these meshes are 2e-5m and 1e-5m, respectively. OG1 mesh at the leading and trailing edges of the airfoil is shown in Figure 21. OG1 has 25 layers of constant spacing at the outside walls which can easily be seen in Figure 21.

OG1 to OG5 grids contain around 400,000 cells. Figure 22 (a) shows the convergence histories of OG1, OG2, and OG3 grids compared with the hybrid fine mesh (1.7M cells) convergence. The convergence comparisons show that all coarse grids converged to the same values; again due to having similar resolution and quality. In comparison to the closed-inlet airfoil convergence plots, Figure 22 (a) shows that the open-inlet take a longer time to converge. Also, Figure 22(a) shows that the fine grid convergence is not significantly different from the coarse grids.

The effects of the number of constant-spacing layers, at the wall, (N_s) on the errors are shown in Figure 22 (b). The results show that N_s has small effects on the open-inlet solutions. In more details, the lift and drag coefficients of OG1, OG2, and OG3 grids are compared with the fine mesh predictions in Figure 23. The lift and drag coefficients are split into the inner and outer surfaces. Notice that inner lift does not change with the angle of attack; Ghoreyshi et al²¹ showed that flow is stationary inside with stagnation pressures almost everywhere. Figure 23 (b), however, shows that the outer surface has negative drags before stall angle and the inner surface has very large drag. The comparison plots of Figure 23 show that coarse grids with uniform spacing inside match very well with the fine mesh force coefficients at inside and outside walls.

OG2, OG4, and OG5 have around 278,000 cells inside and very similar grids outside; in these grids $N_s = 5$ and growth rate is 1.1. However, the initial grid spacing is different; Y^+ values of these grids are given in Table 4 and ranges from one for the OG2 to 0.23 for the OG5. The effects of Y^+ on the errors are

shown in Figure 24 and compared with trends of closed-inlet solutions. Figure 24 shows that the errors of the open-inlet grids are slightly reduced by decreasing Y^+ , however, the errors of all Y^+ values considered are small and less than 2%. On the other hand, the solution accuracy of the closed-inlet grid significantly changes with Y^+ .

OG5, OG10, OG11, OG12 grids were used to study the effect of inside mesh resolution on the overall solutions. All these grids nearly have very similar mesh outside but inside mesh changes from 278,000 to 22,000 cells. This is achieved by reducing the inside wall grid dimensions. OG12 has only 22,000 cells inside and the gird is shown against OG5 with 278,000 cells in Figure 25. Figure 26(a) shows that OG12 will less cells has density residual to a larger value than OG5 and the fine mesh; however, the accuracy is still as good as others as shown in Figure 26(b) which shows OG12 errors from the fine mesh are less than 1%. This means that open-inlet solution is not much sensitive to the number of cells inside.

Figure 27 shows the flow solutions of the closed and open inlet at $\alpha=8.5^{\circ}$. This figure shows that the flow inside airfoil is stationary almost everywhere; therefore the flow solution should not change much with inside mesh resolution. These investigate the inside mesh type on the solution OG20 and OG21 grids were generated; these grids again have structured mesh outside same as previous meshes, but the inside was meshed by the Delaunay tetrahedralization. OG20 has only 9,800 tetrahedra cells inside; the grid is shown in Figure 28(a). Table 4 and Figure 29 show that OG20 with coarse tetrahedra cells inside still match with the fine data. Therefore solutions not much depend on the inside cell resolution as well as type.

OG22 mesh has unstructured cells inside and outside. The outside is meshed by the Delaunay tetrahedralization and has anisotropic layers at the wall. Inside cells are uniform isotropic tetrahedra cells. The mesh and solutions are shown in Figure 28(b) and Figure 29, respectively. Figure 29 shows that outer surface and therefore total lift and drag do not match with fine data everywhere. This is probably due to having highly skewed cells near the outer walls.

Final grid, OG40, is a hybrid mesh outside and unstructured inside. Viscous layers at outside wall were generated by the wall normal extrusion; it has 75 layers. The rest of outside domain is meshed by the Delaunay mesh generator. The grid overview is shown in Figure 30. The lift and drag coefficients of this grid are compared with the fine and OG1 mesh in Figure 31 which shows hybrid grid match well with other grids data; there are very small discrepancies in lift coefficients in the post-stall region.

VI. Conclusions

This paper provides an overview on the grid quality and resolution effects on the aerodynamic modeling of parachute canopies. The CFD simulations were performed using the Cobalt flow solver on two dimensional canopy sections with open and closed inlets. The simulation results show that Cobalt grid quality (ranging from zero to 100) depends mainly on the mesh smoothness, but not the skewness or the wall orthogonality. Cobalt convergence is improved with increasing grid resolution, grid quality (smoothness) and decreasing initial grid spacing at the wall (Y^+) . The results showed that while a high quality grid of Cobalt leads to a better convergence, but is does not always lead to a better accuracy. The solution accuracy will change with grid resolution and smoothness, as well as skewness and the wall orthogonality.

The results of this work showed that the solutions of coarse structured and hybrid grids (around 100,000) match well with prediction of fine meshes containing a few million cells. These grids have appropriate Y^+ values, good smoothness, skewness, and wall orthogonality. While unstructured meshes with anisotropic cells near the wall have very good grid quality in Cobalt but they have the worst accuracy between considered grids because of poor skewness at the walls. The results also showed that in comparison to the closed inlets, the open geometry solutions are less sensitive to the initial grid spacing and number of constant spacing layer at outside walls. Also, the solutions do not change with inside mesh resolution and type. However, a mesh with anisotropic layers at outside walls have again the worst accuracy between considered grids.

The results of two-dimensional airfoils, considered in this work, can be easily generalized to three-dimensional wings. For example, a high quality 3D mesh can be created from spanwise extrusion of a high quality 2D mesh. Our future work will expand the results to include meshes around three-dimensional wings with open inlet, deflected trailing edges, and bleed-air spoilers. The experiments of these wings are underway at the USAFA subsonic wind tunnel.

VII. Acknowledgements

Mehdi Ghoreyshi and Jürgen Seidel are supported by USAFA; their financial support is gratefully acknowledged. Acknowledgements are expressed to the Department of Defense High Performance Computing Modernization Program (HPCMP) and ERDC for providing computer time. The authors appreciate the support provided by the Natick Soldier Research Development and Engineering Center (NSRDEC) Airdrop Technology Team and the High Performance Computing Research Center at USAFA.

This material is based in part on research sponsored by the US Air Force Academy under agreement number FA7000-13-2-0009. The U.S. Government is authorized to reproduce and distribute reprints for Governmental purposes notwithstanding any copyright notation thereon. The views and conclusions contained herein are those of the authors and should not be interpreted as necessarily representing the official policies or endorsements, either expressed or implied, of the US Air Force Academy or the U.S. Government.

References

¹Liseikin, V. D., Grid Generation Methods, Springer Science, Second Edition, 2010.

²Anderson, J. D., Modern Compressible Flow: With Historical Perspective, McGraw-Hill Higher Education, Third Edition, 2002.

³McCormick, S. F., Multilevel Adaptive Methods for Partial Differential Equations, Society of Industrial and Applied Mathematics, 1989.

⁴Gu, X., Schock, H. J., Shih, T. I.-P., Hernandez, E. C., Chu, D., Keller, P. S., and Sun, R. L., "Grid-Quality Measures for Structured and Unstructured Meshes," AIAA Paper 2001-665, January 2001.

⁵Thompson, J. F., Soni, B. K., and Weatherill, N. P., Handbook of Grid Generation, CRC Press, 1999.

⁶Knupp, P. and Steinberg, S., Fundamentals of Grid Generation, CRC Press, 1994.

⁷Henne, P. A., Applied Computational Aerodynamics, American Institute of Aeronautics and Astronautics, 1990.

⁸Baker, T. J., "Three Decades of Meshing; A Retrospective View," AIAA Paper 2003-3563, June 2003.

⁹Sarrate, J. and Staten, M., Proceedings of the 22nd International Meshing Roundtable, Springer International Publishing, 2014.

¹⁰Cheng, S.-W., Dey, T. K., and Shewchuk, J. R., Delaunay Mesh Generation, CRC Press, 2013.

¹¹Leondes, C. T., Structural Dynamic Systems Comutational Techniques and Optimization, Volume 1, Overseas Publishers Association, 1998.

¹²Michal, T. and Cary, A., "Unstructured Grid Extrusion for Viscous Flow Simulations," AIAA Paper 2001-0444, January 2001.

¹³Chalasani, S. and Thompson, D., "Quality Improvements in Extruded Meshes Using Topologically Adaptive Generalized Elements," International Journal for Numerical Methods in Engineering, Vol. 60, 2004, pp. 11391159.

¹⁴ITO, Y. and Nakahashi, K., "Unstructured Hybrid Grid Generation Based on Isotropic Tetrahedral Grids," AIAA Paper 2002-0861, January 2002.

¹⁵Ghoryeshi, M., Jirasek, A., and Cummings, R. M., "Computational Investigation into the Use of Response Functions for Aerodynamic Loads Modeling," AIAA Journal, Vol. 50, No. 6, 2012, pp. 1314–1327.

¹⁶Ghoryeshi, M., Post, M. L., and Cummings, R. M., "CFD Calculation of Aerodynamic Indicial Functions for a Generic Fighter Configuration," *ITEA journal of Test and Evaluation*, Vol. 33, No. 6, 2012, pp. 348–364.

¹⁷Ghoreyshi, M., Cummings, R. M., DaRonch, A., and Badcock, K. J., "Transonic Aerodynamic Loads Modeling of X-31 Aircraft Pitching Motions," AIAA Journal, Vol. 51, 2013, pp. 2447–2464.

¹⁸Ghoreyshi, M. and Cummings, R. M., "Unsteady Aerodynamics Modeling for Aircraft Maneuvers: a New Approach Using Time-Dependent Surrogate Modeling," *Journal of Aerospace Science and Technology*, Vol. 39, 2014, pp. 222–242.

¹⁹Tyssel, L., "Hybrid Grid Generation for Complex 3D Geometries," Proceedings of the 7th International Conference on Numerical Grid Generation in Computational Field Simulation, 2000, pp. 337–346.

²⁰Tyssel, L., "The TRITET Grid Generation System," International Society of Grid Generation (ISGG)," Proceedings of the 10the International Conference on Numerical Grid Generation in Computational Field Simulations, 2000.

²¹Ghoreyshi, M., Seidel, J., Bergeron, K., Jirasek, A., Lofthouse, A. J., and Cummings, R. M., "Prediction of Aerodynamic Characteristics of a Ram-Air Parachute," AIAA Paper 2014-2831, June 2014.

²²Bergeron, K., Jurgen, S., Ghoreyshi, M., Jirasek, A., Lofthouse, A. J., and Cummings, R. M., "Numerical Study of Ram Air Airfoils and Upper Surface Bleed-Air Control," AIAA Paper 2014-2832, June 2014.

²³Strang, W. Z., Tomaro, R. F., and Grismer, M. J., "The Defining Methods of Cobalt: A Parallel, Implicit, Unstructured Euler/Navier-Stokes Flow Solver," AIAA Paper 1999–0786, 1999.

²⁴Gottlieb, J. J. and Groth, C. P. T., "Assessment of Riemann Solvers For Unsteady One-dimensional Inviscid Flows of Perfect Gasses," *Journal of Computational Physics*, Vol. 78, No. 2, 1988, pp. 437–458.

²⁵Tomaro, R. F., Strang, W. Z., and Sankar, L. N., "An Implicit Algorithm For Solving Time Dependent Flows on Unstructured Grids," AIAA Paper 1997–0333, 1997.

²⁶Tomaro, R. F., Strang, W. Z., and Wurtzler, K. E., "Can Legacy Codes Scale on Tens of Thousands of PEs or Do We Need to Reinvent the Wheel?" 2012 High Performance Computing Modernization Program Contributions to DoD Mission Success, pp. 231-236, September 2012.

²⁷Spalart, P. R. and Allmaras, S. R., "A One Equation Turbulence Model for Aerodynamic Flows," AIAA Paper 1992–0439, January 1992.

²⁸Spalart, P. R. and Shur, M. L., "On the Sensitization of Turbulence Models to Rotation and Curvature," Aerospace

Science Technology, Vol. 1, 1997, pp. 297302.

²⁹Spalart, P. R., Jou, W.-H., Strelets, M., and Allmaras, S. R., "Comments on the Feasibility of LES for Wings, and on a Hybrid RANS/LES Approach," In Proceedings, 1st AFSOR International Conference on DNS/LES, Greyden Press, Columbus, OH, 1997, pp. 137147.

 $^{30}\mathrm{Solutions},$ C., "Cobalt User's Manula," February 11, Cobalt Version 6.0, 2013.

- ³¹Dannenhoffer, J. F., "Correlation of Grid Quality Metrics and Solution Accuracy for Supersonic Flows," AIAA Paper 2012-0610, January 2012.
- ³²McDaniel, D. R., Deformation of Viscous CFD Meshes for Aeroelastic and S&C Applications, Phd dissertation, Department of Mechanical and Aerospace Engineering, University of Colorado at Colorado Springs, November 2010.

³³Rumsey, C. L. and Slotnick, J. P., "Overview and Summary of the Second AIAA High Lift Prediction Workshop," AIAA

Paper 2014-0747, January 2014.

- ³⁴Mavriplis, D. J., Vassberg, J. C., Tinoco, E. N., Mani, M., Brodersen, O. P., Eisfeld, B., Wahls, R. A., Morrison, J. H., Zickuhr, T., Levy, D., and Murayama, M., "Grid Quality and Resolution Issues from the Drag Prediction Workshop Series," AIAA Paper 2008-0930, January 2008.
- ³⁵Maddock, I., Harby, A., Kemp, P., and Wood, P. J., Ecohydraulics: An Integrated Approach, John Wiley & Sons, 2013.
 ³⁶Alter, S. J., "A Structured-Grid Quality Measure for Simulated Hypersonic Flows," AIAA Paper 2004-0612, January 2004.
- ³⁷Morton, S. A., McDaniel, D. R., Sears, D. R., Tillman, B., and Tuckey, T. R., "Kestrel: A Fixed Wing Virtual Aircraft Product of the CREATE Program," AIAA Paper 2009-0338, January 2009.
- ³⁸Benney, R. J., Krainski, W. J., Onckelinx, C. P., Delwarde, C. C., Mueller, L., and Vallance, M., "NATO Precision Airdrop Initiatives and Modeling and Simulation Needs," RTO-MP-AVT-133 Technical Report, October 2006.
- ³⁹Bergeron, K., Ward, M., and Costello, M., "Aerodynamic Effects of Parafoil Upper Surface Bleed Air Actuation," AIAA

Paper 2012–4737, August 2012.

⁴⁰Lingard, J. S., "Precision Aerial Delivery Seminar Ram-Air Parachute Design," 13th AIAA Aerodynamic Decelerator Systems Technology Conference, Clearwater Beach, May 1995.

Table 1. Closed grid details. Δ_{s1} and N_s denote the initial spacing and the number of layers of constant spacing normal to all viscous walls, respectively. Growth rate in the viscous layer is shown by GR. Finally, c is the airfoil chord and l denotes the farfield length away from the airfoil.

Grid	Type	Method	Δ_{s1}	N_s	GR	l/c	# Cells
CG1	STR	Normal extrusion, elliptic	1e-5 m	7	1.1	100	341,850
CG2	STR	Multi-block, algebraic	1e-5 m	7	1.1	100	324,570
CG10	STR	Normal extrusion, elliptic	4e-5 m	-	1.1	25	131-141 Straff Section 751
CG11	STR	Normal extrusion, elliptic	4e-5 m	-	1.1	50	115,320 120,900
CG12	STR	Normal extrusion, elliptic	4e-5 m	-	1.1	75	124,620
CG13	STR	Normal extrusion, elliptic	4e-5 m	-	1.1	100	128,340
CG20	STR	Normal extrusion, elliptic	2e-5 m	2	1.1	50	127,410
CG21	STR	Normal extrusion, elliptic	1e-5 m	2	1.1	50	133,920
CG30	UNSTR	Delaunay, anisotropic viscous layers	4e-5 m	2	1.1	50	101,894
CG31	UNSTR	Delaunay, anisotropic viscous layers	2e-5 m	=	1.1	50	114,970
CG32	UNSTR	Delaunay, anisotropic viscous layers	1e-5 m	_	1.1	50	128.564
CG40	HYBRID	Delaunay, 25 prismatic viscous layers	1e-5 m	-	1.1	50	55,324
CG41	HYBRID	Delaunay, 50 prismatic viscous layers	1e-5 m	-	1.1	50	77,754
CG42	HYBRID	Delaunay, 75 prismatic viscous layers	1e-5 m	_	1.1	50	100.842

Table 2. Closed grid solution details.

					err %	
Grid	Y^+	Quality	C_L	C_D	L/D	C_{Lmax}
CG1	0.2663	98.62	0.1484	0.1276	0.2209	0.1183
CG2	0.2339	98.81	1.1504	2.0752	5.6311	-1.7914
CG10	1.074	99.14	1.8921	2.9175	8.1312	-1.7116
CG11	1.074	99.15	1.7397	2.3424	5.0274	-1.6729
CG12	1.074	99.16	1.7155	2.2623	4.4330	-1.6793
CG13	1.074	99.19	1.7045	2.2196	4.0466	-1.6824
CG20	0.5336	99.12	1.0534	1.1167	2.7766	-1.0524 -1.0541
CG21	0.2663	98.99	0.8772	0.7775	2.2576	-0.8549
CG30	0.7260	99.83	0.3247	1.8036	4.3489	0.3532
CG31	0.3642	99.71	4.3107	5.8003	3.6808	
CG32	0.1796	99.55	3.5703	4.5855		1.4514
CG40	0.2663	98.55	5.2646	7.2829	2.9438	1.6056
CG41	0.2663	98.97	1.0484		7.8631	-6.2807
CG42	0.2663	98.94	0.5906	0.5219 0.8316	1.6164 2.1128	-0.8507 -0.5507

Table 3. Open grid details. l/c=100 and GR = 1.1 for all grids.

Grid	Outside mesh	Inside mesh	Δ_{s1}	N_s	# Cavity cells	# Total cells
OG1	STR, elliptic	STR, uniform	4e-5 m	25	278,620	421,840
OG2	STR, elliptic	STR, uniform	4e-5 m	5	278,620	403,240
OG3	STR, elliptic	STR, uniform	4e-5 m	0	278,620	399,520
OG4	STR, elliptic	STR, uniform	2e-5 m	5	278,620	407,500
OG5	STR, elliptic	STR, uniform	1e-5 m	5	278,620	416,260
OG10	STR, elliptic	STR, uniform	1e-5 m	5	120,384	285,028
OG11	STR, elliptic	STR, uniform	1e-5 m	5	56,000	194,188
OG12	STR, elliptic	STR, uniform	1e-5 m	5	22,000	148,262
OG20	STR, elliptic	UNSTR, Delaunay	1e-5 m	5	9,812	137,058
OG21	STR, elliptic	UNSTR, Delaunay	1e-5 m	5	5,209	136,520
OG22	isotropic and anisotropic	UNSTR, Delaunay	1e-5 m	-	5,275	118,202
OG40	HYBRID, 75 prism layers	UNSTR., Delaunay	1c-5 m	-	5,275	98,620

Table 4. Open grid solution details.

Grid	Y+	Quality	err %			
			C_L	C_D	L/D	C_{Lmax}
OG1	0.9490	99.66	0.7146	1.1728	1.7029	-0.4407
OG2	0.9495	99.69	0.9527	1.4604	1.9284	-0.5427
OG3	0.9501	99.70	1.2356	1.6935	2.3153	-0.7218
OG4	0.4721	99.66	0.4549	0.5146	0.5746	-0.1788
OG5	0.2360	99.59	0.4232	0.3767	0.4536	-0.1312
OG10	0.2360	99.26	0.4269	0.3506	0.4322	-0.0934
OG11	0.2359	98.85	0.4430	0.4462	0.5599	-0.1770
OG11 OG12	0.2357	98.86	0.5402	0.4694	0.8619	-0.4866
OG20	0.2360	98.92	0.4994	1.5627	2.6723	-0.1016
OG20 OG21	0.2360	98.91	0.4323	1.8874	3.8378	-0.1263
OG21	0.1599	99.35	3.4452	1.1538	2.6855	1.7791
OG40	0.2364	98.90	1.0078	1.5233	3.2509	0.3833

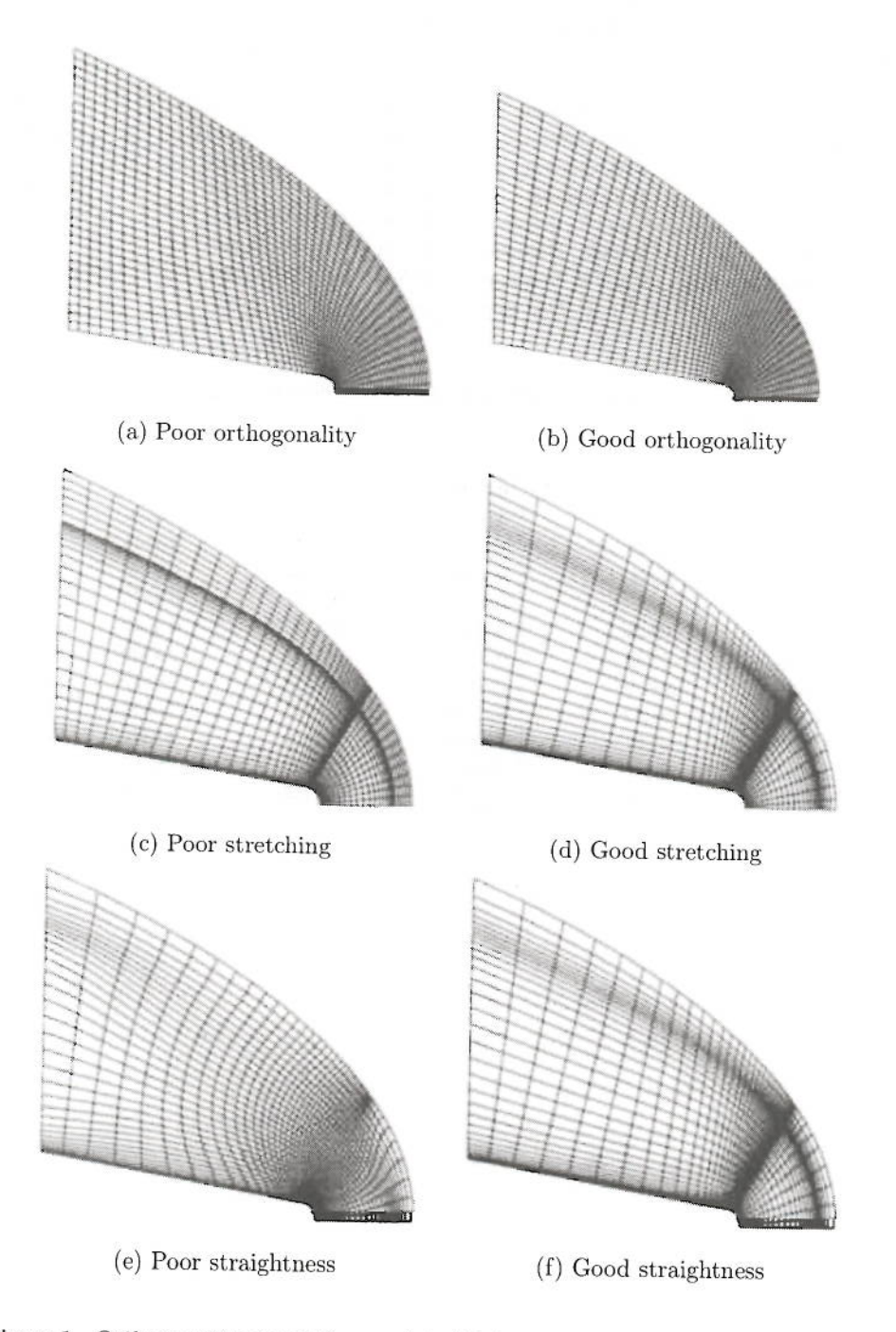


Figure 1. Orthogonality, stretching, and straightness examples for structured grids. 36

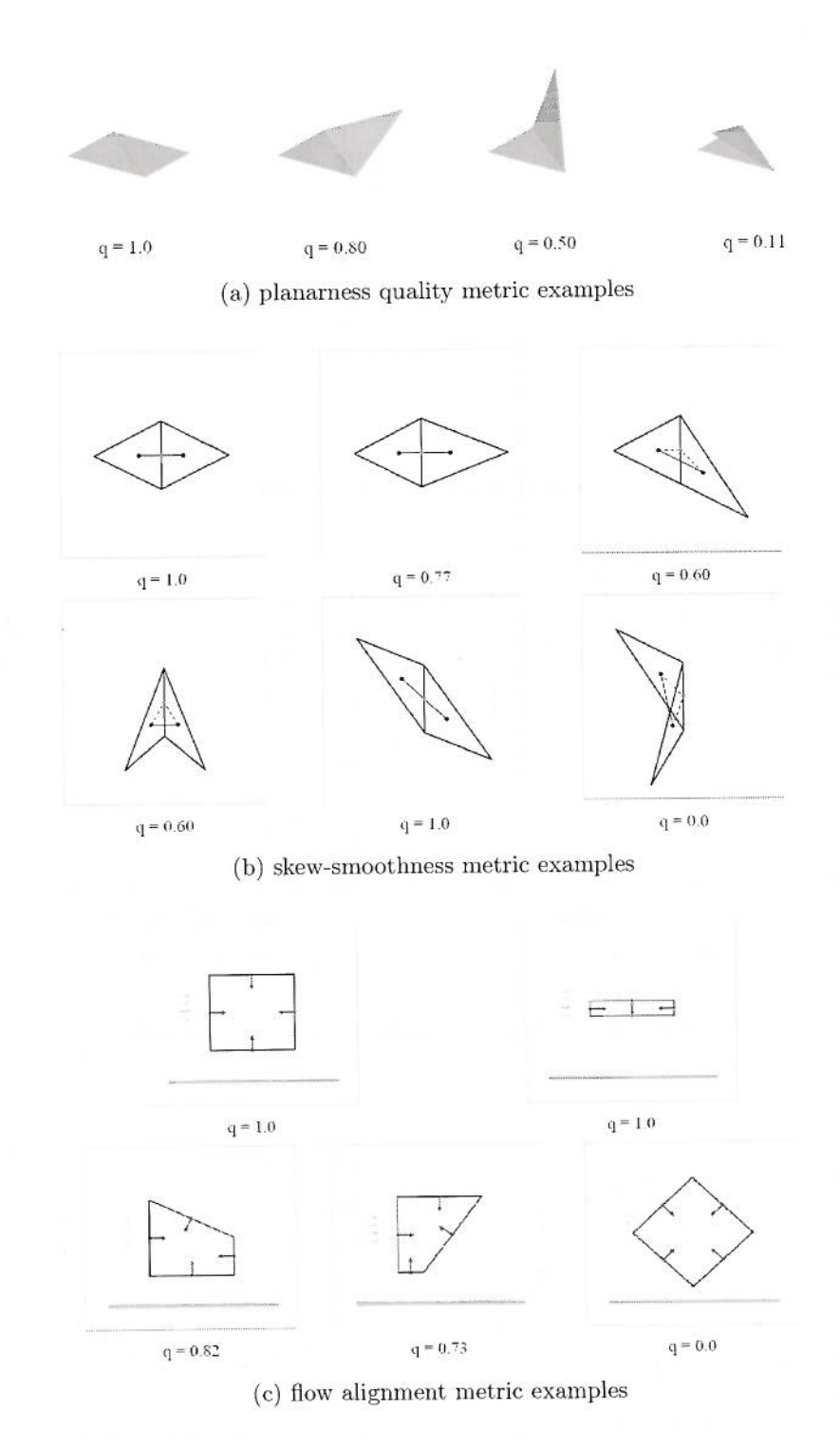


Figure 2. Planarness, skew-smoothness, and flow alignment metric examples from Ref. 32.

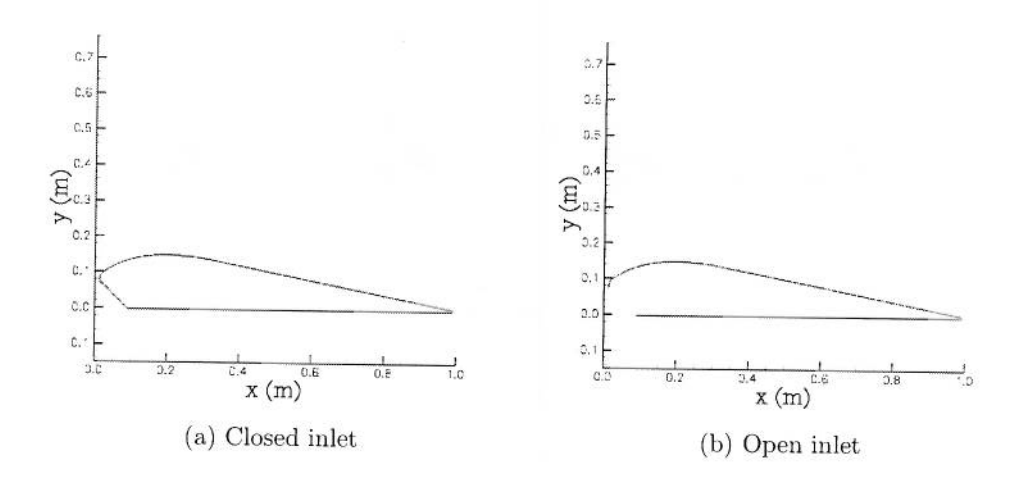


Figure 3. Airfoil geometries for the parachute cases

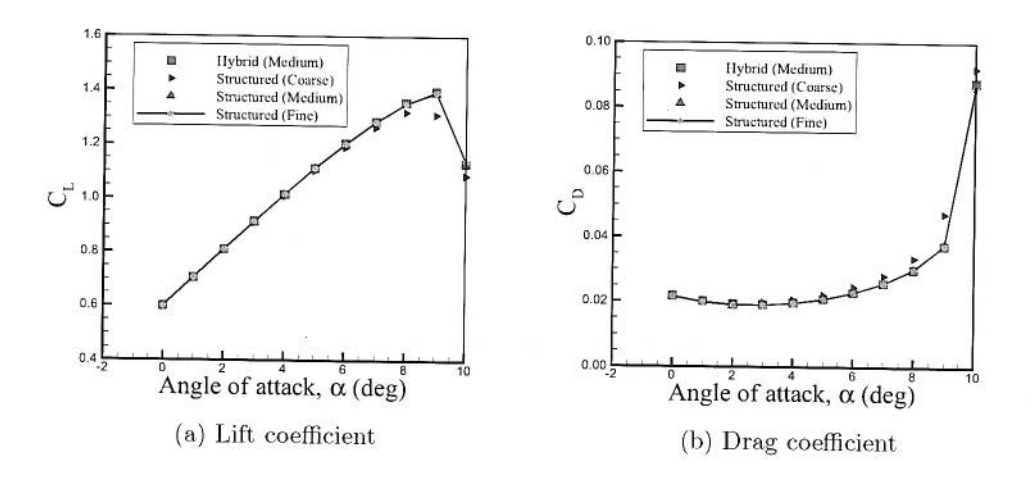


Figure 4. Mesh-independent study of the closed-inlet airfoil.

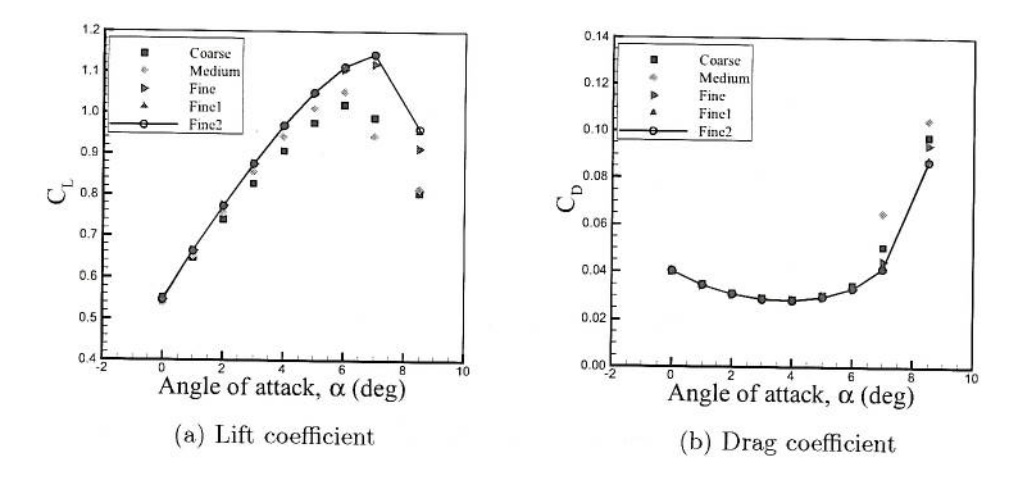
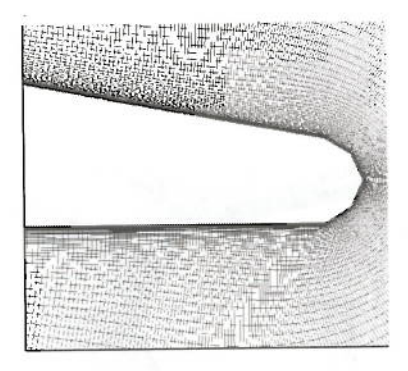
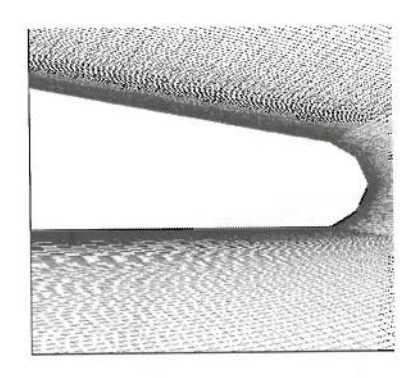


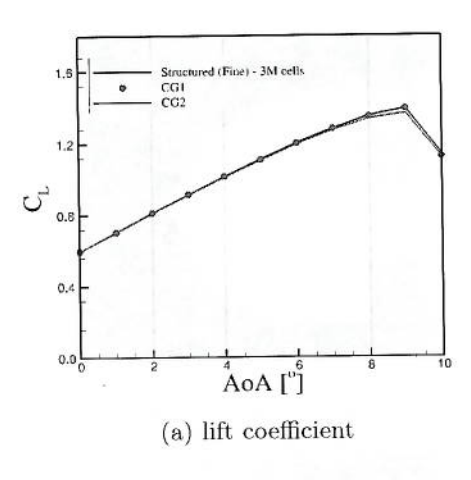
Figure 5. Mesh-independent study of the open-inlet airfoil.





- (a) CG1, structured, elliptic mesh
- (b) CG2, multi-block structured mesh

Figure 6. CG1 and CG2 grids overview.



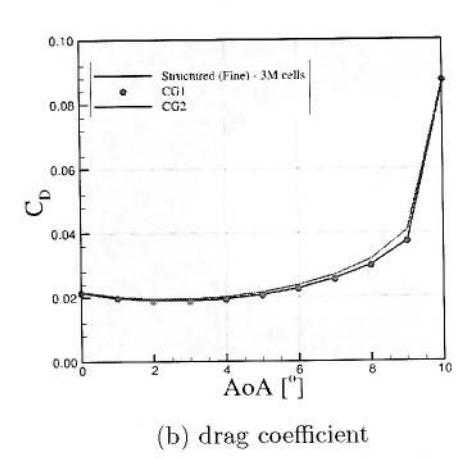


Figure 7. Lift and drag coefficients of CG1 and CG2 grids. The structured fine grid is from Ref. 21.

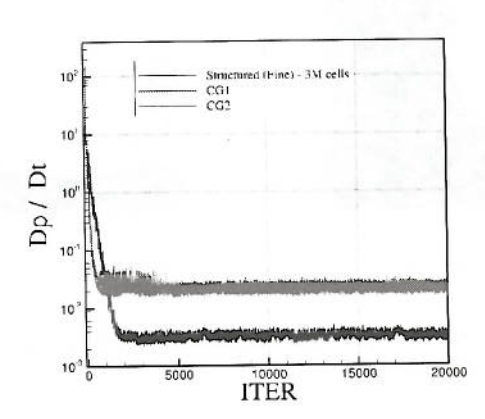


Figure 8. Density residual convergence $(D\rho/Dt)$ of CG1 and CG2 grids, where ρ and t denote density and time, respectively. The structured fine grid is from Ref. 21.

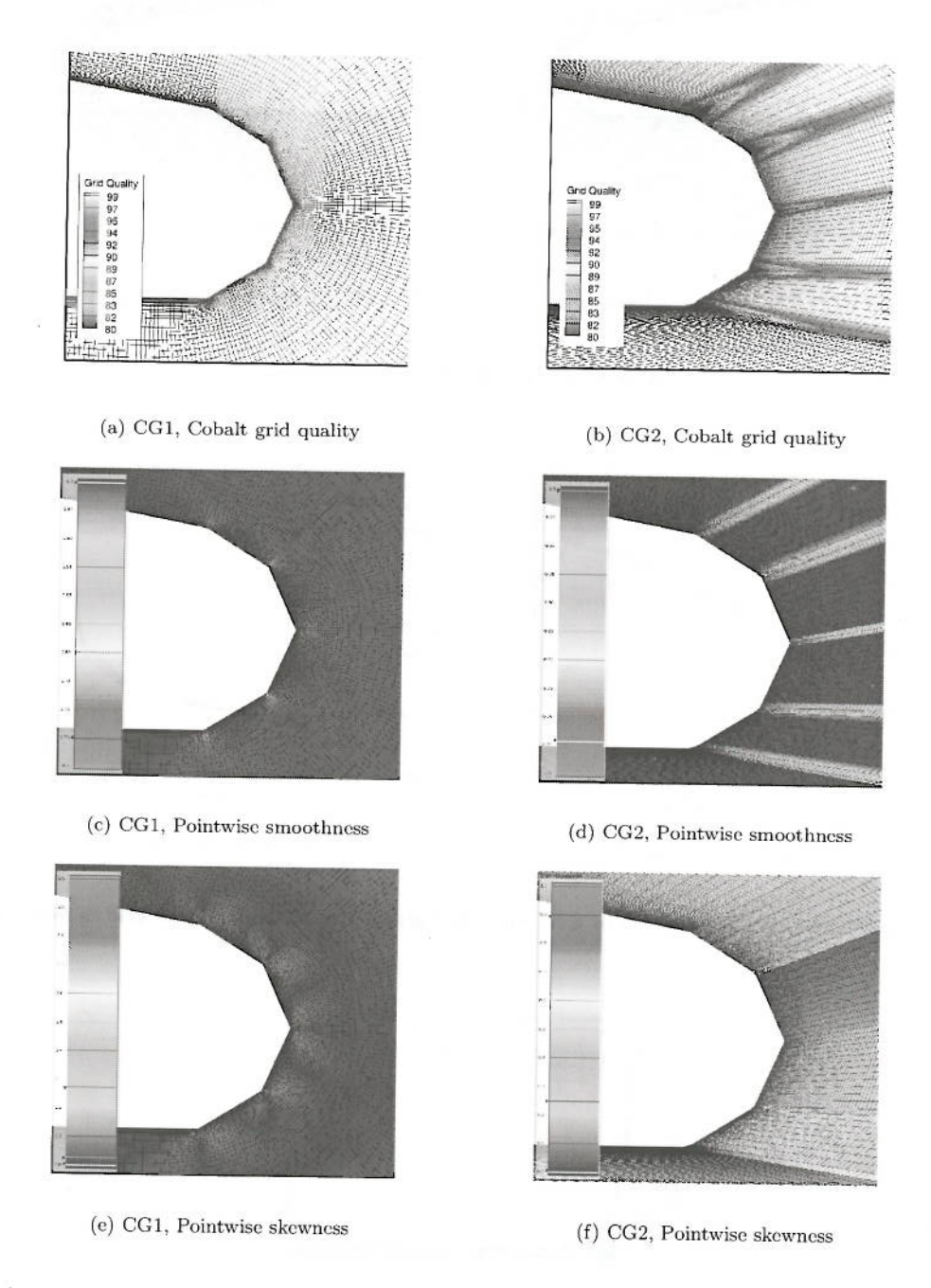


Figure 9. Cobalt grid quality relationship with mesh geometry- Mesh is around trailing edge. In (a) and (b) the white colored cells have the highest quality.

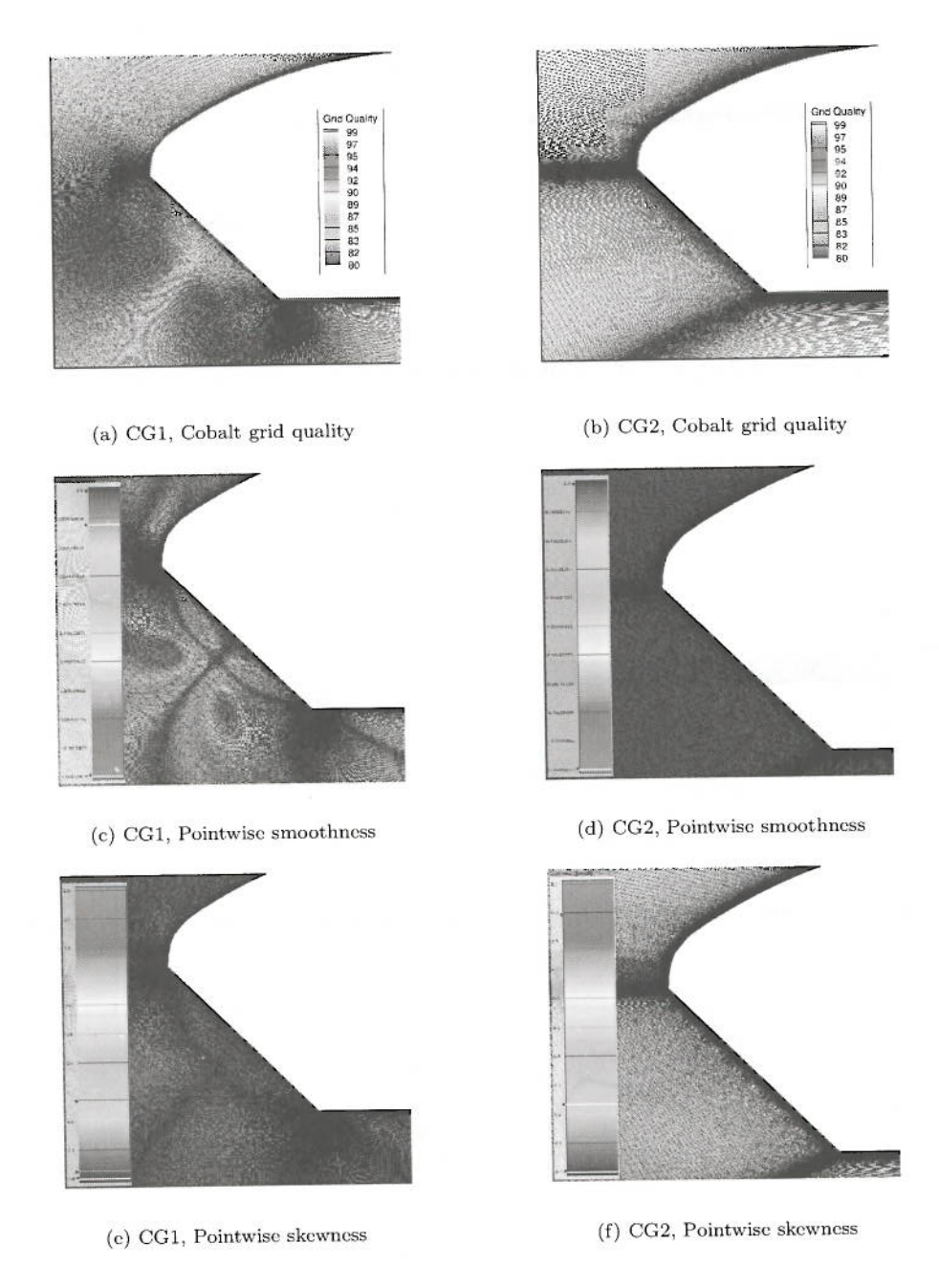


Figure 10. Cobalt grid quality relationship with mesh geometry- Mesh is around leading edge. In (a) and (b) the white colored cells have the highest quality.

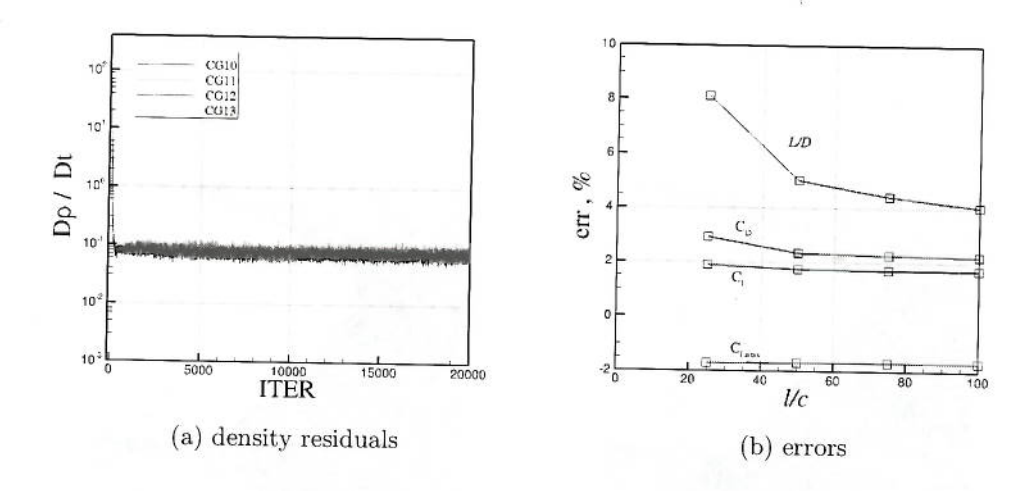


Figure 11. Effects of farfield length (l) on the solution convergence and errors.

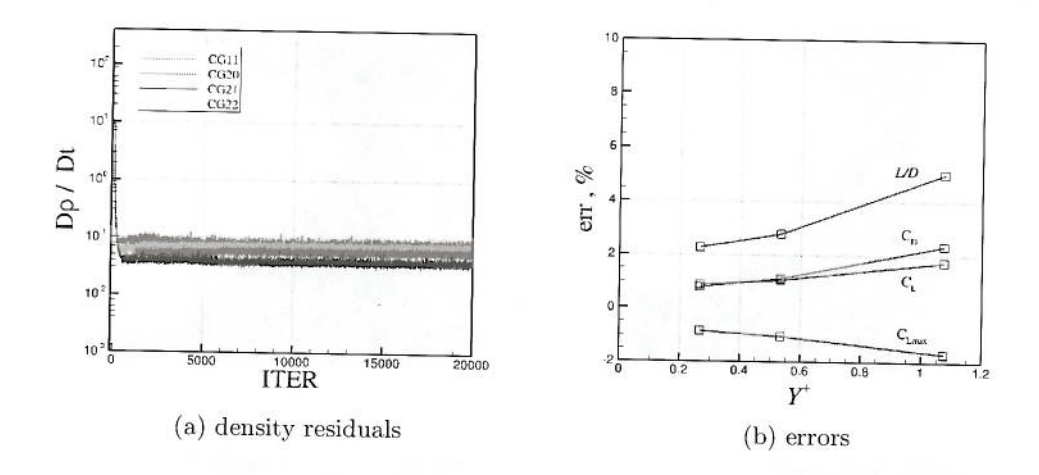


Figure 12. Effects of initial grid spacing (Δ_{s1}) on the solution convergence and errors of structured grids.

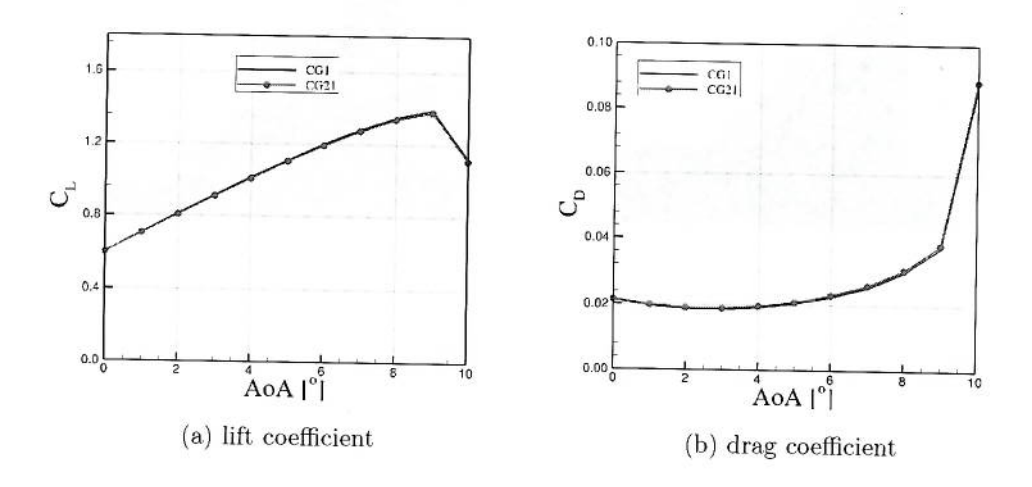


Figure 13. Lift and drag coefficients of CG1 (341,850 cells) and CG21 (133,920 cells) grids.

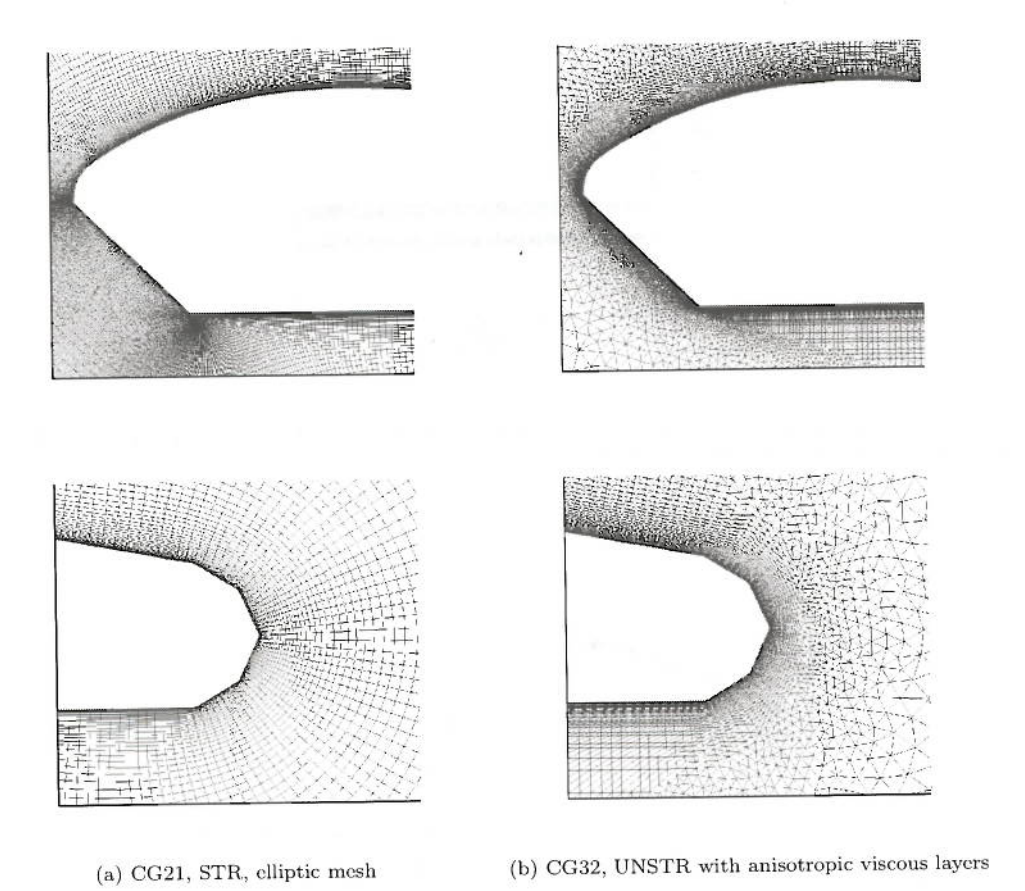


Figure 14. CG21 and CG32 grids overview.

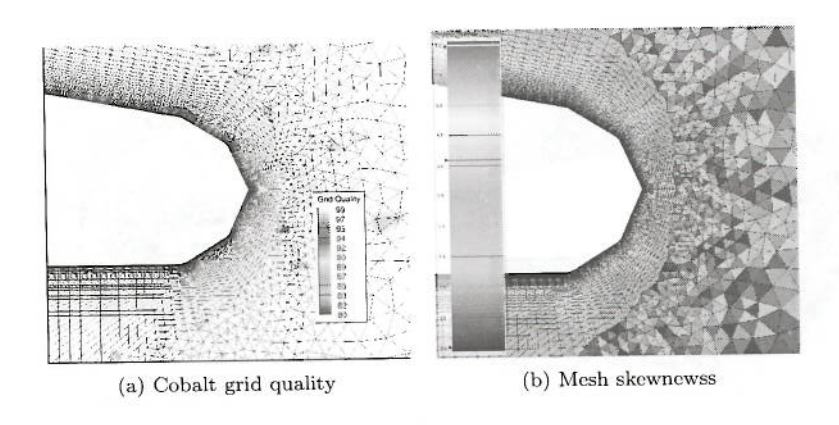


Figure 15. Cobalt cell quality versus Pointwise cell skewness.

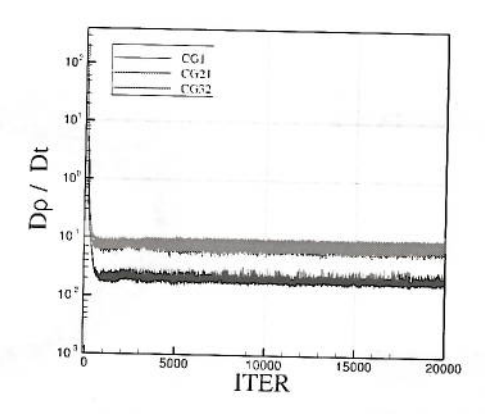


Figure 16. Density residual convergence $(D\rho/Dt)$ of CG1 (STR with 341,850 cells), CG21 (STR with 133,920 cells), and CG32 (USTR with 128,564 cells).

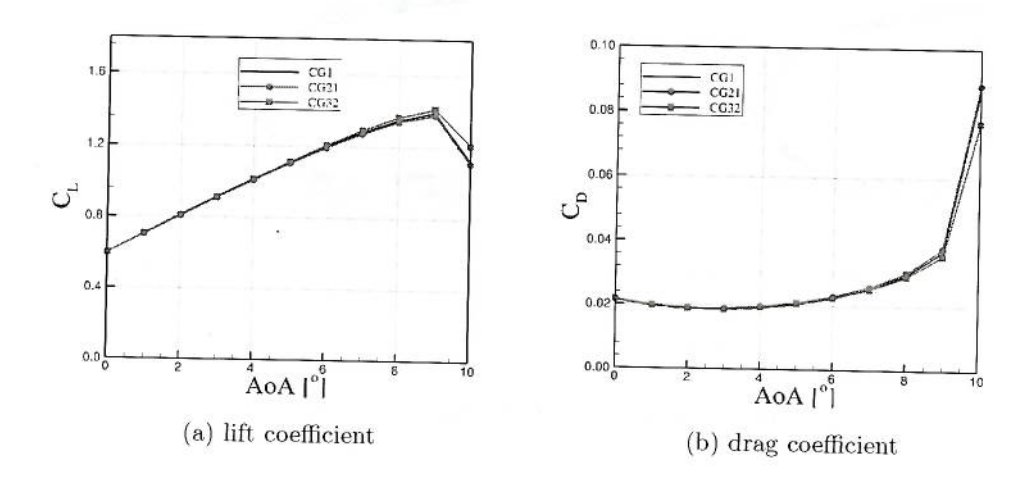


Figure 17. Lift and drag coefficients of CG1, CG21, and CG32.

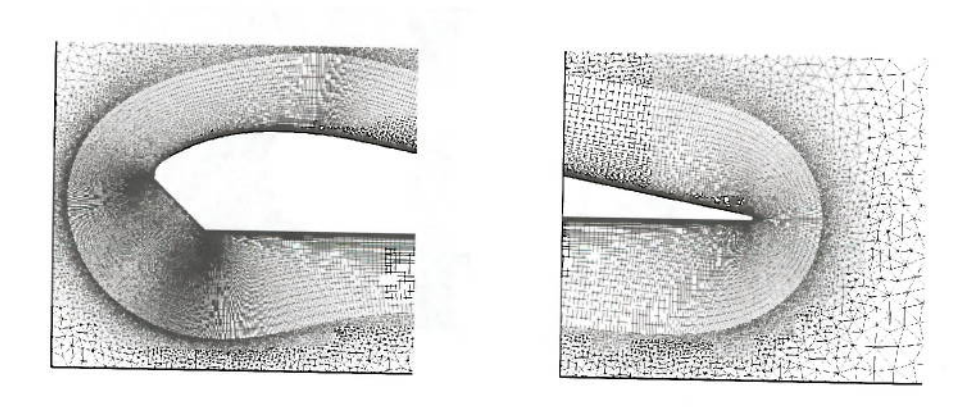


Figure 18. Hybrid mesh of CG42 with 75 prismatic layers near the wall.

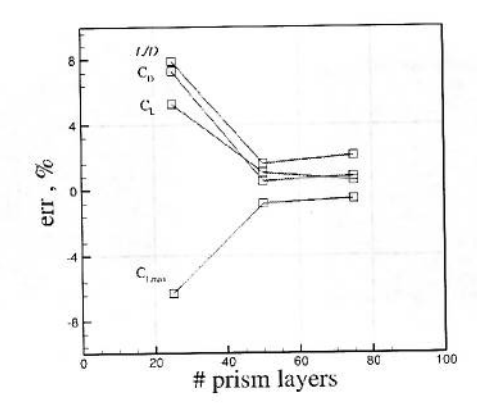


Figure 19. Solution errors against number of prism layers in the hybrid grids.

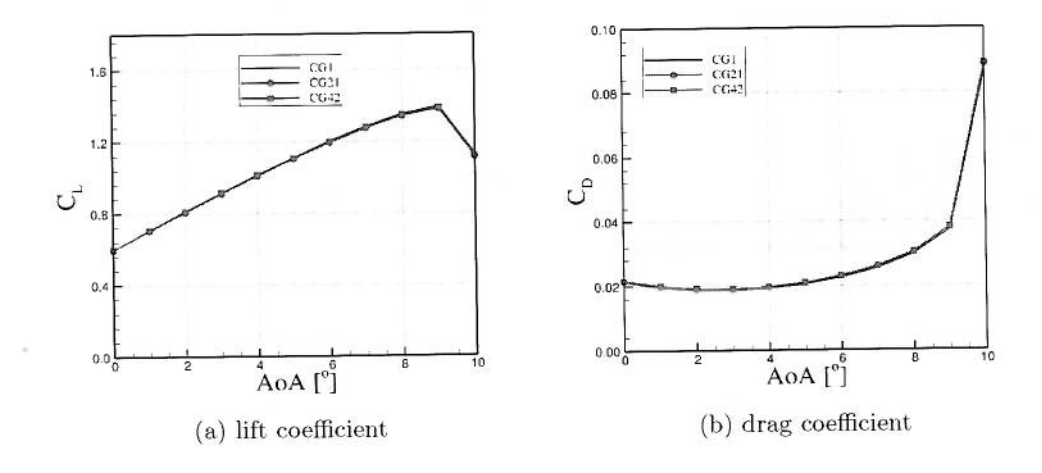
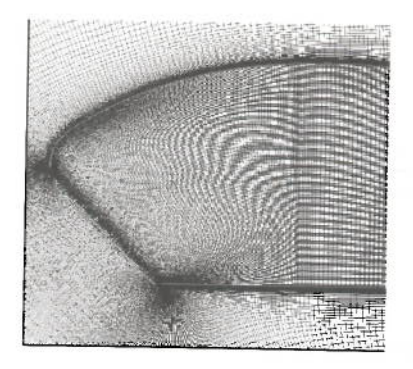


Figure 20. Lift and drag coefficients of CG42 mesh.



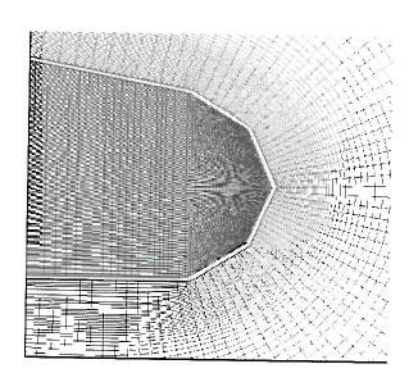
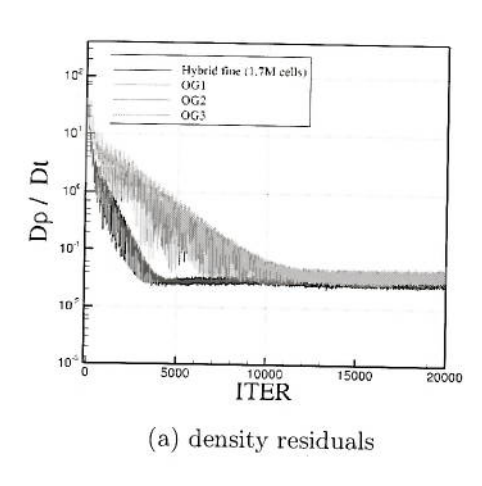


Figure 21. OG1 grid overview.



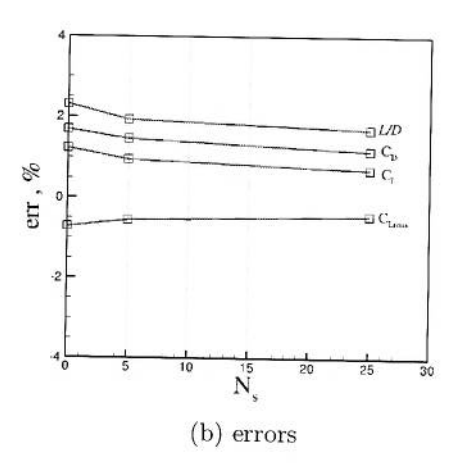
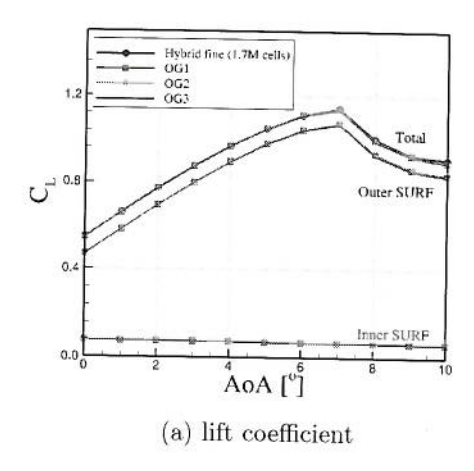
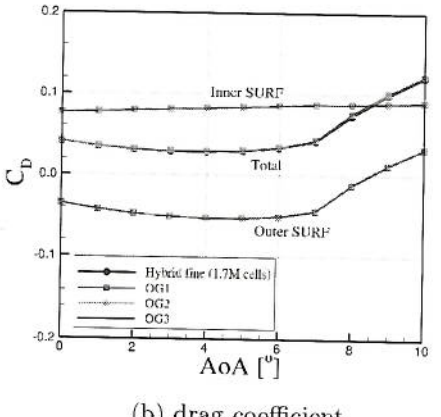


Figure 22. Effects of initial grid spacing (N_s) on the solution convergence and errors of open airfoil grids.





(b) drag coefficient

Figure 23. Lift and drag coefficients of OG1, OG21, and OG32. The coefficients were compared with the hybrid fine grid (1.7M cells) of Ref. 21.

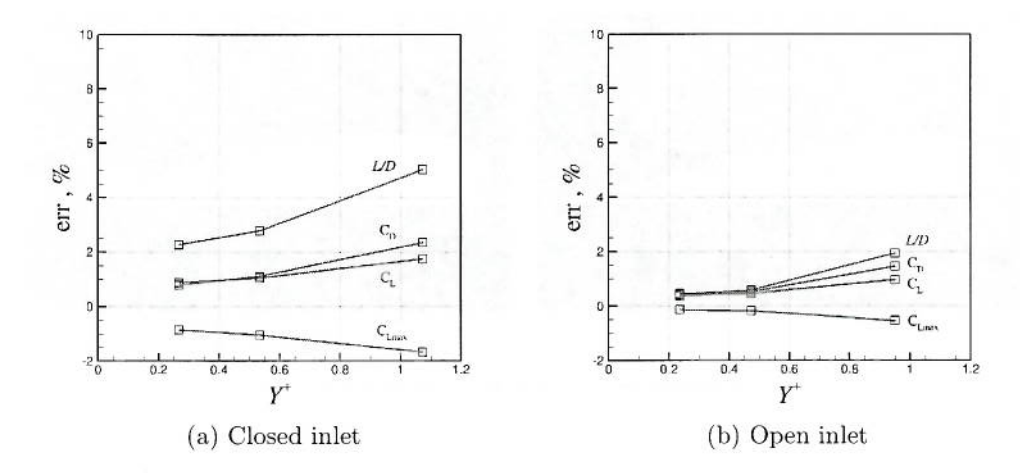


Figure 24. Effects of initial grid spacing (Δ_{s1}) on the solution errors of closed- and open-inlet grids.

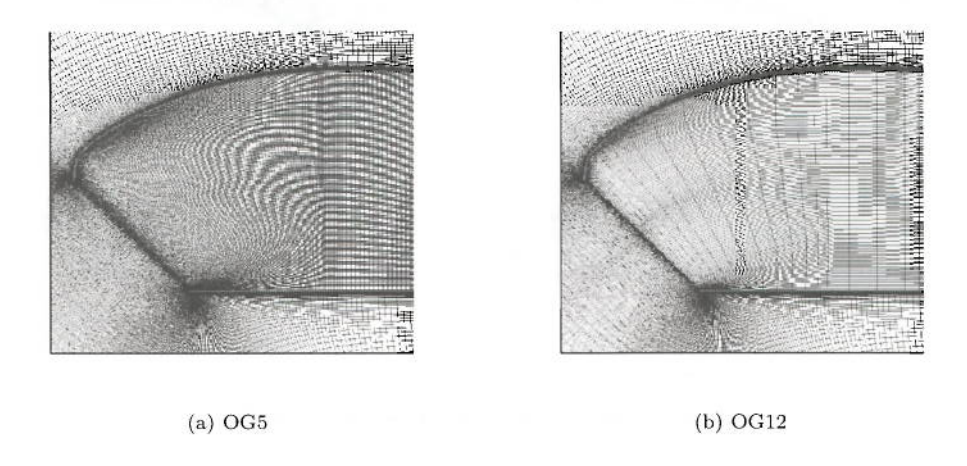


Figure 25. OG12 (with 148,262 cells) grid overview compared to OG5 mesh (with 410,260 cells).

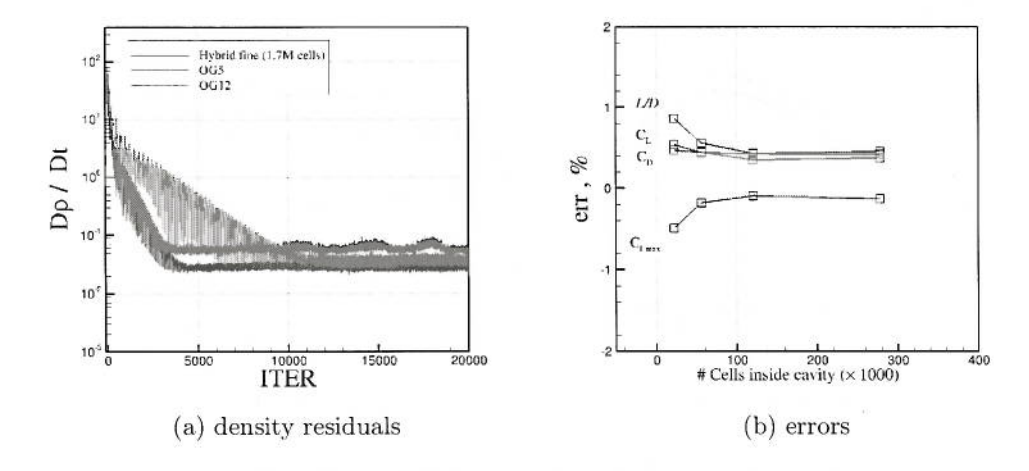


Figure 26. Effects of cavity cell numbers on the solution convergence and errors of open airfoil grids.

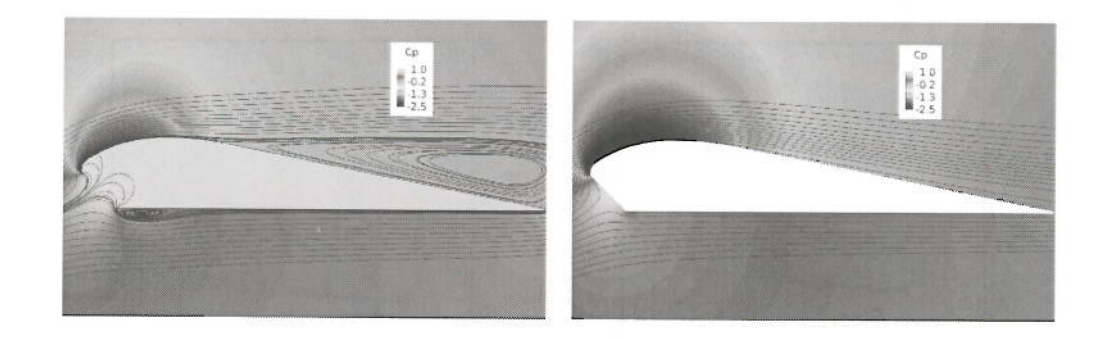


Figure 27. Pressure plots of open- and closed-inlet at $\alpha=8.5^{\circ}$.

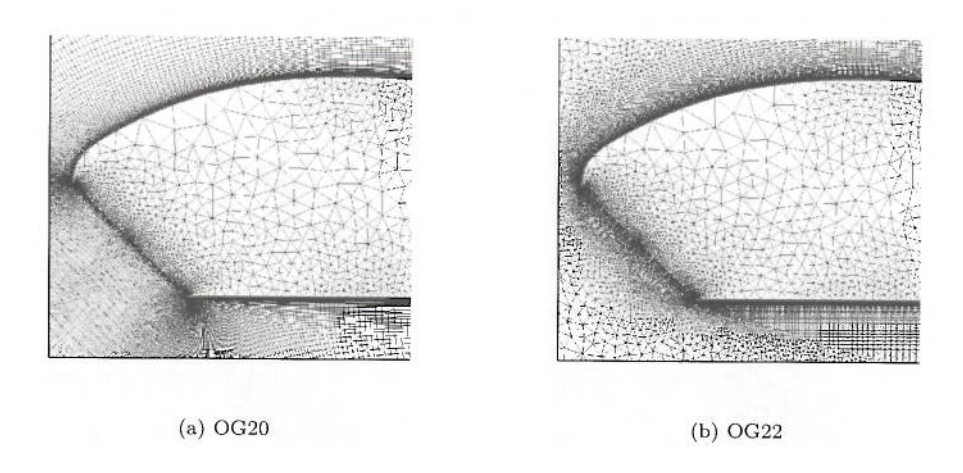


Figure 28. Overview of OG20 and OG22 meshes.

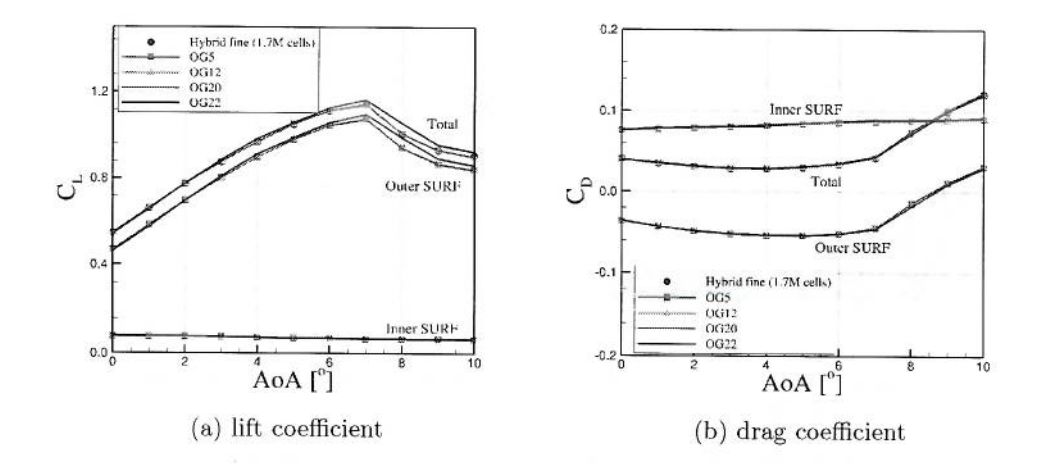
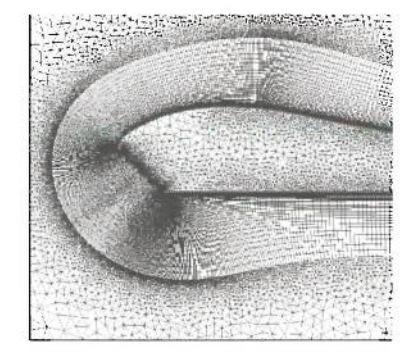


Figure 29. Lift and drag coefficients of OG5, OG12, and OG20.



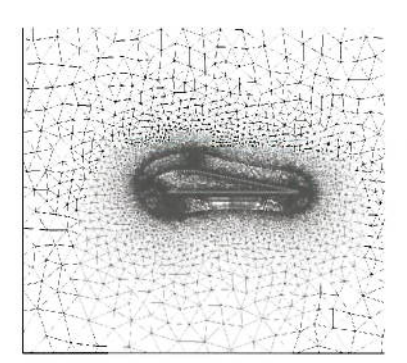
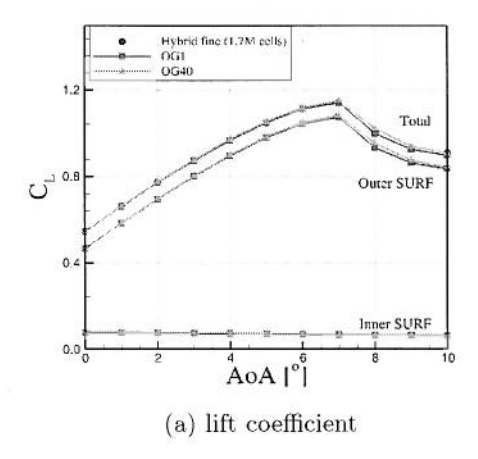


Figure 30. OG40 mesh overview.



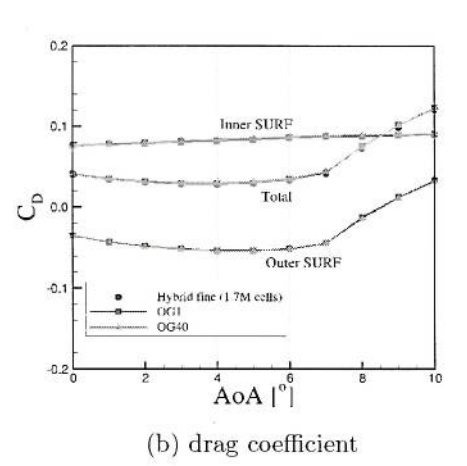


Figure 31. Lift and drag coefficients predicted by the hybrid OG40 mesh.

Vortical Flow Prediction of the AVT-183 Diamond Wing

Mehdi Ghoreyshi^{*}, Krzysztof Ryszka[†] Russell M. Cummings[‡] and Andrew J. Lofthouse[§]

High Performance Computing Research Center, U.S. Air Force Academy USAF Academy, Colorado 80840-6400

The objective of this paper is to assess the potential and limitations of current practice in computational fluid dynamic modeling for predicting vortical flowfields over a generic 53-degree swept diamond wing with blunt tips. This wing was designed under STO AVT Task Group 183 and is based on the SACCON UCAV geometry, which is a lambda wing with complex span-wise distributions of thickness and leading edge radius and with a linear twist onboard of the first trailing edge break. The SACCON wing trailing-edge was swept forward by 26.5-degrees to form a diamond-shaped planform. This new wing also has a constant airfoil section of NACA 64A-006 with a leading edge radius of 0.264 in percent chord and has no twist angle. CFD simulations were performed for an angle of attack sweep at Mach number of 0.15 and Reynolds number of 2.7×10^6 based on the mean aerodynamic chord to match experiments. CFD simulations were run with different turbulence models, that close the Reynolds averaged Navier-Stokes equations, and with a limited assessment of delayed detached eddy simulations. The wind tunnel experiments of the diamond wing were carried out in the Institute of Aerodynamics and Fluid Mechanics of Technische Universität München, Germany and include aerodynamic lift, drag, and pitch moment measurements as well as span-wise pressure distributions at different chord-wise locations. This data set is used to validate CFD results. The results presented demonstrate that the pitch moments predicted by the SARC turbulence model provide a better match to experimental results than the SA model at moderate angles of attack. However, at high angles of attack, all pitch moment predictions are off. The flow visualization results show that a leading-edge vortex is formed above the upper surface of the wing at an angle of attack about eight degrees. This vortex will become larger and stronger as the angle of attack is increased. With increasing angle of attack, the vortex starting point moves upstream and the vortex core moves inboard towards the wing root. The results also show that for the range of angles of attack considered in this work, the flow over the diamond wing is steady, because the vortices are attached and stationary at each angle of attack.

Distribution A. Approved for Public Release. Distribution unlimited.

^{*}Senior Aerospace Engineer, AIAA Senior Member

 $^{^{\}dagger}$ Cadet of Aeronautical Engineering

[‡]Professor of Aeronautics, AIAA Associate Fellow

[§]Director, AIAA Senior Member

Nomenclature

C_L	lift coefficient, $L/q_{\infty}S$
C_m	pitch moment coefficient, $\bar{M}/q_{\infty}Sc$
c	mean aerodynamic chord, m
c_r	chord length at wing root, m
L	lift force, N
M	Mach number, V/a
\bar{M}	pitch moment, N-m
q_{∞}	dynamic pressure, Pa, $\rho V^2/2$
Re	Reynolds number, $\rho V c/\mu$
s	half span, m
V = V	time, s
V	freestream velocity, m/s
x, y, z	aircraft position coordinates
Greek	
α	angle of attack, rad
β	side-slip angle, rad
μ	air viscosity

I. Introduction

Today's modern fighter aircraft typically employ a delta wing configuration to reduce the wave drag at supersonic speeds. The aerodynamic performances of these delta wings are vastly different from those known for the high-aspect ratio wings. In the latter case, the lift increases linearly with angle of attack in the attached flow region and then sharply decreases in the post-stall region. The lift of a sharp delta wing has also an initial linear increase, but at an angle of attack of just few degrees there is an additional lift force to the attached flow lift which makes the lift-curve slope nonlinear. This additional lift, often called the vortex lift, is caused by the vortical flows formed above the wing. The flow separation point of a sharp delta wing is fixed at the leading edge. This creates a strong shear layer along the wing edges which will then roll up into a pair of counter-rotating vortices over the upper surface on the two halves of the wing. These vortices are called leading-edge vortices and their structures depend on the wing's sweep angle, leading-edge geometry, wing thickness, and freestream conditions.

For a sharp-edged delta wing, the separation points are fixed at the leading edge for a considerable range of angle of attack. The vortex strengths and vortex lift therefore will increase with the increase in the angle of attack. At higher angles, however, vortices experience an abrupt transformation called the vortex breakdown which is an asymmetric phenomenon. In a vortex breakdown, the axial velocity component suddenly decelerates and the swirl component of the mean velocity decreases due to the vortex core expansion. The asymmetric vortex breakdown conditions result in additional moments in pitch, yaw, and roll with magnitudes as large or even larger than those obtained from traditional control surface deflections. The vortex breakdown may result sudden changes in pitching moment, loss of lift, and buffeting. The stability and control (S&C) and structural analysis of delta wings are therefore highly dependent on the ability to observe and accurately calculate the principle characteristics of vortical flows.

While the vortical flow behavior over slender wings with sharp leading edges has been studied extensively for over last few decades, ^{8,9,10} much less is known about the formation of vortices over wings with lower sweep angles and blunt leading edges. These type of wings are often incorporated in the designs of unmanned combat aircraft vehicles (UCAV). ¹¹ For these wings, the vortex flow structure is very complicated and depends heavily on the leading edge bluntness and the wing sweep angle. For delta wings with blunt tips, the leading edge separation point is also very sensitive to the boundary layer changes. ¹² The blunt tip vortices can also have significant effects on the stability and control characteristics of a maneuvering aircraft at high angles of attack. The objective of this work is to assess the potential and limitations of current practice in computational fluid dynamics (CFD) modeling for predicting vortical flowfields over a generic

53-degree swept diamond wing with blunt tips.

The diamond wing considered in this paper was designed under STO AVT Task Group 183. The wing planform is based on the SACCON UCAV geometry. The SACCON wing trailing-edge was swept forward by 26.5-degrees to form a diamond-shaped planform. The new wing has a constant airfoil section of NACA 64A-006 with a leading edge radius of 0.264 in percent chord. The wind tunnel experiments of the diamond wing were carried out in the Institute of Aerodynamics and Fluid Mechanics of Technische Universität München, Germany and include aerodynamic lift, drag, and pitch moment measurements as well as span-wise pressure distributions at different chord-wise locations. This data set is used to validate CFD results.

This work is organized into four major categories. First a survey of the literature and theories pertaining to the delta wing vortical flows is provided. The flow solver is then briefly described. Next, the test case is presented and the experimental setup is detailed. Finally, the simulation results will be discussed.

II. Vortical Flows

The vortical flow behavior over delta wings is extremely complex and differs substantially from sharp to blunt tips and from nonslender to slender wings. Over the past few decades, most research was done on the vortices over slender sharp-edged delta wings.¹³ Some early works in this field were reviewed by Sun¹⁴ and most recently by Mitchell et al.⁴ In one of the earliest studies, for example, Jensen (1948)¹⁵ studied the low-speed flowfields and the lift and moment characteristics of a sweptback wing and a delta wing, both with a 65° sweptback leading edge and a double wedge symmetrical airfoil section. His results showed that two strong vortices are formed over the upper surfaces of both wings for angles of attack as low as 10°. A sketch of these vortices is shown in Figure 1 for the delta wing case. Jensen's work also showed that the lift curve slope increases for angles of attack above ten degrees.

It is well known that a sharp leading edge causes the boundary layer to separate at the leading edge resulting a free shear layer. For a slender wing, the separated shear layers roll up into a pair of counterrotating vortices over the upper surface on the two halves of the wing. The shear layer may exhibit instabilities that increase the vortical substructures and, therefore, the primary vortex increases in both size and strength as it extends downstream. Ornberg¹⁶ in 1954 showed that these leading edge vortices are stationary and form a low pressure region over the upper surface that will increase the lift. Notice that this additional lift comes at the expense of a drag penalty due to loss of leading-edge suction.¹⁷ The leading edge vortices allow the onset of stall to be delayed to higher angles as well. For steady and inviscid flow, the vortex lift can be approximated to some extent by the leading edge suction analogy,¹⁸ linear slender wing theory,¹⁹ or detached flow methods.²⁰ The Polhamus's leading edge suction analogy is probably the most widely applicable method to estimate the vortex lift of different planforms at different flight speeds. This analogy assumes that the vortex lift has the same magnitude as the potential-flow force which is lost because of the separation at the sharp leading edge.²¹ The method has provided good results for the attached vortices.¹⁸

As the angle of attack increases, the core of leading edge vortices will move inboard and secondary vortices can be formed below the main vortices.²² Ornberg¹⁶ in 1954 and Marsden and his colleagues²³ in 1958 reported the existence of these secondary vortices. They found that the secondary vortices form below and outboard the main wing vortices with opposite circulation. The leading-edge vortices can separate near the surface because of the adverse pressure gradients in the spanwise direction.²³ These separated flows may then roll up to form smaller secondary vortices of the opposite sign of vorticity which tend to move the primary vortices inboard and upward.⁷

Leibovich²⁴ showed that in a slender delta wing, each leading-edge vortex core is approximately one core diameter above the lifting surface of the wing. Over a nonslender wing, however, the vortices are formed much closer to the surface of the wing, therefore, the interaction of the secondary vortices with the shear layer of the primary vortex causes the primary vortex to split into a dual primary vortex structure.²⁵ Since the cores of vortices over nonslender wing are much closer to the surface and its boundary layer, the flow over nonslender wings is more sensitive to Reynolds number than flows over slender wings.²⁵ The vortical flow separation also occurs at lower angles of attack compared with a slender delta wing.¹¹

The leading-edge vortices have significant effects on the aerodynamic behavior of aircraft; they form regions of high vorticity and low-pressure over the upper wing surface that cause a nonlinear increase in lift until the maximum attainable lift with attached flow. At high angles of attack, the vortex structures change dramatically, leading to vortex breakdown, which is known to cause nonlinear aerodynamic behavior. Vortex breakdown is characterized by a sudden deceleration of the axial flow in the vortex core, a decrease in

circumferential velocity, and an increase in the vortex size and turbulent dissipation.²⁶ The onset of vortex breakdown starts from the trailing edge of the wing and moves forward on the wing with increasing angle of attack until, at sufficiently high angle of attack, the flow is dominated by the periodic wake shedding encountered over bluff bodies.²⁷ Note that a slender wing attains its maximum lift and stalls approximately when the onset of vortex breakdown crosses the trailing edge, while wings with smaller sweep angles stall when the onset of vortex breakdown moves towards the wing apex.²⁶

One of the methods to reduce the vortex drag is using a rounded leading edge.²⁸ While the leading edge suction is (normally) lost in the sharp edges, a large portion of the leading-edge suction is restored in a round edge and hence the drag force becomes smaller. However, the blunt tips fundamentally change the vortical flow behavior and structure. On delta wings with rounded leading edges, the flow separation point is not fixed at the leading edge and depends on the Reynolds number and the leading edge curvature. The origin of the leading edge vortex is at the delta wing apex for a sharp-edged wing but it is further downstream for a rounded tip.²⁹ The leading-edge vortices from sharp edges are steady for a wide range of angles of attack. Only if the angle of attack increases greatly, these vortices become unsteady and separate starting from the trailing edge of the wing. The flow at blunt nose, however, separates at moderate to high angles of attack starting from an outboard and aft location near the trailing edge²⁹

III. CFD Solver

Cobalt solves the unsteady, three-dimensional, compressible Navier-Stokes equations in an inertial reference frame. Arbitrary cell types in two or three dimensions may be used; a single grid therefore can be composed of different cell types.³⁰ In Cobalt, the Navier-Stokes equations are discretized on arbitrary grid topologies using a cell-centered finite volume method. Second-order accuracy in space is achieved using the exact Riemann solver of Gottlieb and Groth,³¹ and least squares gradient calculations using QR factorization. To accelerate the solution of the discretized system, a point-implicit method using analytic first-order inviscid and viscous Jacobians is used. A Newtonian sub-iteration method is used to improve the time accuracy of the point-implicit method. Tomaro et al.³² converted the code from explicit to implicit, enabling Courant-Friedrichs-Lewy (CFL) numbers as high as 10⁶. In Cobalt, the computational grid can be divided into group of cells, or zones, for parallel processing, where high performance and scalability can be achieved even on ten thousands of processors.³³ Some available turbulence models in Cobalt are the Spalart-Allmaras (SA) model, ³⁴ Spalart-Allmaras with Rotation Correction (SARC), ³⁵ and Delayed Detached-eddy simulation (DDES) with SARC.³⁶

IV. Test Case

The diamond wing used for this work was designed within the NATO RTO task group AVT-183. The objective of this task group was reliable prediction of separated flow onset and progression for air and sea vehicles. The AVT-183 wing is based on the SACCON UCAV geometry of AVT-161 research program³⁷ but it retains a simple and less complicated design compared to SACCON. In more details, the SACCON has a lambda wing planform with a leading edge sweep angle of 53° as shown in Fig. 2. The main sections of the SACCON model are the fuselage, the wing section, and wing tip. The configuration is defined by three different profiles at the root section of the fuselage, two sections with the same profile at the inner wing, forming the transition from the fuselage to wing and the outer wing section.

The spanwise distributions of thickness in percent chord and leading-edge radius of SACCON are shown in Figure 3. According to this figure, the leading edge radius is sharp at the root chord and then increases in the spanwise direction up to the intersection between fuselage and wing and then decreases. Figure 3 also shows that the thickness ratio in spanwise direction decreases. Finally, the outer wing section profile is twisted by 5^o around the leading edge to reduce the aerodynamic loads and shift the onset of flow separation to higher angles of attack.

The combination of sweep angle with sharp-blunt leading edges and the twist angle makes the flow around SACCON very complicated and difficult to predict even for static conditions. ^{38,39,40} This is due to formation of an apex vortex and a tip vortex which are formed by the onset and progression of the flow at the sharp and blunt leading edges at moderate angles of attack. At higher angles of attack these vortices become stronger and the onset of the tip vortex moves inboards. Over a small range of angle-of-attack, two vortices merge and coalesce to form much a stronger and deeper vortex which suddenly changes the pitch moment values.

At higher angles, vortices breakdown and again cause severe pitch moment changes.

For all above reasons, although CFD results of AVT-161 match each other at small angles of attack but they predicted different values at moderate to high angles of attack; besides none of codes could match the SACCON experimental data for the full range of angles of attack. To follow up the vortex flow studies of AVT-161 and gain information to understand why some CFD codes miss or match the leading-edge separation aerodynamics of interest, the work of AVT-183 has been focused on a new geometry with simpler design complexity than the SACCON. The new wing has a constant radius blunt leading edge in spanwise direction. The thickness ratio is also constant and the wing is non-twisted. In addition, the trailing edge has swept forward 26.5-degrees to form a diamond wing. This design has been compared with the SACCON geometry in Fig. 4.

Figure 5 shows the diamond wing layout used in the wind tunnel experiments. The wind tunnel model was places on a peniche with height of 9 cm to minimize the boundary layer effects from the wing tunnel wall. Figure 5 shows that the diamond wing wind tunnel model has a root chord of 1.2 m, slightly bigger than SACCON. The wing half span is approximately 0.65m. The moment reference point (x_{mrp} is located at 0.49 m from apex. A constant NACA64A006 airfoil section was used. The airfoil shapes at some spanwise

locations are shown in Figure 6.

A hybrid RANS mesh was generated for this model. The mesh was generated in two steps. In the first step, the inviscid tetrahedral mesh was generated from a clean configuration using the ICEM-CFD code. The inviscid mesh was then used as a background mesh by TRITET^{41,42} which builds prism layers using a frontal technique. TRITET rebuilds the inviscid mesh while respecting the size of the original inviscid mesh from ICEM-CFD. Mesh overview is shown in Figure 7. The grid is symmetric configuration and contains 5.4 million points and 13.2 million cells.

V. Wind Tunnel Experiments

A half model of the diamond wing was built for wind tunnel testing. The model layout is shown in Figure 5. The experiments of the diamond wing were carried out at the Technische Universität München subsonic wind tunnel. Figures 8 shows the wing model with a peniche in the test section of this wind tunnel. The wind tunnel is operable in a closed- and open-circuit mode with a suction configuration. Test section area is $1.80 \, \mathrm{m} \times 2.40 \, \mathrm{m}$ with a length of 4.8 meters. The wind tunnel maximum speed is about 65 m/sec.

All experiments were conducted for an angle of attack sweep at Mach number of 0.15 and Reynolds number of 2.7× 10⁶ based on the mean aerodynamic chord. An external six-component balance was used to measure the forces and moments acting on the model only and not the peniche. A stereo particle image velocimetry (PIV) technique was also used to measure flow field properties and detect vortical flows. The PIV technique was done with a laser and two cameras. The camera and laser positions are highlighted in Figure 8. For each test with different camera angles, about 400 images were captured. These images were processed using LaVision DaVis software. The experimental data include averaged lift, drag, and pitch moment coefficients for all test runs over the range of tested angles of attack. Besides, the surface pressure coefficients were measured for a number of slices at different chord-wise locations. These slices are shown in Figure 9.

VI. Results and Discussion

Steady and unsteady simulations of the diamond wing were carried out with different turbulence models. All simulations retain second-order spatial accuracy and use an implicit temporal operator to advance the flow solution in time. However, the steady-state cases are first-order accurate in time and were computed with a CFL of one-million. Unsteady computations were performed using second-order temporal accuracy and three Newton sub-iterations. The effects of the time step on the predictions are evaluated for unsteady simulations.

Turbulence models considered include the Spalart-Allmaras (SA) model, Spalart-Allmaras with Rotation Correction (SARC), and Delayed Detached-eddy simulation (DDES) with SARC.³⁶ Note that the DDES formulation will improve predictions of flows with massive separation which are time-dependent flows. Therefore, all DDES simulations were performed using second-order temporal accuracy and three Newton sub-iterations.

The computed overall lift, drag, and pitch moment coefficients using the SA turbulence model are shown in Figure 10 and compared to experimental data. These simulations are steady-state type and correspond to an angle-of-attack sweep from zero to 20° with a 0.5 degrees increment for angles between 8 to 16 degrees and one degree increment for all other angles. These angles are selected allowing us to compare CFD predictions with static pressure measurements in the wind tunnel at each of these angles. Two CFD data sets are presented in Figure 10; the first dataset are simulated for 1,500 iterations for all angles of attack; the second dataset corresponds to simulations that run for more iterations (3,000) at some high angles of attack. Figure 10 shows that the computed overall lift, drag, and pitch moment coefficients from both simulations match very well, indicating that the force and moment coefficients have already reached their final values at iteration 1,500 and they do not change further in time.

Figure 10 shows that predictions of CFD with the SA turbulence model match very well with experiments at small angles of attack but they do not match at higher angles, except the drag force. At high angles of attack, CFD lift data overestimate and pitch moment predictions underestimate the measurements; also the experiments show that there is a break in the pitch moment curve around 8° angle of attack; CFD using the SA model, however, shows the break in pitch moment curve at a much higher angle (around 12°).

Results of steady-state simulations with the SARC turbulence models are compared with experiments and predictions obtained from the SA model in Figure 11. These simulations were first-order accurate in time and were computed with a CFL of one-million; however they ran for 6,000 iterations to allow forces and moments reaching their final values. Figure 11 shows that the SARC and SA turbulence model predictions are in good agreement with each other and experiments at small angles of attack. However, at moderate to high angles, predictions from these turbulence models are different: the SARC drag values are slightly larger than the SA model as well as experiments; the lift coefficients from the SARC model are slightly smaller than predicted lift from the SA model and become closer to the experiments for angles of attack above 15 degrees. The SARC pitch moment values agree well with experiments at moderate angles of attack but they are off for angles above 15 degrees. The SARC model accurately predicts the pitch moment break seen in the experiments around 8° angle of attack.

Figure 12 shows the effects of the time step size in the unsteady SARC computations compared with the steady SARC predictions. Unsteady computations were performed using second-order temporal accuracy and three Newton sub-iteration with time step sizes of 2e-4 and 4e-5 seconds. These unsteady simulations were ran for 6,000 iterations and the overall forces and moments were averaged for the last 3,000 iterations. The results in Figure 12 reveal that discrepancies between the steady and unsteady predictions are very small; this indicates that the flow is steady and attached over the surfaces in this angle of attack range.

Figures 13 and 14 present the flow visualization around the diamond wing at different angles of attack by using the SA and SARC turbulence models, respectively. Visualization of vortices over the upper surfaces was done by using iso-surfaces of vorticity; the surface and vortices in these figures were colored with the pressure coefficient ranging from -3 to 2. These figures show that visualization plots for $\alpha = 4^{\circ}$ are very similar for the SA and SARC models. At this angle, the flow separates at the wing-tip near trailing edge due to considerable pressure difference between the lower and upper surfaces. This separated flow then rolls up into a small-size tip vortex which can be seen in Figures 13(a) and 14(a). These figures show that at the wing leading edge, there is a positive spanwise pressure gradient towards the center of wing. The pressure gradient becomes larger at the wing tip.

At six degrees angle of attack, the tip vortex becomes stronger as shown in Figures 13(b) and 14(b). However, the size of the vortex predicted by the SARC turbulence model is larger than the one predicted by the SA model. The vortex predicted from SARC is also located further upstream. Notice that the pressures at the leading edge are smaller than four angle of attack case; the spanwise pressure gradient is therefore larger at six degrees angle of attack. Figures 13 and 14 show that at about 8° angle of attack, a leading edge vortex is formed above the wing. This leading-edge vortex originates from about 0.4 and 0.6 c_r (the chord length at the wing root) for the SARC and SA models, respectively. Again the SARC predicted vortex is bigger and stronger than the vortex predicted by the SA model. These leading-edge vortices merge with the tip vortex. A low pressure region is formed above the upper surface around the vortex core. Vortices also increase in size as they extend downstream.

As angle of attack is further increased, the leading-edge vortices become stronger and bigger; the vortex starting point also moves upstream. For example at ten degrees angle of attack, the starting points of vortices predicted by the SA and SARC models are at about 0.5 and 0.3 c_r , respectively. The center of the vortex also moves inboard with increasing angle of attack.

More details of the flows around the diamond wing can be found in Figures 15-22 which compare predicted pressure coefficients by the SA and SARC model against experiments for several angles of attack. In these figures, the corresponding pressure distributions on the upper and lower surfaces of the wing are shown. Figure 15 shows that at all chord-wise locations, considered in this work, CFD predictions from both turbulence models match well with each other and experiments. In all plots of this figure, moving towards the wing tip (y/s=1) a positive and a negative pressure gradient exist at the lower and upper surface, respectively. The pressure curves for $\alpha=4^{\circ}$ are smooth with a minimum pressure at the wing tip. Figure 15 shows that no vortex-type flow is present for the range of chordwise locations considered.

Figure 16 compares the pressure distribution plots at $\alpha=6^{\circ}$. The pressure differences between the upper and lower surfaces are larger than plots at $\alpha=4^{\circ}$. CFD pressure values match with experiments almost everywhere. The largest discrepancies in plots can be seen at $0.6c_r$. At this location, the SARC model predicts a negative pressure region in the upper surface near the wing tip due to the tip vortex presence; the vortex core is located about y/s=0.93. However, SA and experiment results do not predict the existence of such a vortex at this location and angle. Figure 16 shows that at $0.6c_r$, there is a positive spanwise pressure gradient towards the wing tip at the vortex boundaries. The lower surface pressure distributions at this angle of attack are smooth and have no interesting flow features present.

The pressure differences between the upper and lower surfaces at $\alpha=8^{\circ}$ even become larger. The lower surface pressure distributions show no interesting flow feature again as shown in Figure 17. However, the upper surface has a strong negative dip at some chordwise locations due to the presence of a leading edge vortex. The SARC model exhibits the vortex presence even at $0.395c_r$. As flow moves downstream, the predicted vortex becomes bigger (the dip becomes wider), however the pressure values become less negative. The SA predicts a vortex above the upper surface as well. This vortex is seen only at $0.6c_r$. Experiment results also exhibit a vortex starting around $0.5c_r$. Figure 17 shows that pressure distributions predicted by CFD do not exactly match with experiments around vortices.

As angle of attack is increased to $\alpha=10^\circ$, the SARC predicted vortex is moved further upstream, at about $0.295c_r$ as shown in Figure 18. The vortex core is also moved inboard. For example, Figure 17 shows that for $\alpha=8^\circ$ at $0.395c_r$, the vortex core is located about y/s=0.95; the vortex core is located at about y/s=0.85 for $\alpha=10^\circ$. Experiment results exhibit that a vortex is formed starting at $0.395c_r$. The SA model, however, predicts the vortex starting point at $0.5c_r$. CFD data and experimental results show that the predicted vortex becomes larger in size and the pressure values become less negative as the flow moves upstream. Also, a positive spanwise pressure gradient is predicted towards the wing tip at the vortex boundaries in the simulation and experimental results.

At 12 degrees angle of attack, experimental results shows a vortex starting at $0.395c_r$; the SARC and SA vortices now originate from $0.295c_r$ and $0.395c_r$, respectively. The vortices become bigger and induce more negative pressure regions as shown in Figure 19. For example, at $0.6c_r$ the vortex diameter is about 0.4 of half-span length. As the angle of attack is further increased, vortices predicted from CFD and experiments become much bigger. At high angles of attack, the pressure distribution becomes more uniform across the vortex at upstream locations.

Final results compare CFD pedictions using DDES-SARC turbulence model with experiments. DDES simulations ran for 12,000 iterations using a second-order time accuracy and a time step of 4e-5 second. Lift, drag, and pitch moment coefficients were averaged for the last 6,000 iterations. Figure 23 compares the DDES-SARC predictions with experiments as well as the SARC predictions. The results show that even predictions from the DDES-SARC model do not match with experiments; prediction curves with the angle of attack are not smooth as well. Notice that the flow is steady-state at these angles and a DDES model probably do not much help to improve predictions.

VII. Conclusions

While the vortical flow behavior over slender wings with sharp leading edges has been studied extensively for over last few decades, much less is known about the formation of vortices over wings with lower sweep angles and blunt leading edges. In the latter, the vortex flow structure is very complicated and depends heavily on the leading edge bluntness and the wing sweep angle. These vortices can have significant effects on the aircraft stability and control characteristics.

CFD potential and limitations for predicting vortical flowfields were investigated over a generic 53-degree swept diamond wing with blunt tips. The diamond wing considered in this paper was designed under STO

AVT Task Group 183. The wing planform is based on the SACCON UCAV geometry. The SACCON wing trailing-edge was swept forward by 26.5-degrees to form a diamond-shaped planform. The new wing has a constant airfoil section of NACA 64A-006 with a leading edge radius of 0.264 in percent chord. The wind tunnel experiments of the diamond wing were carried out in the Institute of Aerodynamics and Fluid Mechanics of Technische Universität München, Germany and include aerodynamic lift, drag, and pitch moment measurements as well as span-wise pressure distributions at different chord-wise locations. This data set is used to validate CFD results.

Turbulence models considered included the Spalart-Allmaras (SA) model, Spalart-Allmaras with Rotation Correction (SARC), and Delayed Detached-eddy simulation (DDES) with SARC.³⁶ The results presented demonstrated that the pitch moments predicted by the SARC turbulence model provided a better match to experimental results than the SA model at moderate angles of attack. However, at high angles of attack, all pitch moment predictions were off. The flow visualization results showed that a leading-edge vortex is formed above the upper surface of the wing at an angle of attack about eight degrees. This vortex became larger and stronger as the angle of attack was increased. With increasing angle of attack, the vortex starting point moved upstream and the vortex core moved inboard towards the wing root. The results also showed that for the range of angles of attack considered in this work, the flow over the diamond wing was steady, because the vortices were attached and stationary at each angle of attack. For this reason, predictions from the DDES-SARC model also did not match with experiments.

VIII. Acknowledgements

Mehdi Ghoreyshi is supported by USAFA under contract FA70001320018. Their financial support is gratefully acknowledged. Computer time was provided by the Department of Defense Engineering Research Development Center (ERDC). The experimental data were provided in the framework of STO AVT Task Group 183 by the Institute of Aerodynamics and Fluid Mechanics of Technische Universität München, München, Germany. The authors appreciate the support provided by the High Performance Computing Research Center at USAFA.

References

- ¹Torenbeek, E. and Wittenberg, H., Flight Physics: Essentials of Aeronautical Disciplines and Technology, with Historical Notes, Springer, 2009.
- ²Gad-el Hak, M. and Blackwelder, R. F., "The Discrete Vortices From a Delta Wing," AIAA Journal, Vol. 23, No. 6, 1985, pp. 961–962, DOI: 10.2514/3.9016.
- ³Houghton, E. L., Carpenter, P. W., Collicott, S., and Valentine, D., Aerodynamics for Engineering Students, Elsevier, 2013.
- ⁴Mitchell, A., Molton, P., Barberis, D., and Delery, J., "Vortical Substructures in the Shear Layers Forming Leading-Edge Vortices," AIAA Paper 2001–2424, June 2001.
- ⁵Mangler, K. W. and Smith, J. H. B., "A Theory of the Flow Past a Slender Delta Wing with Leading Edge Separation," Proceedings of the Royal Society of London. Series A, Mathematical and Physical Sciences, Vol. 251, No. 1265, 1959, pp. 200–217.
- ⁶Morton, S., Forsythe, J. R., Mitchell, A. M., and Hajek, D., "DES and RANS Simulations of Delta Wing Vortical Flows," AIAA Paper 2002–0587, January 2002.
- ⁷Agrawal, S., Barnett, R. M., and Robinson, B. A., "Numerical Investigation of Vortex Breakdown on a Delta Wing," *AIAA Journal*, Vol. 30, No. 3, 1992, pp. 584–591.
- ⁸Thomas, J. L., Krist, S. T., and Anderson, W. K., "Navier-Stokes Computations of Vortical Flows Over Low-Aspect-Ratio Wings," AIAA Journal, Vol. 28, No. 2, 1990, pp. 205–212.
- ⁹Gursul, I., Gordnier, R., and Visbal, M., "Unsteady Aerodynamics of Nonslender Delta Wings," Progress in Aerospace Sciences, Vol. 41, 2005, pp. 515557.
- ¹⁰Vallespin, D., Da Ronch, A., Badcock, K. J., and Boelens, O. J., "Vortical Flow Prediction Validation for an Unmanned Combat Air Vehicle Model," *Journal of Aircraft*, Vol. 48, No. 6, 2011, pp. 1948–1959.
- ¹¹Elsayed, M., Scarano, F., and Verhaagen, N. G., "Leading-Edge Shape Effect on the Flow over Non-Slender Delta Wings," AIAA Paper 2008–344, January 2008.
- ¹²Folk, C. and Ho, C. M., "Micro-Actuators for Control of Delta Wing with Sharp Leading Edge," AIAA Paper 2001–0121, January 2001.
- ¹³Verhaagen, N. G., "Effects of Leading-Edge Radius on Aerodynamic Characteristics of 50° Delta Wings," AIAA Paper 2010–323, January 2010.
- ¹⁴Sun, Y. C., Experimental Investigation of the Flow Field About Sharp-Edged Delta and Rectangular Wings, M.a. sc., The University of British Columbia, 1961.

¹⁵Jensen, A. A., Wind tunnel investigation of a supersonic tailless airplane at low subsonic speed, Phd thesis, California Institute of Technology, 1948.

¹⁶Ornberg, T., "A Note on the Flow Around Delta Wings," KTH-Aero TN, 1954, pp. 961–962.

¹⁷Traub, L. W., "Comparative Study of Delta Wings with Blunt Leading Edges and Vortex Flaps," Journal of Aircraft, Vol. 33, No. 4, 1996, pp. 828–830, DOI: 10.2514/3.47022.

¹⁸Polhamus, E. C., "Prediction of Vortex-Lift Characteristics by a Leading-Edge-Suction Analogy," Journal of Aircraft, Vol. 8, No. 4, 1971, pp. 193–199.

¹⁹Jones, R. T., "Properties of Low Aspect Ratio Pointed Wings at Speeds Above and Below the Speed of Sound," NACA Rept. 835, 1946.

²⁰Mangier, K. W. and Smith, J. H. B., "Calculations of the Flow Past Slender Delta Wings with Leading Edge Separation," Royal Establishment, Farnborough, England, Rept. Aero. 2533, 1957.

²¹Snyder, M. H. and Lamar, J. E., "Application of the Leading-Edge Sunction Analogy to Prediction of Longitudinal Load Distribution and Pitching Moments For Sharp-Edge Delta Wings," NASA TN D-6994, 1972.

²²Vigneron, Y. C., Rakich, J. V., and Tannehill, J. C., "Calculation of Supersonic Viscous Flow Over Delta Wings With Sharp Subsonic Leading Edges," NASA TM-78500, 1978.

²³Marsden, D. J., Simpson, R. W., and Rainbird, W. J., "An Investigation into the Flow Over Delta Wings at Low Speeds with Leading Edge Separations." College of Aeronautics Report 114. A.R.C. 20 409, 1958.

²⁴Leibovich, S., "Vortex Stability and Breakdown: Survey and Extension," AIAA Journal, Vol. 22, No. 9, 1984, pp. 1192–1206.

²⁵Taylor, G. S., Schnorbus, T., and Gursul, I., "An Investigation of Vortex Flows Over Low Speed Delta Wings," AIAA Paper 2003-4021, June 2003.

²⁶Pamadi, B. N., Performance, Stability, Dynamics, and Control of Airplanes, AIAA Education Series, AIAA, Reston, Virginia, 2004.

²⁷Cummings, R. M., Forsythe, J. R., Morton, S. A., and Squires, K. D., "Challenges in High Angle of Attack Flow Prediction," Progress in Aerospace Sciences, Vol. 39, No. 5, 2003, pp. 369–384.

²⁸Rinoie, K., "Experiments on a 60-Degree Delta Wing with Rounded Leading-Edge Vortex Flaps," Journal of Aircraft, Vol. 37, No. 1, 2000, pp. 37–44, DOI: 10.2514/2.2559.

²⁹Luckring, J. M., "A Survey of Fsactors Affecting Blunt Leading-Edge Separation for Swept and Semi-Slender Wings," AIAA Paper 2010–4820, June 2010.

³⁰Strang, W. Z., Tomaro, R. F., and Grismer, M. J., "The Defining Methods of Cobalt: A Parallel, Implicit, Unstructured Euler/Navier-Stokes Flow Solver," AIAA Paper 1999–0786, 1999.

³¹Gottlieb, J. J. and Groth, C. P. T., "Assessment of Riemann Solvers For Unsteady One-dimensional Inviscid Flows of Perfect Gasses," *Journal of Computational Physics*, Vol. 78, No. 2, 1988, pp. 437–458.

³²Tomaro, R. F., Strang, W. Z., and Sankar, L. N., "An Implicit Algorithm For Solving Time Dependent Flows on Unstructured Grids," AIAA Paper 1997–0333, 1997.

³³Tomaro, R. F., Strang, W. Z., and Wurtzler, K. E., "Can Legacy Codes Scale on Tens of Thousands of PEs or Do We Need to Reinvent the Wheel?" 2012 High Performance Computing Modernization Program Contributions to DoD Mission Success, pp. 231-236, September 2012.

³⁴Spalart, P. R. and Allmaras, S. R., "A One Equation Turbulence Model for Aerodynamic Flows," AIAA Paper 1992–0439, January 1992.

³⁵Spalart, P. R. and Shur, M. L., "On the Sensitization of Turbulence Models to Rotation and Curvature," Aerospace Science Technology, Vol. 1, 1997, pp. 297302.

³⁶Spalart, P. R., Jou, W.-H., Strelets, M., and Allmaras, S. R., "Comments on the Feasibility of LES for Wings, and on a Hybrid RANS/LES Approach," In Proceedings, 1st AFSOR International Conference on DNS/LES, Greyden Press, Columbus, OH, 1997, pp. 137147.

³⁷Cummings, R. M. and Schütte, A., "An Integrated Computational/Experimental Approach to UCAV Stability & Control Estimation: Overview of NATO RTO AVT-161," AIAA Paper 2010–4392, June-July 2010.

³⁸Cummings, R. M., Jirasek, A., Petterson, K., and Schmidt, S., "SACCON Static and Dynamic Motion Flow Physics Simulation Using Cobalt," AIAA Paper 2010–4691, June-July 2010.

³⁹Frank, N., "Strategy for Dynamic CFD Simulations on SACCON Configuration," AIAA Paper 2010–4559, June-July 2010.

⁴⁰Vallespin, D., Da Ronch, A., Badcock, K. J., and Boelens, O., "Validation of Vortical Flow Predictions for a UCAV Wind Tunnel Model," AIAA Paper 2010–4560, June-July 2010.

41 Tyssel, L., "Hybrid Grid Generation for Complex 3D Geometries," Proceedings of the 7th International Conference on Numerical Grid Generation in Computational Field Simulation, 2000, pp. 337–346.
42 Tyssel, L. "The TRITET Grid Generation System" International Society of Grid Generation (ISGG)." Proceedings of

⁴²Tyssel, L., "The TRITET Grid Generation System," International Society of Grid Generation (ISGG)," Proceedings of the 10the International Conference on Numerical Grid Generation in Computational Field Simulations, 2000.

⁴³Luckring, J. M. and Boelens, O. J., "A Unit-Problem Investigation of Blunt Leading-Edge Separation Motivated by AVT-161 SACCON Research," presented at the RTO Applied Vehicle Technology Panel (AVT) Specialists Meeting held in Portsmouth, United Kingdom on 12 - 14 October 2011.

⁴⁴Hövelmann, A., Grawunder, M., and Breitsamter, C., "AVT-183 Wind Tunner Measurments at TUM-AER," 33th AVT-PBW, Copenhagen, Denmark, 2014.

WING VORTICES ON DELTA WING

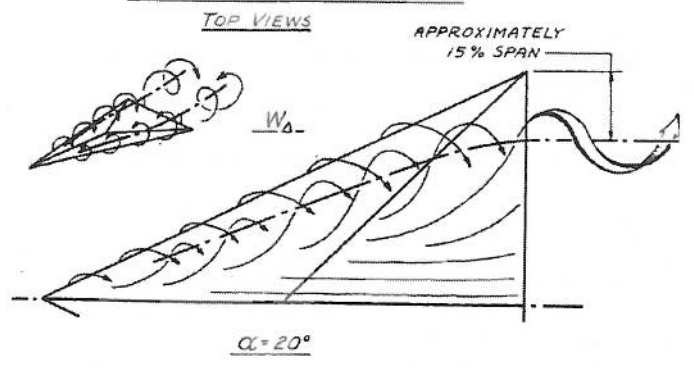


Figure 1. Jensen's sketch of leading edge vortices over a delta wing at $\alpha=20^{\circ}.^{15}$

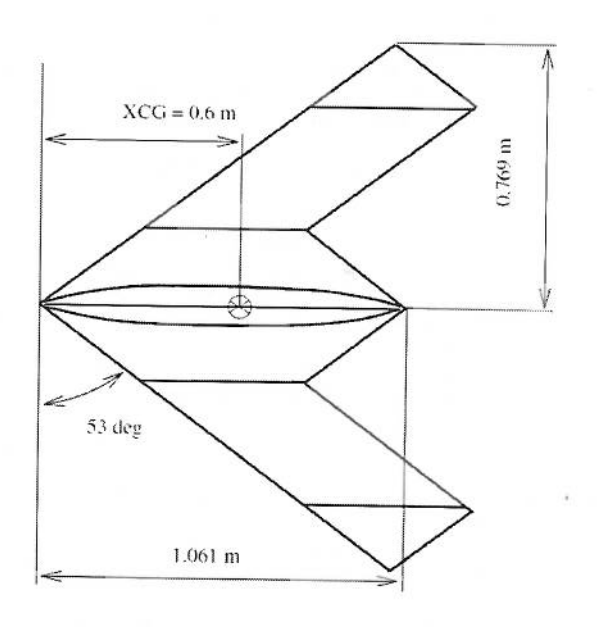


Figure 2. The SACCON geometry.

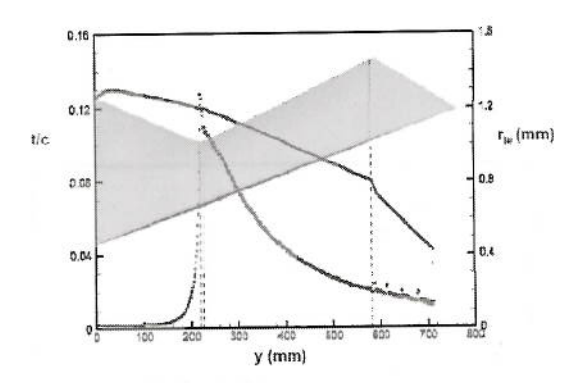


Figure 3. SACCON thickness and leading-edge radius. This picture is adapted from Ref 43.

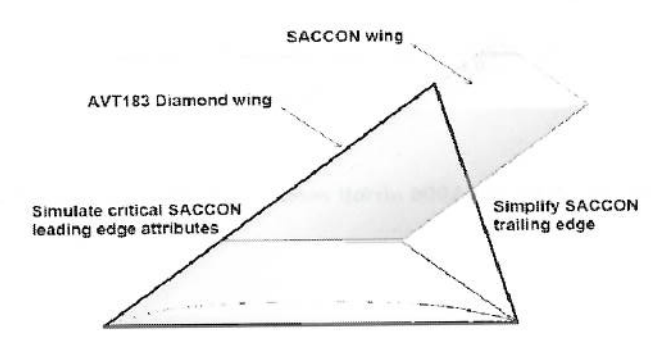


Figure 4. Diamond wing concept. This picture is adapted from Ref 43.

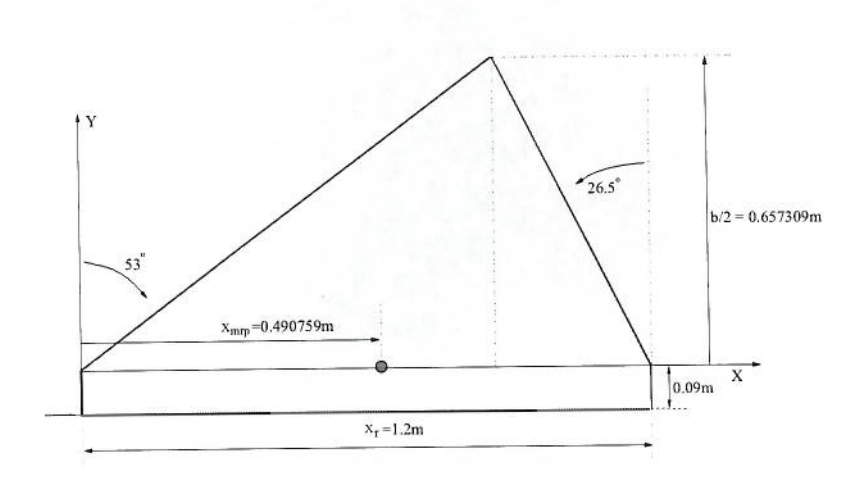


Figure 5. Diamond wing geometry

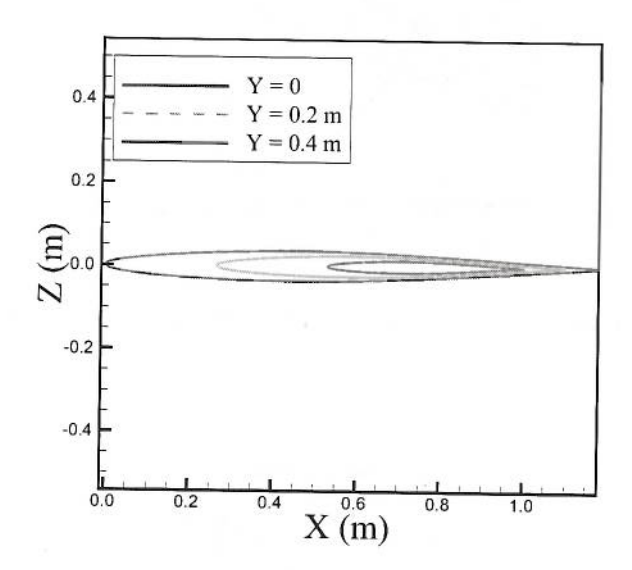


Figure 6. NACA64A006 airfoil section used in the diamond wing.

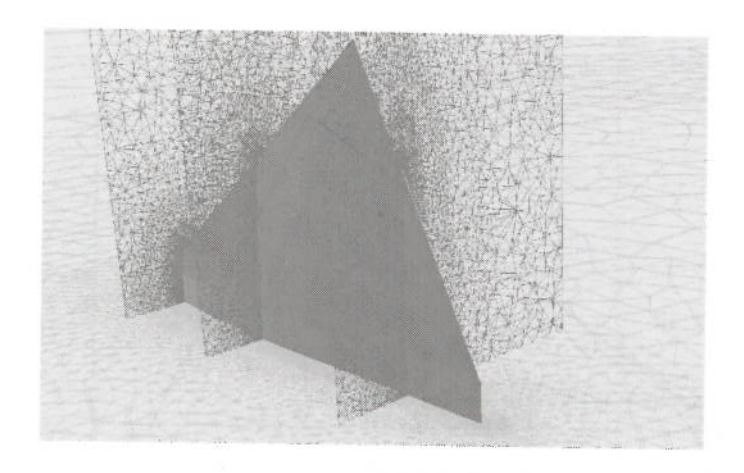


Figure 7. Diamond wing mesh.

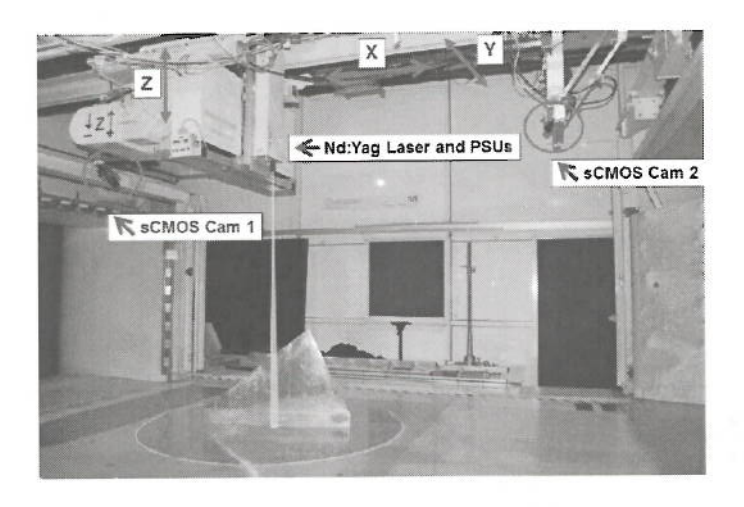


Figure 8. The AVT-183 diamond wing at the Technische Universität München wind tunnel. 44

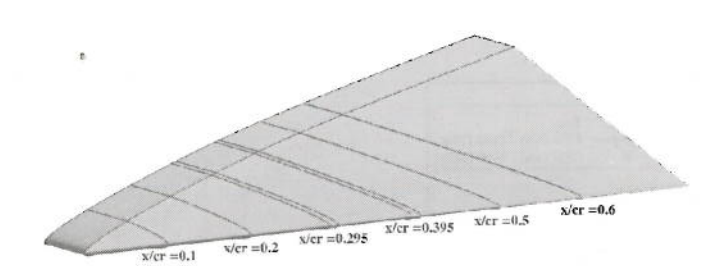


Figure 9. Pressure tap locations.

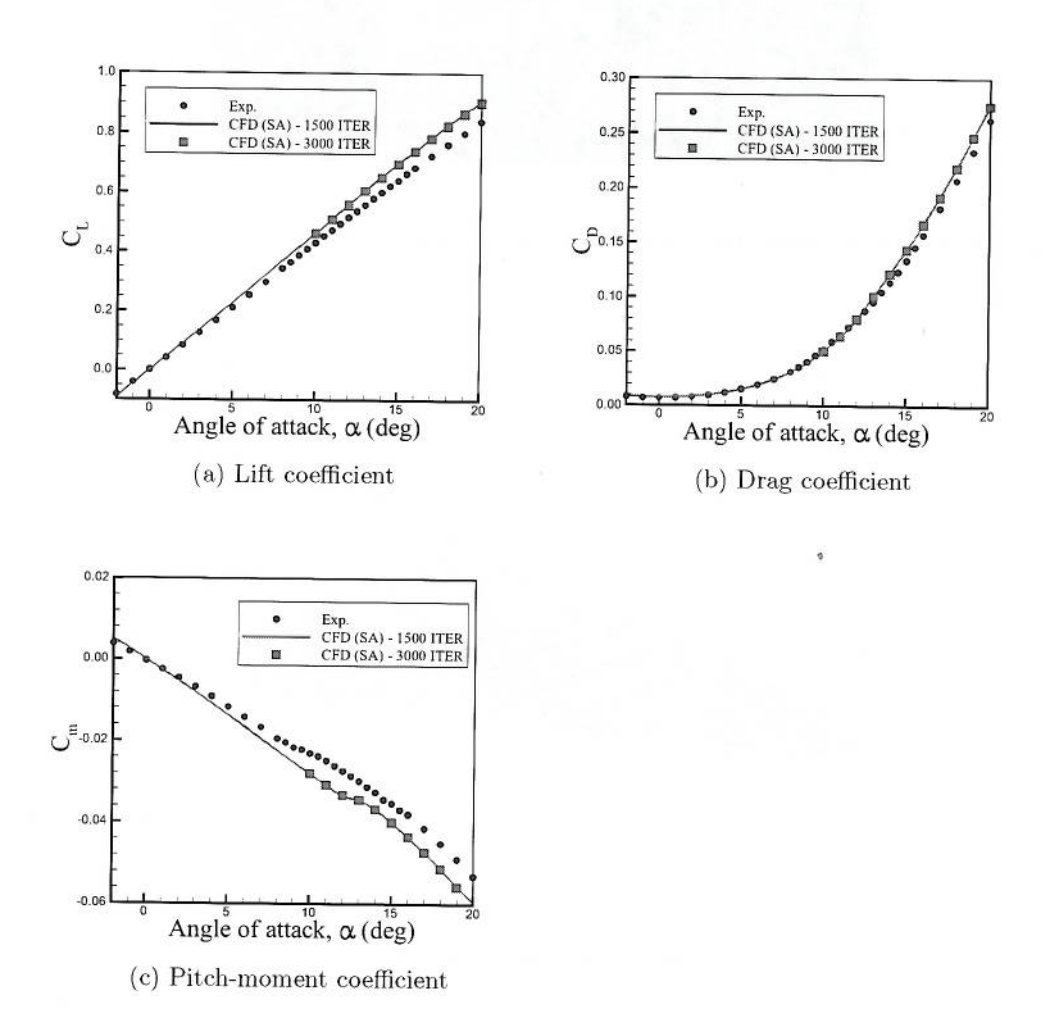


Figure 10. CFD predictions of Cobalt with SA turbulence model. Mach number is 0.15 with $Re = 2.7 \times 10^6$.

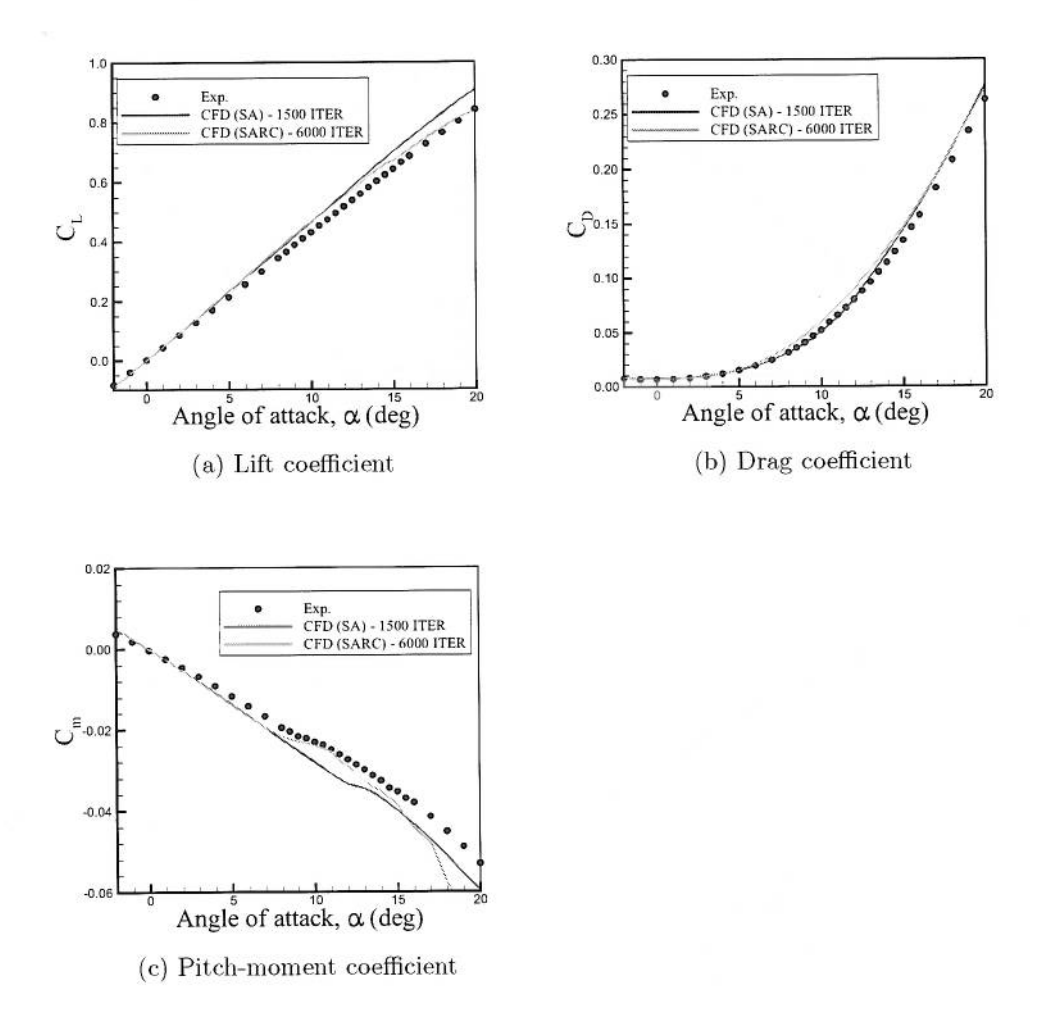


Figure 11. SARC versus SA data. In both, first order accuracy in time with one Newton sub-iteration were used.

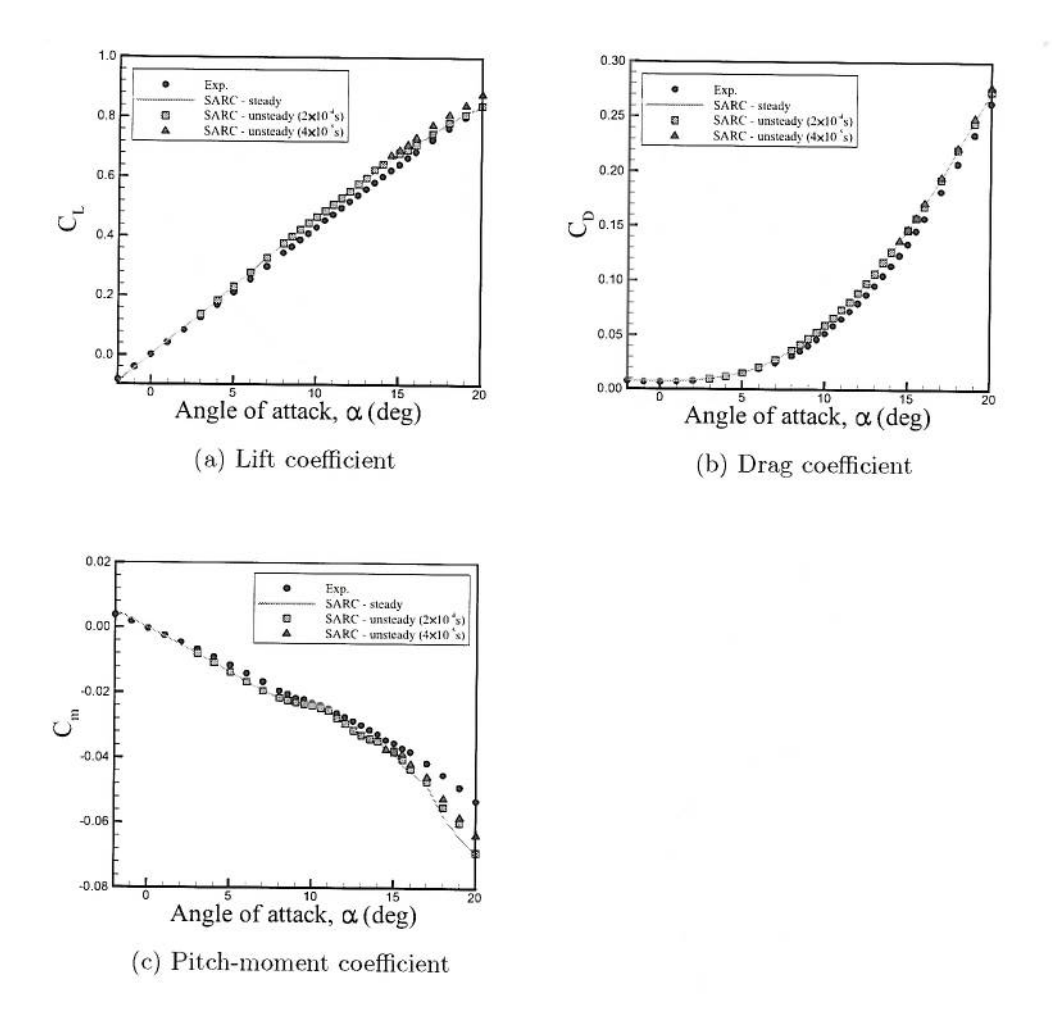


Figure 12. Unsteady simulations using SARC turbulence model. In all unsteady simulations, second order accuracy in time with three Newton sub-iteration were used. All unsteady coefficients are averaged values for last 3,000 iterations.

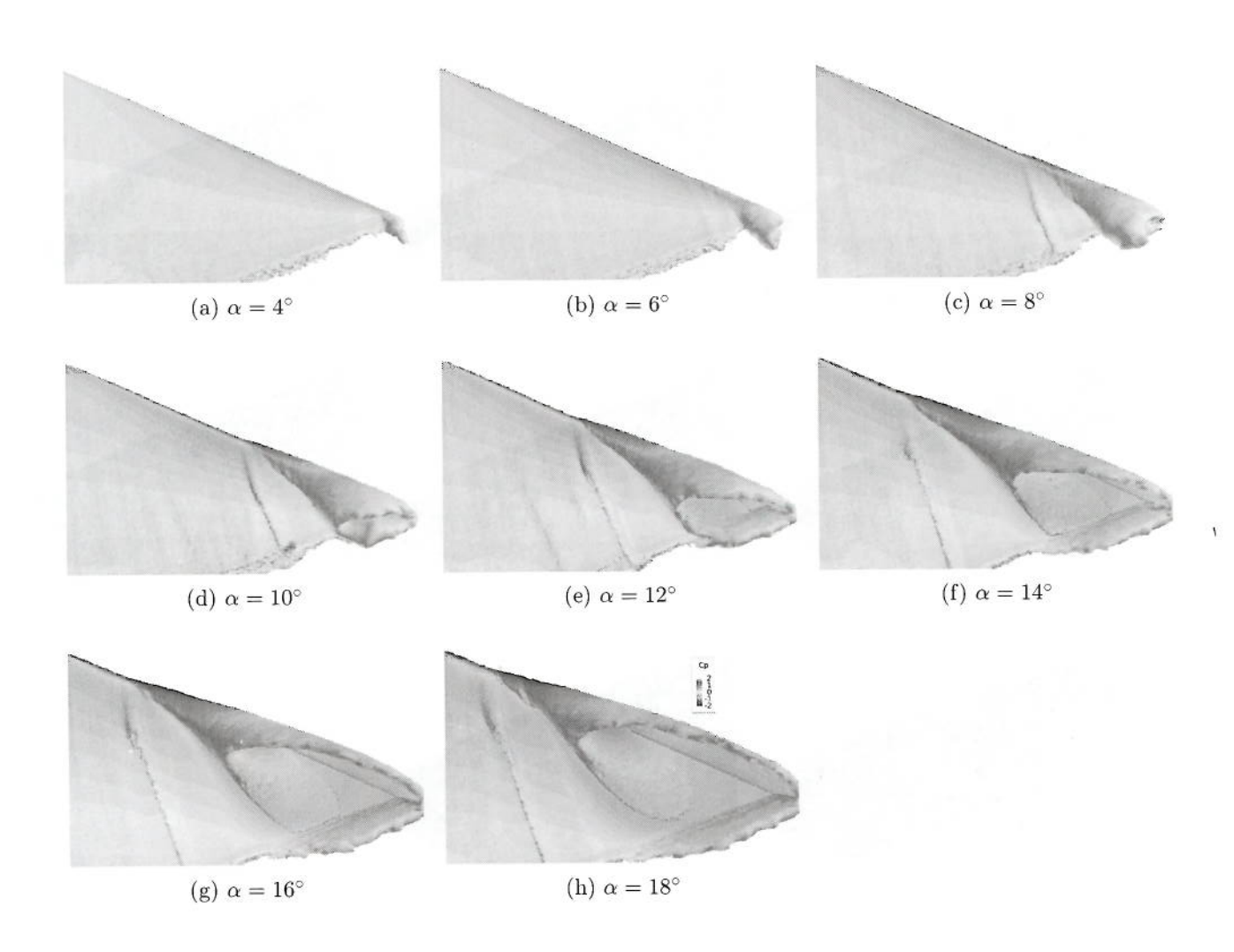


Figure 13. Vortical flows over the AVT-183 diamond wing using SA turbulence model.

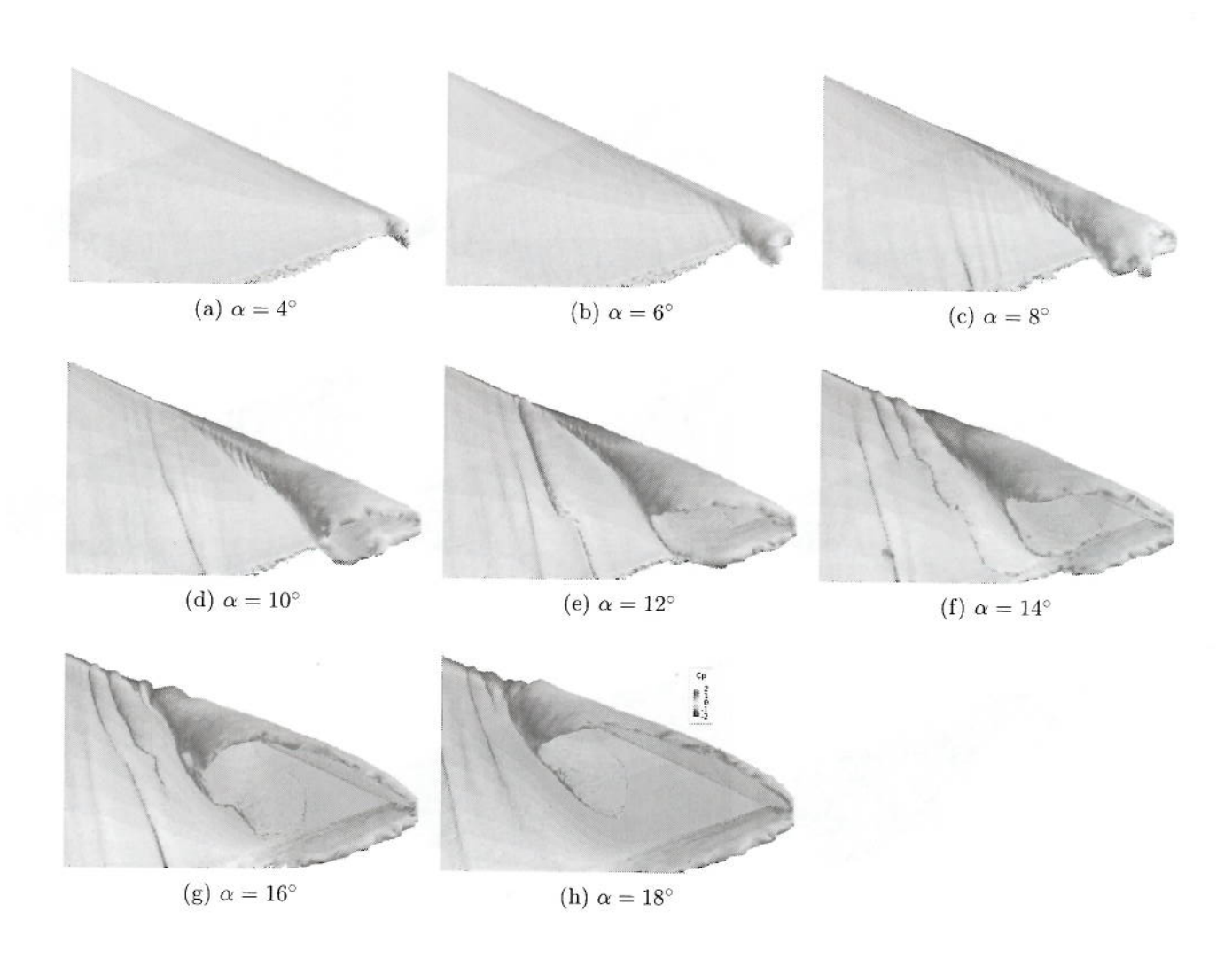


Figure 14. Vortical flows over the AVT-183 diamond wing using SARC turbulence model.

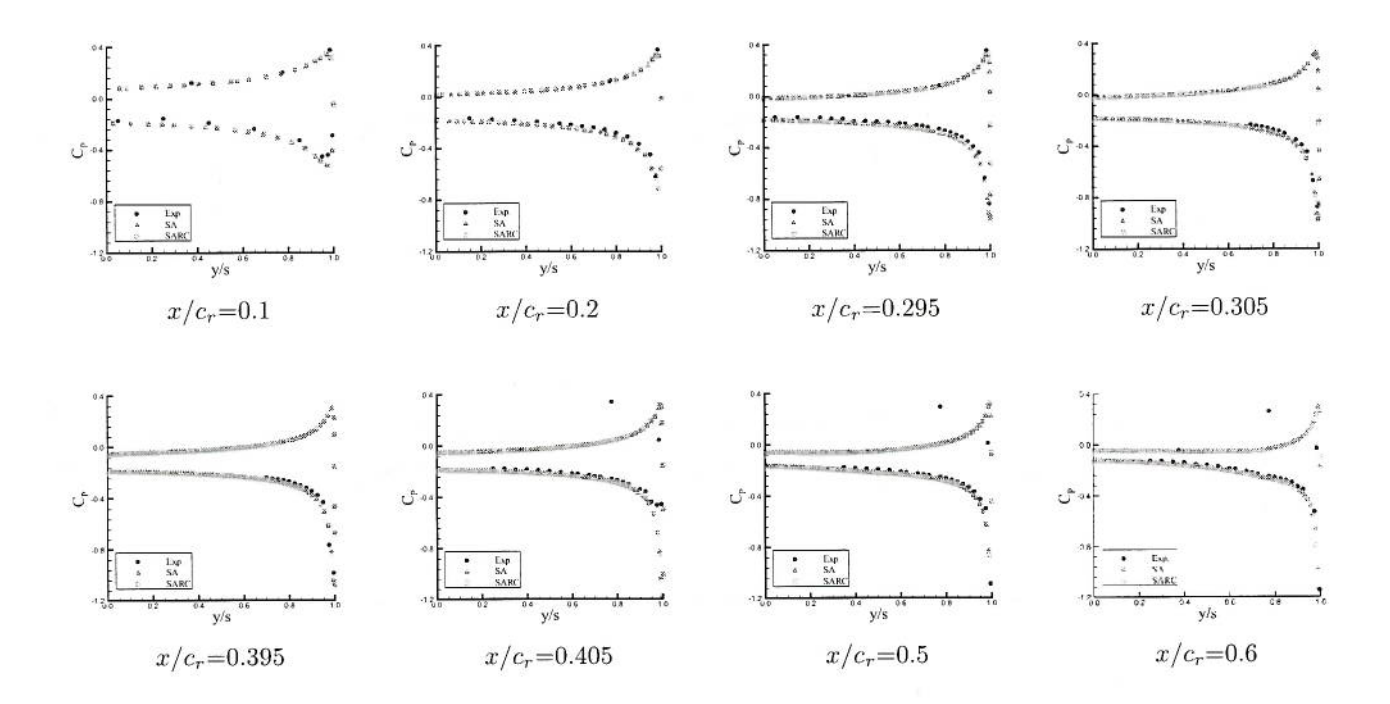


Figure 15. CFD pressure tap data at $\alpha=4^{\circ}$.

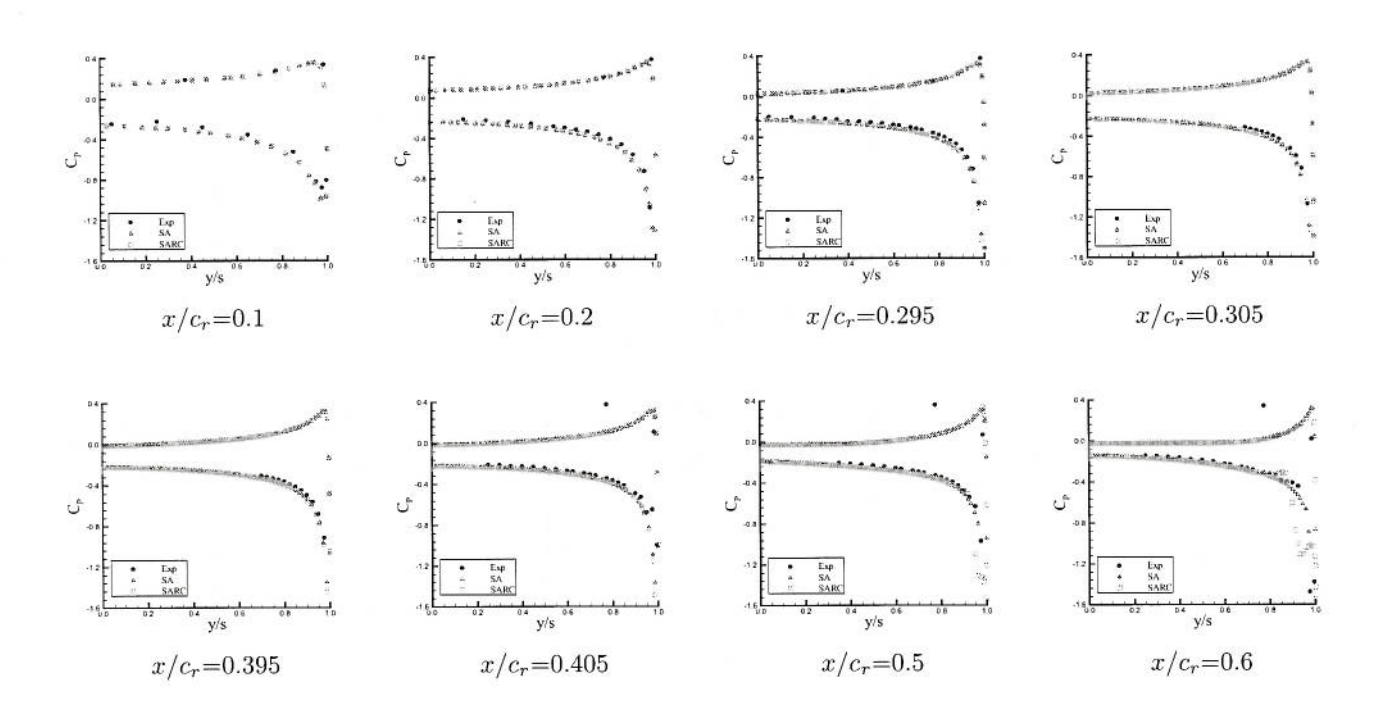


Figure 16. CFD pressure tap data at $\alpha=6^{\circ}$.

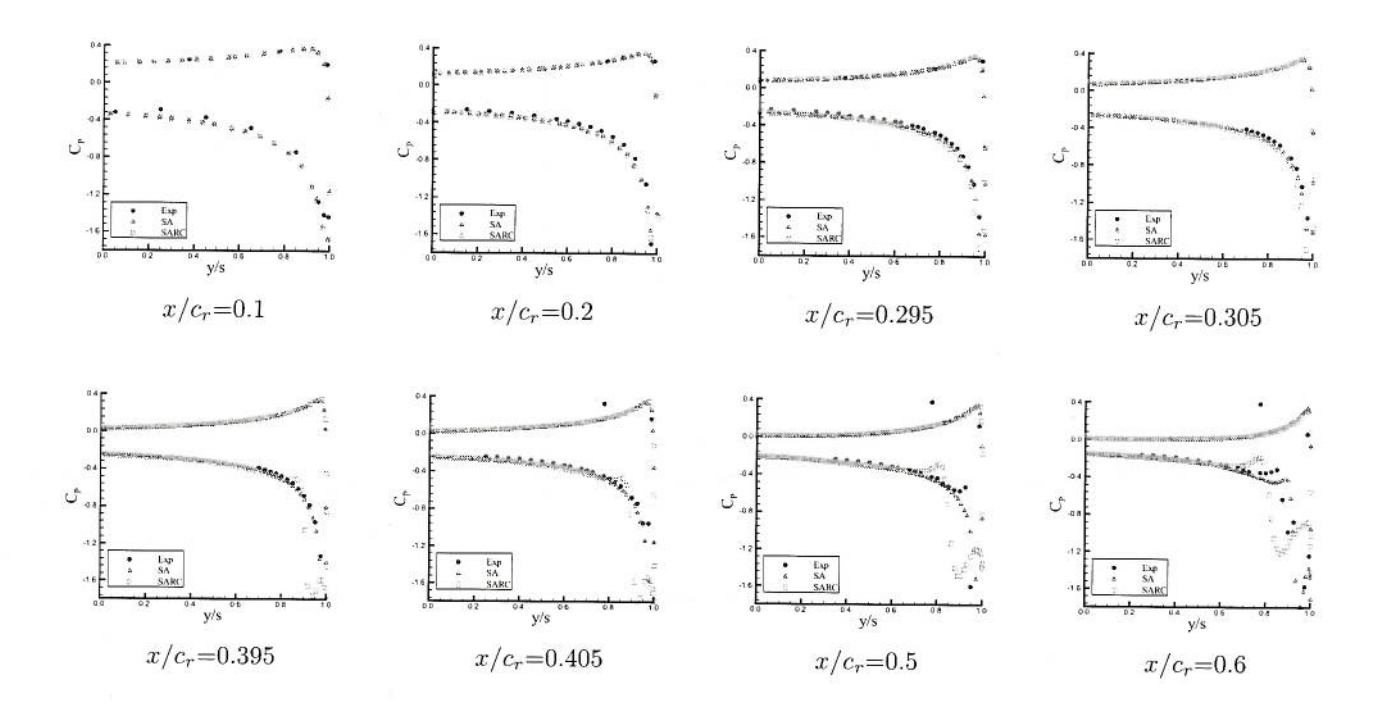


Figure 17. CFD pressure tap data at $\alpha=8^{\circ}.$

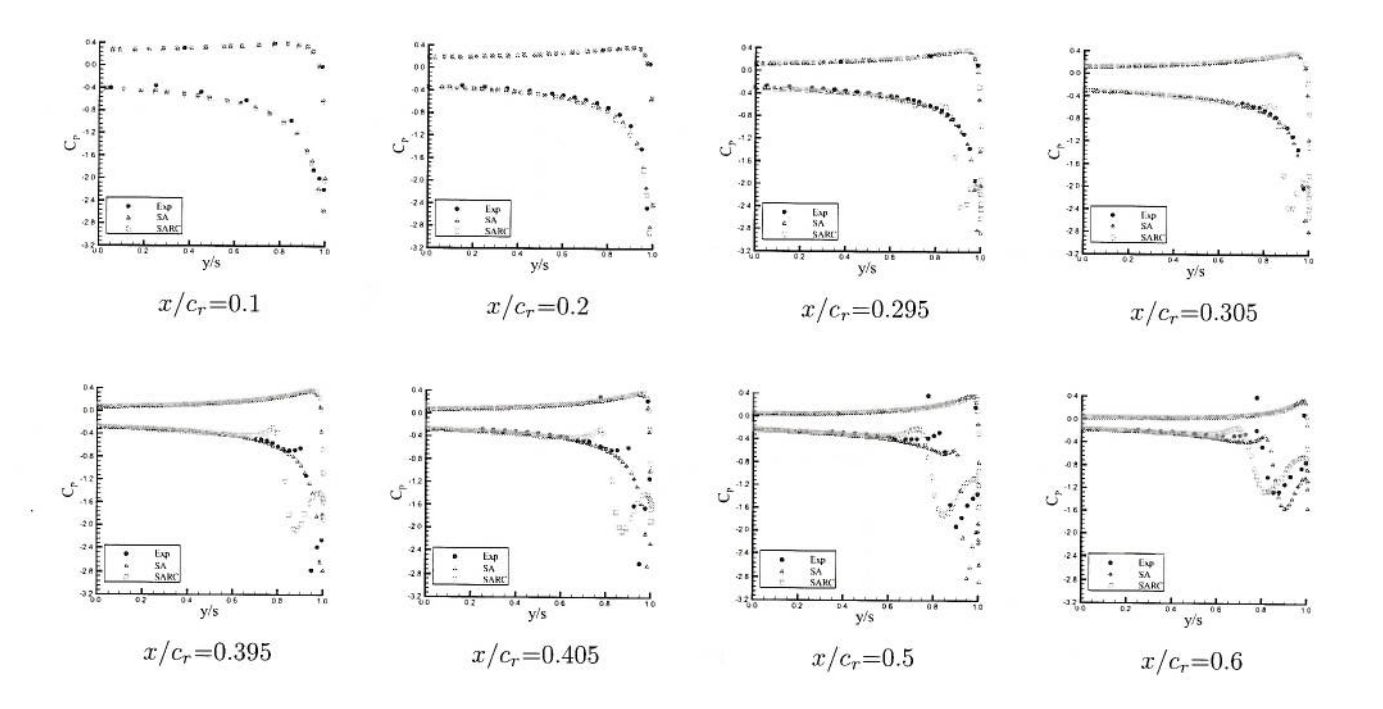


Figure 18. CFD pressure tap data at $\alpha=10^{\circ}$.

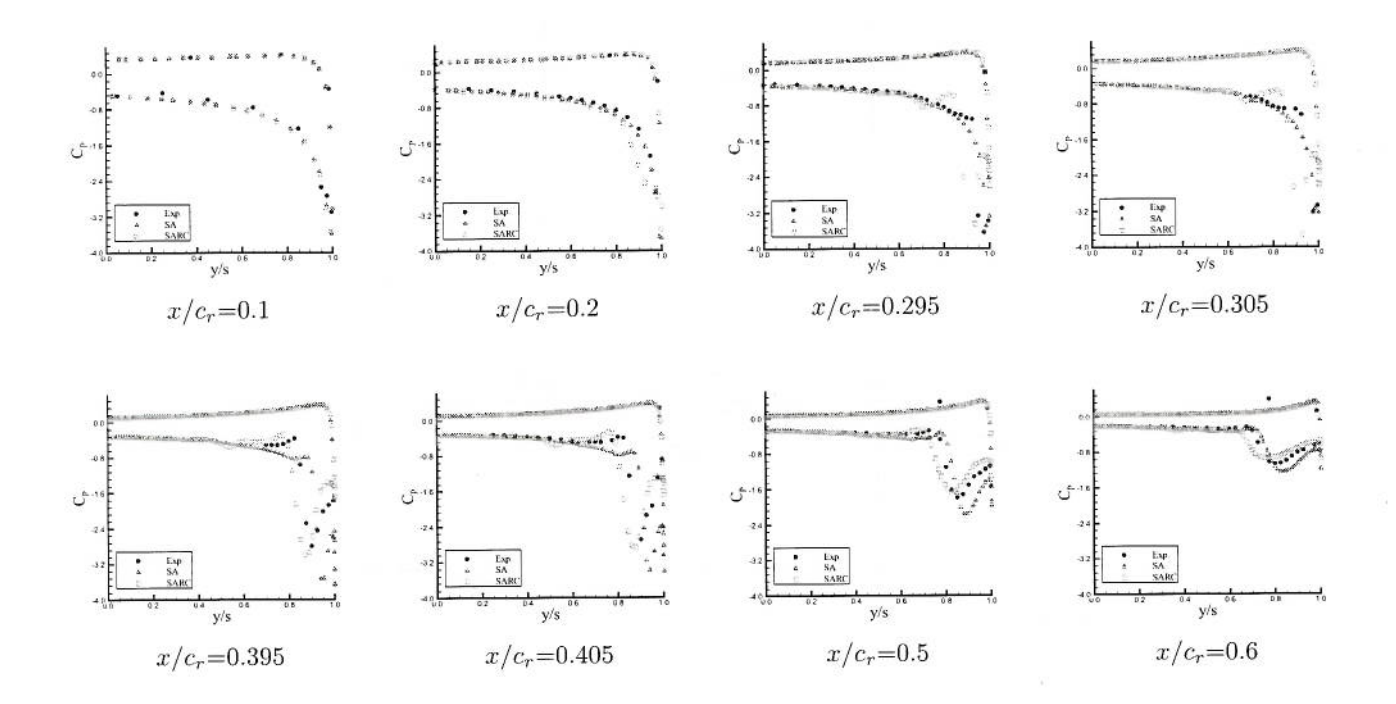


Figure 19. CFD pressure tap data at $\alpha=12^{\circ}$.

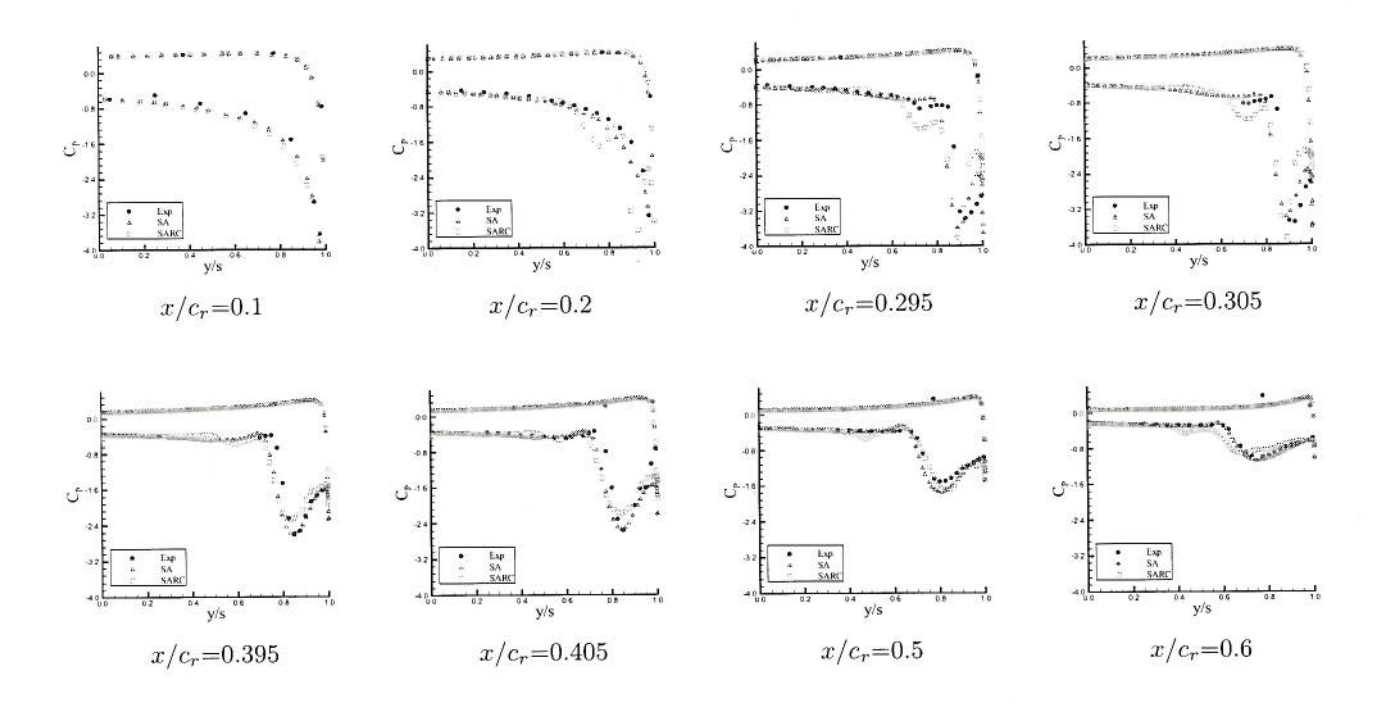


Figure 20. CFD pressure tap data at $\alpha=14^{\circ}$.

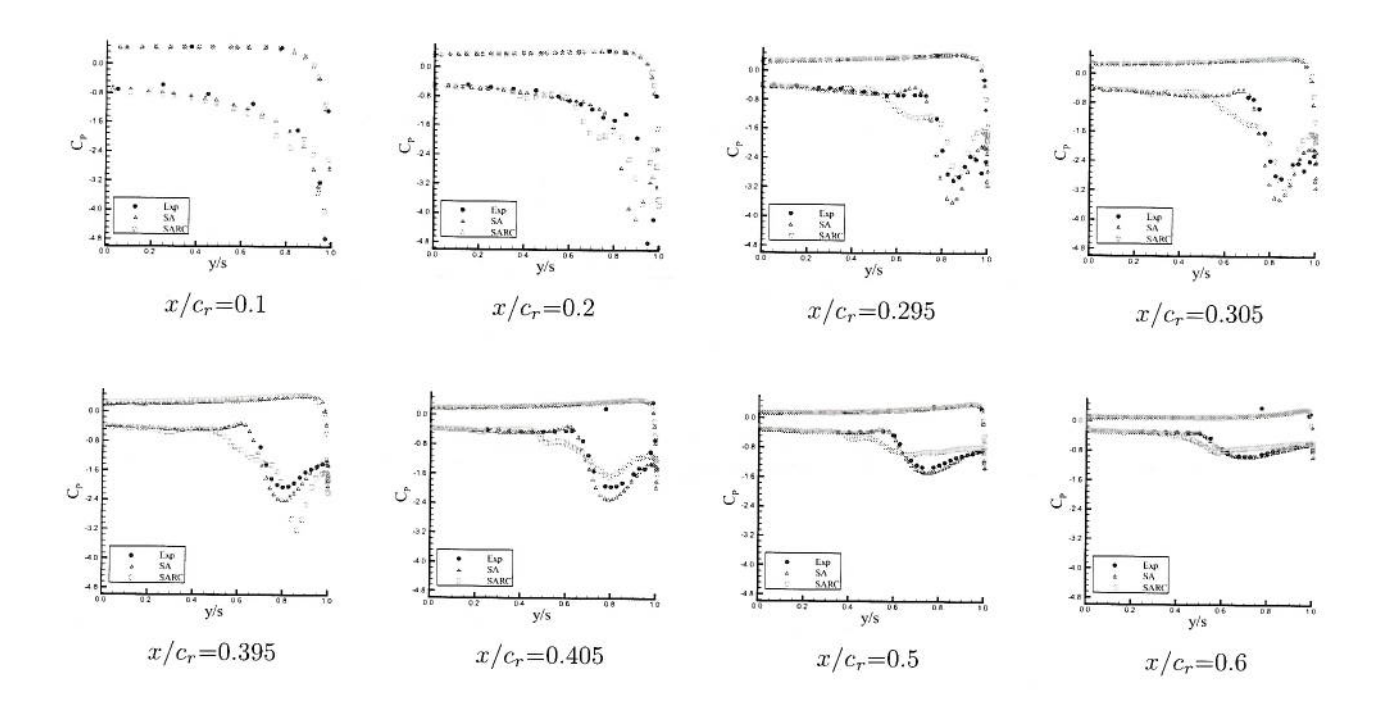


Figure 21. CFD pressure tap data at $\alpha=16^{\circ}.$

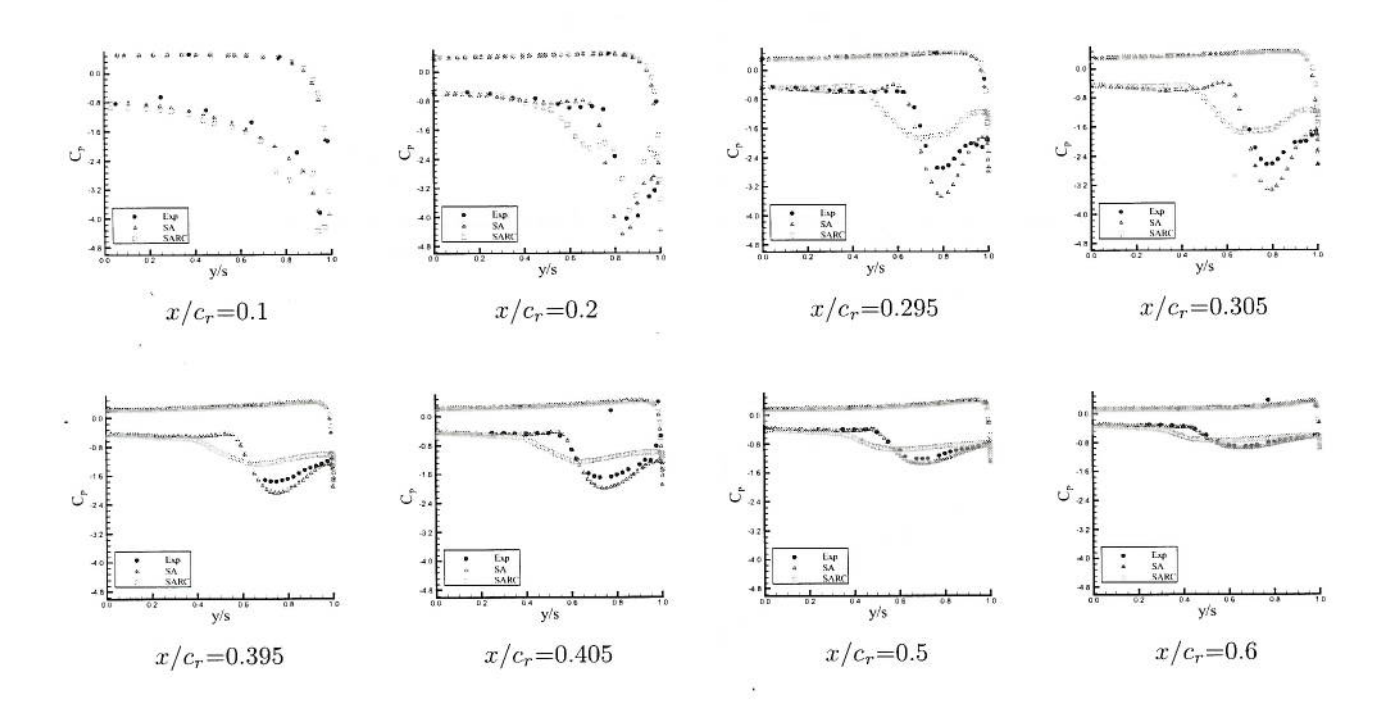


Figure 22. CFD pressure tap data at $\alpha = 18^{\circ}$.

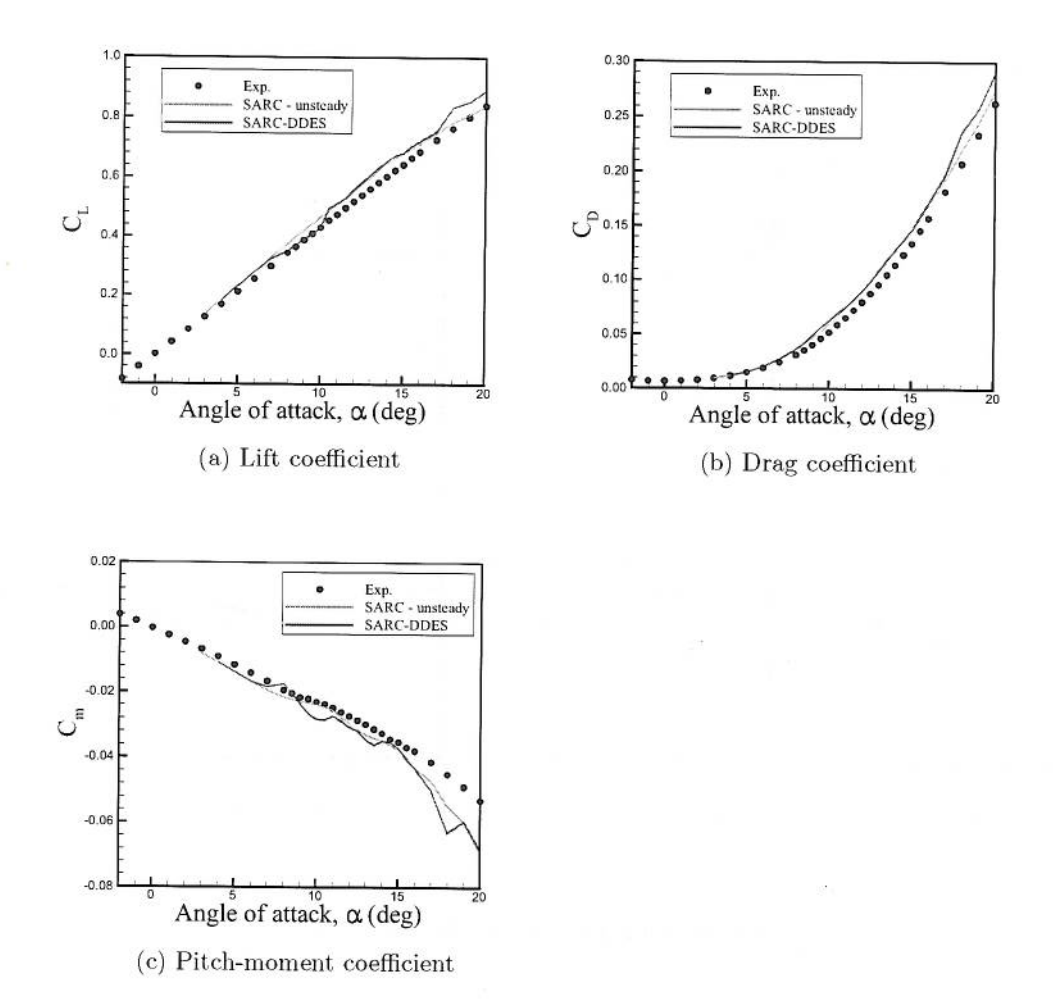


Figure 23. Unsteady simulations using SARC-DDES turbulence model. SARC-DDES cases ran for 12,000 iterations and coefficients were averaged for last 6,000 iterations.